# High Resolution Electronic Spectroscopy of van der Waals Clusters Formed in Superfluid Helium Nanodroplets

Dissertation
zur Erlangung des
Doktorgrades der Naturwissenschaften (Dr. rer. nat.)
der Naturwissenschaftlichen Fakultät IV
-Chemie und Pharmazie-
der Universität Regensburg

vorgelegt von
**Eva-Maria Wirths**
2014

Diese Arbeit wurde angeleitet von: Prof. Dr. A. Slenczka

Promotionsgesuch eingereicht am: 18.12.2014

Prüfungsausschuss: Prof. Dr. N. Korber, Vorsitzender
Prof. Dr. A. Slenczka
Prof. Dr. B. Dick
Prof. Dr. A. Penzkofer

For my Family

&

Benedikt

“Die Endlosigkeit des wissenschaftlichen Ringens sorgt unablässig dafür, daß dem forschenden Menschengeist seine beiden edelsten Antriebe erhalten bleiben und immer wieder von neuem angefacht werden: Die Begeisterung und die Ehrfurcht.”

-Max Planck-

# Table of Contents

# 1 Introduction

Spectroscopy provides an experimental option to investigate matter on the atomic scale. One of the most interesting and challenging domains in this field is the research on clusters, as they fill the gap between well-studied isolated molecules and the bulk phase. Clusters may consist of only a few or up to thousands of atoms and they exhibit a wide variety of properties, which depend to a large extent on the cluster size and structure. One approach to study clusters spectroscopically is the application of doped clusters, i.e. clusters containing a chromophore as a probe molecule. Then the properties of the cluster can be analyzed by regarding the chromophore's spectral signature and its modification under varying cluster formation conditions. Some of the many questions, which are of interest in this research field, are for example: How much insight can be gained about the cluster size and structure by the analysis of the chromophore's spectral signature? Do structural isomers exist for a given cluster stoichiometry and which are the spectroscopic methods that can be applied to distinguish between their different configurations? Are the clusters stable and rigid or rather fluxional? Which factors (temperature, doping conditions, etc.) influence the cluster formation process?

In order to find answers to these questions experiments using superfluid helium droplets as a host system can be applied, since the droplet environment offers many beneficial properties for a systematic research on clusters and their formation process. In spectroscopy helium droplets serve as a cryogenic matrix cooling the embedded species to an equilibrium temperature of 0.37 K within picoseconds, while at the same time ensuring the free rotation and movement of the dopant inside the droplet [TV04]. Thus, cluster formation of individually picked up and cooled particles occurs within the droplet environment. Moreover, it was shown that the doping of helium droplets and therefore also the cluster formation is subject to a statistical process, which helps to distinguish between spectral signals of different cluster stoichiometries [LST95]. The particular properties of helium droplets, which characterize this host system as a gentle matrix well suited for spectroscopic experiments, are reviewed in numerous articles [TV98, CLSS01, SV01, TV04, CDF$^+$06, SL06, ST08]. A general discussion on helium droplets and electronic spectroscopy with helium droplets as a host system can also be found in this thesis in chaps. 2 and 3.

In the present work various aspects of two different cluster systems embedded into superfluid helium droplets are presented. Water clusters with phthalocyanine as a chromophore were chosen as a prototype system for a cluster with a distinct electric dipole moment, so as to enable investigations containing Stark spectroscopy. These investigations were conducted in a continuous droplet beam. The results are discussed in chap. 5, after a presentation of the experimental setup (chap. 4).

The second species considered in this thesis are van der Waals clusters consisting of one anthracene molecule and a differing quantity of argon atoms. This system was selected for investigations, since weakly bound clusters of aromatic molecules with rare gas atoms serve as prototype systems for the spectroscopic research of solvation on a microscopic scale (see e.g. [AEJ82, AEJD83, ASJ84, LJ87, LB90, SBHEJ91, BHEJL92, HLTV98, KTL00, KNT$^+$11, DMK$^+$12a, DMK$^+$12b, DMBS14]). The study on anthracene-argon clusters was conducted in a pulsed droplet beam for varying pick-up conditions. The regarded clusters contain between one and up to ~100 argon atoms. The spectra, which are presented and discussed in chap. 6, are compared with corresponding gas phase measurements in order to gain information on the influence of the helium droplet environment on the cluster formation.

This thesis ends with a conclusion in chap. 7, which sums up the gained results and presents proposals for further research projects.

# 2 Basic Principles of Helium Droplets

This chapter gives an introduction into the properties of bulk helium and helium droplets. The production of droplet beams is discussed for continuous and pulsed helium sources. Moreover, the doping of the droplets with foreign particles, and their coagulation process within the helium environment is presented.

## 2.1 Properties of Helium

The existence of the chemical element helium is known since 1868. It was deduced from the observation of a spectral line at 587.49 nm in the solar spectrum [Jan68]. Due to the manner of discovery the element owes its name to the sun (Greek: helios). It was isolated and studied on earth for the first time in 1895 [Ram95].

From all elements of the periodic table helium is the one with the lowest melting and boiling points. It has two stable isotopes, $^3$He and $^4$He. With a nuclear spin of $I = 0$ $^4$He exhibits a bosonic nature, while $^3$He with a nuclear spin of $I = 1/2$ is a fermion. The physical properties of the isotopes are strongly affected by the difference in the spin statistics. As $^3$He is not relevant for this research project it is not further discussed here. When helium is mentioned in this thesis it generally refers to $^4$He.

Fig. 2.1 shows the phase diagram of $^4$He represented in a double logarithmic plot. It exhibits several abnormalities. For instance, no triple point exists marking the equilibrium between gaseous, liquid and solid phase. For pressures below about 25 bar the transition into the solid phase is missing completely. The fact that helium at standard conditions

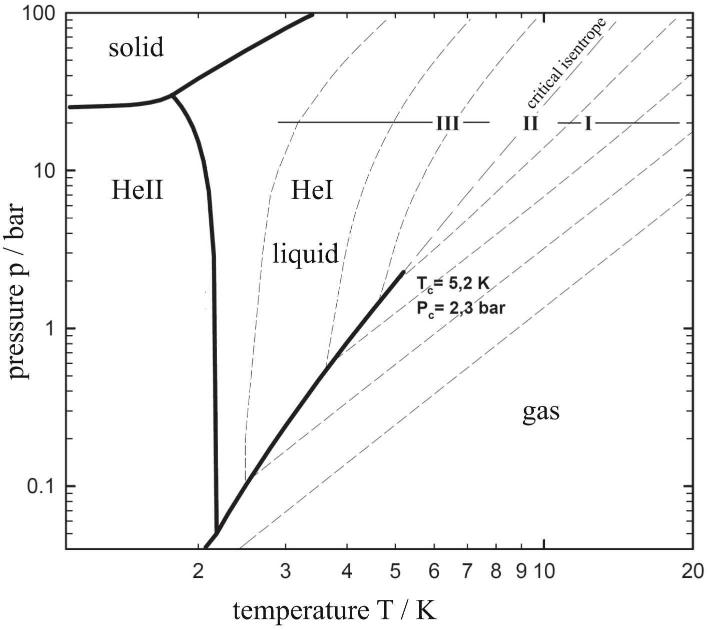

**Fig. 2.1:** Phase diagram of $^4$He (from [BKN$^+$90]). The solid lines are phase boundaries, the dashed lines represent isentropes for different expansion conditions. T$_c$ and p$_c$ are the temperature and pressure at the critical point, respectively.

remains liquid even down to absolute zero is due to the zero-point energy being close to the dissociation energy, which results in an increased delocalization of the wavefunction [TV04]. In addition to the transitions between gaseous, liquid and solid phase there is a further phase transformation between HeI and HeII. By cooling helium gas at a pressure of 1 bar the HeI phase is reached at 4.21 K and the HeII phase at 2.17 K. The temperature below which HeI transitions into HeII is called the $\lambda$-point. The transition from HeI to HeII is recognized by a significant change in the physical properties, observed for the first time in 1938 [Kap38]. To characterize this transition Tisza introduced the two-fluid model for liquid helium [Tis47]. It states that helium below the $\lambda$-point exists as a mixture with two components, a normal fluid and a superfluid fraction. The ratio of the superfluid part increases with further reduction of the temperature. Below 1 K the normal fluid phase is not existent any more and the entire liquid is superfluid. Superfluidity manifests in a very high thermal conductivity and a vanishing viscosity. The consequence is a frictionless motion of foreign substances through the superfluid helium as long as a critical velocity is not exceeded. This threshold is called Landau velocity and takes the value of about 58 m/s for bulk HeII at saturated vapor pressure [Lan41].

Helium is transparent for electromagnetic radiation from the microwave to the vacuum ultraviolet range. Furthermore, it has an exceptionally low polarizability of $\alpha = 0.205$ Å$^3$ and thus its interaction with foreign substances is very weak, which means that it is chemically inert [RS85]. Its relative dielectric constant of $\epsilon = 1.055$ for temperatures between 2 K and 4 K is close to the vacuum value of $\epsilon = 1.000$ [LST95]. Its low temperature, chemical inertness and the other characteristics described above make superfluid helium an ideal host system for spectroscopic research.

## 2.2 Droplet Formation and Properties

Although superfluid helium was expected to be a suitable cryogenic host system for spectroscopy this field of research could not profit from the advantages of HeII in the bulk phase. This is due to the fact that it is basically impossible to solve foreign substances in bulk HeII, since the embedded particles coagulate with each other and condense at the container wall. This problem becomes irrelevant, however, when using droplets of HeII levitating freely in a vacuum apparatus. These helium droplets are composed of thousands up to several millions of helium atoms depending on the expansion conditions.

The first experiment on molecular spectroscopy with helium droplets was reported in 1992 for the infra-red spectrum of $SF_6$ [GSS92]. Subsequent measurements on the same system revealed the fully-resolved rotational lines of the P, Q and R branches [HMTV95]. From the intensity profile of the rotational fine structure a droplet temperature of $0.37 \pm 0.05$ K was determined, which was in good agreement with earlier theoretical predictions. Later measurements on the IR-spectrum of OCS [GHH$^+$00] and numerous other molecules could confirm this value [CLSS01]. Assuming similar transition temperatures for bulk helium and droplets (cf. fig. 2.1) as well as an inner pressure of the droplets far below 25 bar this temperature implies the superfluid state of helium droplets [LST95, TV04]. Further evidence for their superfluidity is given by the free rotation of molecules inside the droplet environment. The fully resolved rotational lines in the reported IR-spectra are therefore seen as a microscopic indication for HeII

[HMTV95, GTV98]. Thus, helium droplets serve as an ideal microscopic research system for superfluidity in addition to their application as a cryogenic host system for embedded species. Moreover, chemical and photochemical reactions can be studied in the gentle ultra-cold droplet environment [TV04, ST08].

Helium droplets are generated by adiabatic expansion of helium into a vacuum chamber. The size and velocity of the superfluid droplets depends on the nozzle characteristics and on the expansion conditions. Typical are nozzle temperatures between 7 K and 30 K and high stagnation pressures between 10 bar and 100 bar. According to the applied droplet source a continuous or pulsed droplet beam is formed.

A continuous-flow nozzle with a small diameter of 5 $\mu$m or 10 $\mu$m is used for the generation of a directed continuous droplet beam. The droplets originate either from free jet expansion of helium gas condensing into clusters or from the fragmentation or Rayleigh break-up of expanded liquid helium. Their size distribution and scattering cross section were determined by different deflection experiments [JN92, LST93, Knu97, HTD98, KH99, TV04]. The average number of helium atoms per droplet and the corresponding droplet diameter are illustrated in fig. 2.2 as functions of the nozzle temperature [TV04]. The graphs correspond to varying stagnation pressures. The droplet size is calculated assuming a spherical shape, a uniform density and a sharp outer edge for a helium droplet. The droplet radius is then given by $R_0 = 2.22 \cdot N^{1/3}$ Å with $N$ being the number of helium atoms, which the droplet contains [BS90]. These assumptions follow the liquid-drop model and are quite reasonable for helium nanodroplets. In the droplet center the particle density almost equates the value for bulk liquid helium of $\rho_{bulk} = 0.0218$ Å$^{-3}$, while at the droplet surface region the density decreases to 10 % of this value [HTD98]. The plots in fig. 2.2 show that for a constant stagnation pressure the droplet size grows with decreasing nozzle temperature. The smallest droplets are produced by condensation of helium gas, the largest ones by Rayleigh break-up of a liquid jet of helium. The different expansion processes are represented by isentropic curves in the phase diagram. They are plotted as dashed lines in fig. 2.1 and can be divided into three groups, the subcritical (I), the critical (II) and the supercritical (III) isentropes, whose evolution is determined by the initial stagnation conditions.

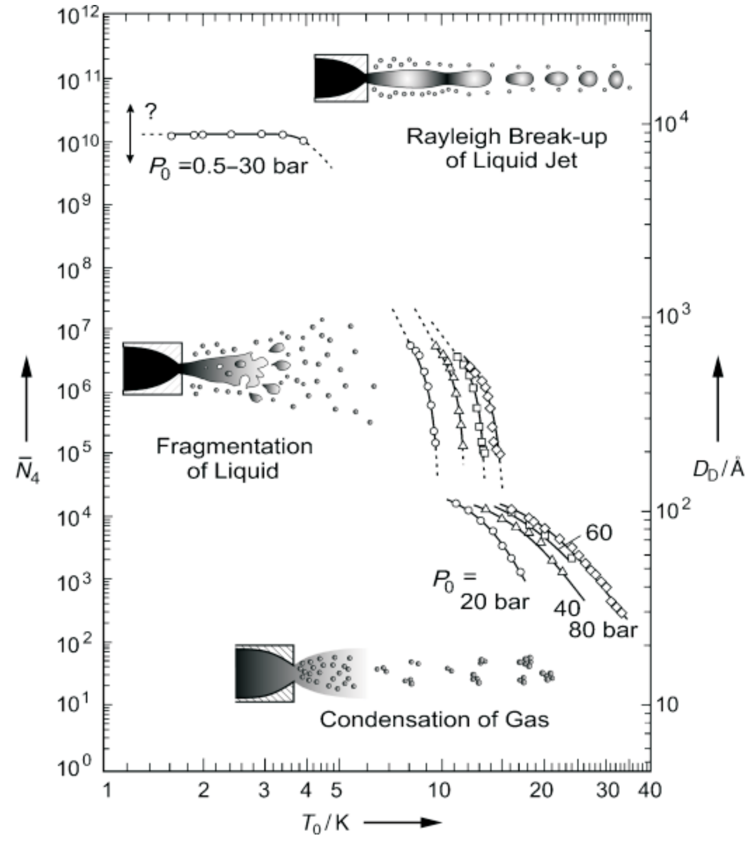

**Fig. 2.2:** Graphic representation of the helium droplets' diameter $D_D$ and the number of helium atoms per droplet $\bar{N}_4$ for the three modes of continuous jet expansion. The graphs correspond to different stagnation pressures $p_0$ and they are plotted against the nozzle temperature $T_0$. (from [TV04])

In the case of subcritical expansion the gas-liquid phase boundary is approached from the gas side. The expanding helium is cooled adiabatically leading to its condensation into droplets. When the collision rate in the expanding gas abates further downstream the condensation process expires. The droplets commence cooling by evaporation of helium atoms. The binding energy for bulk helium of 5 $\mathrm{cm}^{-1}$ ($\equiv$ 7.2 K) per atom on average is also assumed for helium droplets [ST87, TV04]. The evaporation rate decreases exponentially with time, starting with ca. $10^{10}$ $\mathrm{Ks}^{-1}$ and finishing with a droplet temperature of about 0.4 K for times larger than $10^{-4}$ s, which is in good agreement with the experimental equilibrium value [Ste85, HMTV95, HTK97]. The very high initial cooling rate makes the helium droplets a nearly perfect thermostat, as it prevents the increase of the droplet temperature [TV04].

In a droplet beam generated via subcritical expansion the droplets contain between $10^2$ and $10^4$ helium atoms. The droplet size distribution can be simulated by a log-normal distribution via fit of the parameters $\mu$ and $\sigma$ [LST93, TV98].

$$f(N) = \frac{1}{N\sigma\sqrt{2\pi}} e^{\frac{-(lnN-\mu)^2}{2\sigma^2}} \tag{2.1}$$

Thus the mean number of helium atoms per droplet $\bar{N}$ is given by

$$\bar{N} = e^{\mu + \frac{\sigma^2}{2}} \tag{2.2}$$

with a standard deviation of

$$s_{\bar{N}} = \bar{N}\sqrt{e^{\sigma^2} - 1}. \tag{2.3}$$

The droplet's velocity ranges from 200 m/s to 400 m/s. They show a high speed ratio of about $100 \lesssim v/\Delta v \lesssim 300$ [BKN$^+$90].

With supercritical expansion droplets are formed from liquid helium fragmenting into clusters. After the break-up of the liquid the droplets also cool down to the equilibrium temperature of 0.37 K by evaporation of helium atoms, as in the subcritical case. The droplets formed thus exhibit a bimodal size distribution. The large droplets consist of more than $10^6$ helium atoms with an exponentially decreasing size distribution. The small droplets contain about $10^4$-$10^5$ atoms [BKN$^+$90]. The droplet velocity lies in between 50 m/s and 100 m/s. The transitional area between the subcritical and the supercritical expansion is characterized by a droplet formation corresponding to isentropes passing the phase boundary near the critical point ($T_c = 5.2$ K, $p_c = 2.3$ bar).

In addition, a continuous droplet beam can be generated via Rayleigh break-up of a liquid jet of helium. These droplets are much larger than the ones discussed above. They contain between $10^{10}$ and $10^{12}$ helium atoms. The beam velocity is low, clearly below the Landau velocity of 58 m/s, and satisfies the Bernoulli equation $v = c\sqrt{2P_0/\rho_0}$. The pressure $P_0$ and the density $\rho_0$ correspond to the expansion conditions, while $c$ is a constant. The speed ratio is high, approaching values of $v/\Delta v \gtrsim 100$ for decreasing source temperature and increasing stagnation pressure [GT03].

Alternatively a directed beam of helium droplets can be produced with a pulsed droplet source. The pulsed setups reported in the literature are equipped with a General Valve [GEA02, SKMV02, YBE05, YBWE06, YBN+07, YE08] or an Even Lavie Valve, modified for cryogenic application [PRD+09, FAMvH12]. The droplet density in pulsed helium droplet beams is increased by more than an order of magnitude compared with continuous beams. Another fundamental difference is the time dependence of the helium pressure at the nozzle outlet during pulse generation. Hence, the size distribution and velocity of the droplets varies within one pulse, determining its time profile. To characterize the droplet pulses undoped droplets were investigated by Rayleigh scattering of UV radiation [GEA02, PRD+09]. In addition, doped droplets were analyzed by mass spectrometric measurements [YBE05, YE08, FAMvH12] and by recording the laser-induced fluorescence of chromophore molecules embedded inside the helium droplets [GEA02, SKMV02, PRD+09].

With a General Valve 30 - 100 $\mu$s droplet pulses are produced by the movement of a poppet beating against a stainless steel front plate. The shape of the nozzle throat is essential for the expansion characteristics. Depending on the nozzle shape and expansion conditions droplets containing $10^3$ up to $10^5$ helium atoms can be produced [SKMV02, YBE05]. For nozzle temperatures between 9 K and 14 K at a stagnation pressure of 20 bar the droplets exhibit velocities between 330 m/s and 400 m/s [SKMV02].

Instead of a poppet the Even Lavie Valve possesses a plunger pressed against a front gasket with an orifice of 60 $\mu$m in diameter. A helium pulse is produced by sending a short high-current pulse (12 - 25 A) to a low inductance coil inside the valve so as to pull back the plunger by magnetic field force. The opening duration is only about 20 $\mu$s before the plunger is pushed back into its sealing position by a return spring and the gas pressure [noz]. The helium droplet beam produced thus exhibits a bimodal size distribution. The leading fraction consists of droplets with an average size between $10^4$ and $10^6$ helium atoms per droplet depending on the expansion conditions [PRD+09, FAMvH12]. The rear part of the pulse holds large droplets consisting of $> 10^6$ helium atoms. In contrast to the former ones these large helium droplets are not suitable for doping with foreign particles. By varying the expansion conditions the relative abundance of the two fractions is shifted. With decreasing stagnation pressure and increasing nozzle temperature the leading part of the pulse rises and smaller droplets are produced. The droplet velocity can be varied from 250 m/s up to 410 m/s. Fig. 2.3 shows the beam velocity as a function of the stagnation pressure at different nozzle temperatures and repetition rates. From the graphs it becomes obvious that also the repetition rate influences the helium expansion and droplet formation. However, it has only a thermal effect on the valve and an increased repetition rate can be compensated by lowering the nozzle temperature [PRD$^+$09].

The Even Lavie Valve offers several advantages compared with a General Valve. The gas pulse duration is shorter and a better reliability of the system is ensured as it is independent of the lifetime of a poppet. Moreover, the pulse-to-pulse fluctuation is smaller and the short opening time of the valve minimizes the gas load in the source chamber significantly [Pen10].

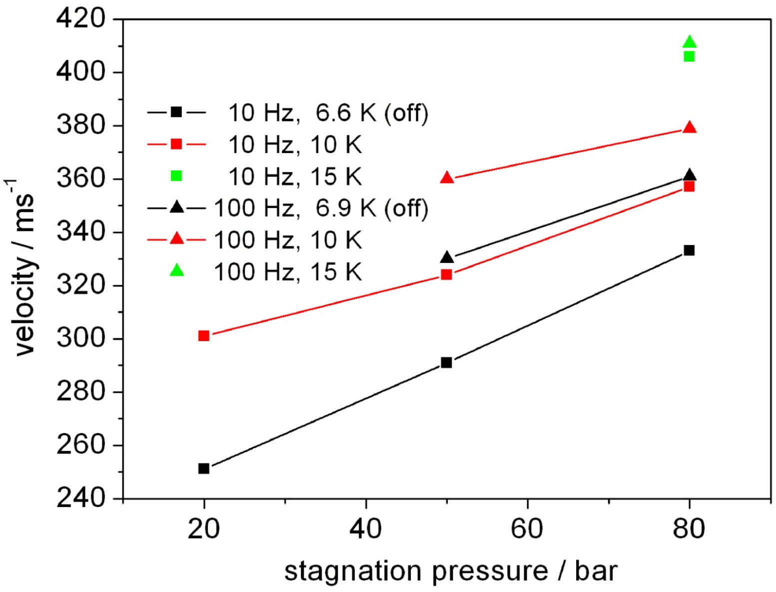

**Fig. 2.3:** Velocities of helium droplets produced at different expansion conditions with an Even Lavie Valve (from [Pen10]).

## 2.3 Doping and Coagulation within the Droplets

The inelastic collision between a superfluid helium droplet and an atom or molecule can result in the embedding of the foreign particle inside the droplet. This is a pick-up procedure, which is used in order to dope the helium droplets with foreign particles. These particles are provided as a gas phase sample in a pick-up unit, which the droplet beam passes on the flight through the vacuum apparatus. The particle density in the pick-up cell is adjusted by tuning to a corresponding vapor pressure. Its adjustment depends on the desired doping, for the pick-up probability is directly influenced by the particle density of the dopant species in the pick-up cell.

The mathematical description, which can be deduced for the probability $P_k$ of doping the droplets on their flight through the pick-up cell with $k$ particles is given by a Poisson distribution [LST95].

$$P_k(n) = \frac{(\sigma n L)^k}{k!} e^{-\sigma n L} \tag{2.4}$$

The length of the droplets' flight path through the pick-up unit is referred to as $L$, while $n$ denotes the particle density of the dopant in the pick-up cell. $\sigma$ is the effective pick-up cross section of the helium droplets, which is proportional to the droplets' geometric cross section. From this it follows that the pick-up probability scales with the size of the droplets $N$ as $N^{2/3}$ for spherical droplets. Hence, equ. 2.4 describes the probability that droplets with an effective pick-up cross section $\sigma$ leave the pick-up cell (length $L$, particle density $n$) with exactly $k$ particles inside.

This model is used for the doping of helium nanodroplets with clusters of a well-defined size distribution. Above all it is applied to experimental data in order to assign spectral features to clusters with a particular stoichiometry. To this purpose the pick-up probability is influenced by varying the dopant's particle density in the pick-up unit. By analyzing the evoked intensity response of the spectra the transitions can be assigned to the clusters under investigation. This is one of the few methods in mass spectrometry, which enables the assignment of cluster stoichiometries without the destruction of the sample.

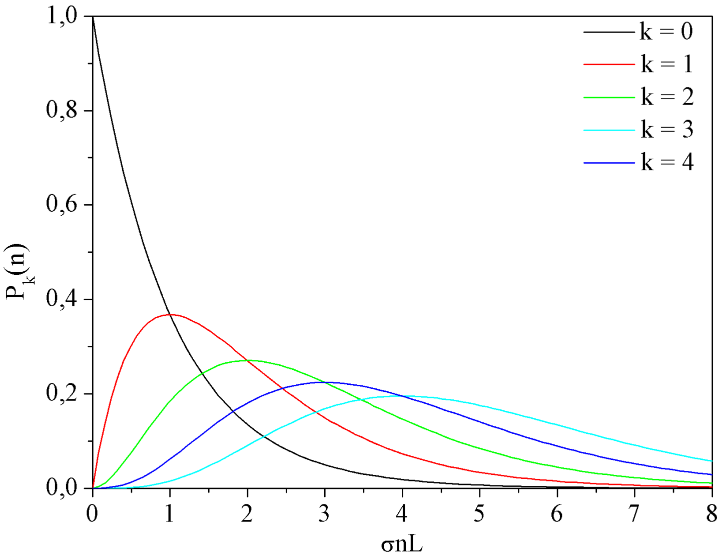

**Fig. 2.4:** Fraction of helium droplets doped with $k$ foreign particles as a function of the particle density $n$ in the pick-up cell. The length of the droplets' flight path through the pick-up cell $L$ and the pick-up cross section of the droplets $\sigma$ are assumed to be constant.

The graphs showing the Poisson distribution according to equ. 2.4 with $k = 0$ up to $k = 4$ are illustrated in fig. 2.4. The argument $\sigma nL$ is the average number of collisions between droplets and particles leading to a capture. In the case of undoped droplets ($k = 0$) equ. 2.4 shows an exponential decay. In the case of doped droplets ($k > 0$) the graphs rise with $n^k$, i.e. a linear increase for $k = 1$, a parabolic increase for $k = 2$, etc. After reaching a maximum the probability $P_k$ decreases exponentially. The positions of the maxima show a linear correlation with $k$ and are characterized by equ. 2.5.

$$n\sigma L = k \tag{2.5}$$

As can be seen in fig. 2.4 the curves for different $k$ overlap and the size distribution of the clusters becomes broader with increasing $\sigma nL$. With increasing $k$ the gradient of $\mathrm{P}_k(\mathrm{n})$ decreases and the difference between graphs of neighboring $k$ numbers becomes less characteristic. Therefore, the easiest case to accomplish and analyze is single particle doping. A loss in size selectivity has to be considered when analyzing multiple particle doping.

The mathematical derivation for the description of the pick-up process is based on several assumptions. One condition for the validity of the Poisson distribution for this procedure is that the doping is a pick-up process of individual particles. In addition, it is assumed that the helium droplets have a uniform size. Furthermore, the cross section of the droplets should not be influenced by the number of picked up particles and therefore be independent of $k$. Another assumption is that the scattering of helium droplets out of the beam can be neglected as well as evaporation effects [LST95]. These conditions are not inevitably fulfilled for a helium droplet beam crossing a pick-up unit.

The assumption that foreign particles are picked up individually by the droplets is quite reasonable. In the pick-up cell the samples investigated in this project are provided at room temperature or higher and their vapor pressure is in the $10^{-4}$ mbar - $10^{-5}$ mbar range. On account of these conditions, i.e. high temperature and low vapor pressure, the formation of clusters in the gas phase can be excluded. The neglect of droplet scattering out of the beam axis and detection volume is also appropriate, as the expansion of the skimmed and aligned droplet beam is small compared to the collection angle of the detector. A monodisperse size distribution and a constant cross section $\sigma$ of the droplets is, however, an approximation, which holds for the case of large droplets and a small number of captured particles. The required droplet size and the allowed number of captured particles for the validity of this approximation depends on the substance under investigation.

Another aspect neglected in this consideration is the fact that stationary conditions, an inherent basic for the mathematical assumptions made above, are not given when using a pulsed helium droplet source. During the passage of one pulse through the pick-up unit a time dependency of the particle density might occur due to the pick-up procedure. However, only a small fraction of the droplet pulse is relevant for the spectroscopic measurements undertaken in this research project as the pulsed helium droplet beam is only used together with pulsed lasers. These have a pulse duration in the nanosecond range (5 ns - 50 ns) and constant pick-up conditions can be assumed for the correspondingly small fraction of the droplet pulse used for spectroscopy. Furthermore, the time profiles are equal for every pulse. Thus, quasi-stationary conditions apply for the doping of a pulsed droplet beam and the pick-up process can be described under the same assumptions as made for the continuous beam [Pen10].

The variation of the droplets' cross section $\sigma$ remains the most serious deviation from the assumptions made above. Therefore it will be considered separately for the substances under investigation in this research work, which are phthalocyanine-water ($\mathrm{Pc(H_2O)}_k$) clusters and anthracene-argon ($\mathrm{An(Ar)}_k$) clusters. The decrease in droplet size and therefore the decrease of the droplets' cross section depends on the energy, which is transferred into the droplets during the doping process. This energy dissipates via evaporative cooling, which is described in chap. 2.2 for the droplet formation. After a collision and capture the momentum and energy of the picked up particle dissipates into the helium environment. In some cases this transfer is not fully completed, but the captured particle leaves the droplet again after passing through it. The probability that a capture is proceeded by the embedding of the particle is characterized by the sticking coefficient $s$, which is $< 1$ for helium droplet doping. Its value depends on the interaction potential between the droplet and the particle as well as on the momentum of energy of the sample [LST95]. In the case of a completed energy transfer the embedded particle reaches the helium droplet equilibrium temperature of 0.37 K within picoseconds.

It is assumed that individually captured and cooled particles undergo coagulation within a droplet due to long-range electrostatic or van der Waals forces between the molecules and atoms. These forces are only marginally shielded by the interspersed helium as the dielectric constant of liquid $^4$He is almost in accordance with the vacuum value [LST95]. By these interactions clusters consisting of $k$ consecutively picked up and cooled particles are formed within the droplets. This coagulation process takes place on a time scale between $10^{-10}$ s and $10^{-8}$ s [LST95] and releases energy into the droplets, which is dissipated again by evaporation of helium atoms from the droplet surface. Due to the superfluidity of the droplets the dopants move and rotate freely according to the interaction with each other. Thus, the formation of unique cluster structures occurs inside helium droplets. This was first observed for cyanoacetylene (HCCCN) forming a long chain cluster only in a helium droplets environment [CDF$^+$06].

Accordingly, the formation of inhomogeneous clusters can be influenced by the order of the pick-up cells, as has been shown frequently [PVH01, LTV06, LSS07, KGMNS$^+$07, KNT$^+$11, DMBS14]. In this work a post pick-up process refers to the embedding of a cromophore into undoped helium droplets and the formation of a van der Waals cluster around it. In the case of a prior pick-up this sequence is changed and the cromophore is the last particle captured by the droplets.

In summary, the total energy released into the helium droplets on pick-up derives from the collision, the internal energy of the foreign particle, the binding energy between dopant and helium and the coagulation process within the droplets. As this energy is dissipated via evaporative cooling a single particle pick-up can lead to the evaporation of between hundreds and thousands of helium atoms from the droplet surface. This size decrease can be estimated for the substances under investigation. The upper boundary of the average internal energy of the gas particles can be estimated calculating with $kT/2$ per degree of freedom. The lower boundary can be estimated assuming an equal distirbution of the vibrational states. Hence the internal energy of phthalocyanine at 600 K is between $15.4 \cdot 10^3$ cm$^{-1}$ and $36.3 \cdot 10^3$ cm$^{-1}$. The internal energy of anthracene at 300 K is between $1.9 \cdot 10^3$ cm$^{-1}$ and $7.1 \cdot 10^3$ cm$^{-1}$. The collision energy is estimated for an average droplet velocity of about 350 m/s from which follows a value of ca. $2.6 \cdot 10^3$ cm$^{-1}$ for phthalocyanine and $0.9 \cdot 10^3$ cm$^{-1}$ for anthracene, respectively. Neglecting the binding energy with helium, which is small in comparison, the the pick-up of one phthalocyanine molecule leads to an evaporation of between 3600 and 7780 helium atoms. The pick-up of one anthracene molecule provokes an evaporation of between 560 and 1600 helium atoms. These numbers are estimated with an evaporation energy of a helium atom of 5 cm$^{-1}$ ($\equiv$ 7.2 K) on average [ST87, TV04]. Argon and water are provided at room temperature and thus the total energies released into the helium environment upon their capture are about $0.5 \cdot 10^3$ cm$^{-1}$ and $1 \cdot 10^3$ cm$^{-1}$, respectively. When multiple pick-up is considered the energy dissipation upon coagulation within the droplet must be taken into account, too. The energies for Ar-Ar and $H_2O$-$H_2O$ binding are about $0.5 \cdot 10^3$ cm$^{-1}$ and $3.4 \cdot 10^3$ cm$^{-1}$, respectively, estimated from the corresponding evaporative energies

[Atk01]. Thus, the number of evaporated helium atoms is about 200 per Ar atom and about 880 per water molecule. This shows that small Pc($H_2O$)$_k$ clusters or even large An(Ar)$_k$ clusters can be embedded into medium-sized or large helium droplets. In the present study of electronic spectroscopy the superfluid droplets can be considered as large, as they consist in all measurements of $> 10^4$ helium atoms, on average.

However, due to the evaporative cooling the cross section $\sigma$ of the helium droplets decreases significantly during the droplet beams flight through the pick-up unit. When multiple particle doping is investigated the distinct change in droplet size influences the analysis of the data. In order to respect this effect mathematically the cluster size within the droplets, which corresponds to the number of picked up particles $k$, is redefined for large pick-up rates [KGMNS+07]. Assuming again that the pickup probability scales with the size of the droplets $N$ as $N^{2/3}$, the corrected average number of picked up particles can be derived from the ratio of the real droplet size $(N_0 - ck)$ to the initial droplet size $N_0$.

$$dk = \frac{(N_0 - ck)^{2/3}}{N_0^{2/3}} \sigma L dn \tag{2.6}$$

The constant $c$ corresponds to the number of helium atoms evaporating upon a single pick-up and $\sigma L$ is defined using equ. 2.4. The integral of equ. 2.6 then yields the average number of captured and embedded particles $k$ corrected for the case of a multiple particle pick-up.

$$k = \frac{N_0}{c} \left[ 1 - \left( 1 - \frac{c\sigma L}{3N_0} n \right)^3 \right] \tag{2.7}$$

Dopant species are divided into two groups, heliophobic and heliophilic ones. Heliophobic substances remain at the droplet surface, while heliophilic ones are located inside the droplets. This depends on the potential between the foreign particle and the helium environment. Organic closed-shell species, rare gas atoms and water molecules show heliophilic behavior while alkaline and alkaline earth metals are generally heliophobic. All substances, which are of relevance in the present work, are heliophilic from which follows their embedding and coagulation inside the helium droplets.

# 3 Spectroscopy on Molecules and Clusters in Helium Droplets

In the following chapter the characteristics of fluorescence excitation spectroscopy, dispersed emission spectroscopy and Stark spectroscopy are discussed for molecules and clusters in helium droplets. These spectroscopic methods are based on recording the fluorescence of the dopant and therefore they can only be applied for species, which exhibit an adequate fluorescence quantum yield. Besides general explanations on the spectroscopic methods the differences between helium droplet spectra and gas phase spectra are considered, since they reflect the interaction between the sample and the helium environment. In this work only organic closed shell molecules and the transitions between their singlet states are regarded.

## 3.1 Fluorescence Excitation Spectroscopy

The principle of laser-induced fluorescence excitation spectroscopy is illustrated in fig. 3.1. It shows the energy level diagram of the ground state $S_0$ and the first electronically excited state $S_1$ of an organic molecule in the gas phase (left) and in a helium droplet environment (right). For each of the electronic states several vibrational modes are shown as well. Ideally, only the lowest vibrational state of $S_0$ is populated and all transitions caused by photon absorption emerge from this state. In order for an absorption to take place the transition has to be allowed and the laser frequency $\nu_L$ has to be on resonance with it. If this is the case, the electronically excited state gets populated and emission with the frequencies $\nu_F$ might occur. The plot of the integrated fluorescence as a function of the excitation frequency yields the laser-induced fluorescence excitation spectrum. The signals in the spectrum provide information on the (ro)vibrational structure of the sample's excited state. The term electronic origin or $0_0^0$ signal refers to the transition from the vibrational ground state of the $S_0$ state into the vibrational ground state of the $S_1$ state. The signal intensities depend on the transition dipole moments, the fluorescence quantum yields of the emissive states and the population in the $S_0$ state. However, for supersonic jet spectroscopy as well as helium droplet spectroscopy the radiative decay upon excitation competes with other non-radiative decay mechanisms such as internal conversion, internal vibrational redistribution and intersystem crossing.

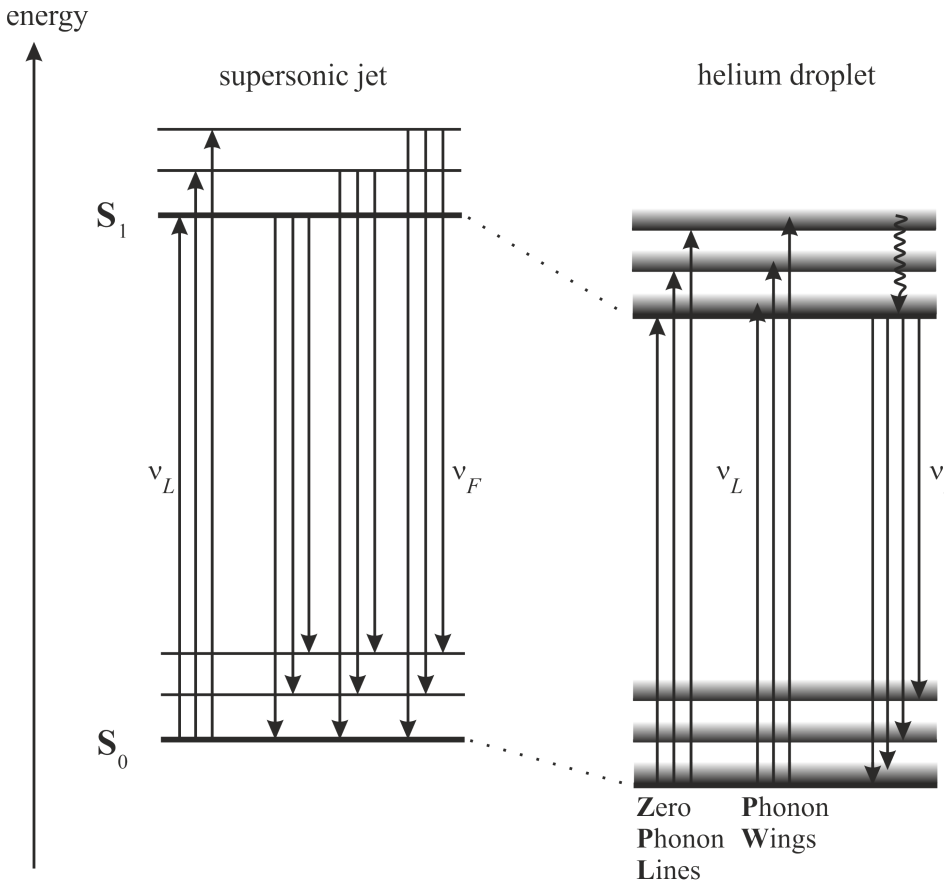

**Fig. 3.1:** Energy level diagram illustrating the principle of fluorescence excitation and dispersed emission spectroscopy. The electronic $S_1 \leftarrow S_0$ transitions of an organic molecule in the gas phase are compared with those in helium droplets. For details see text.

To achieve conditions where only the vibrational ground state of $S_0$ is populated, free molecules or clusters in the gas phase can be prepared by adiabatic expansion in a supersonic jet. However, the cooling is not as efficient as the evaporative cooling observed for helium droplet experiments and thus hot bands are sometimes observed in spectra of jet cooled species. Moreover, the formation process of clusters in supersonic jet measurements can not be described with a well-defined statistic. By contrast, in helium droplets the cluster formation is subject to a statistical process, as explained in detail in chap. 2.3. This helps to assign the excitation signals to clusters with a distinct stoichiometry.

A further difference between gas phase and helium droplet spectra is a frequency shift of the electronic transitions, which is normally in the range of up to ± 100 $cm^{-1}$ [TV04]. It is provoked by the solvation of the molecule in the droplet, which leads to a stabilization of the ground state and the excited state. In the case of helium droplet spectra of phthalocyanine and anthracene, the two substances used as chromophores in this work, the signals appear red-shifted compared to the gas phase spectra [SDHT01, KRH05]. This implies a larger stabilization energy for the excited state than for the ground state. Such a case is depicted in fig. 3.1 on the right side. The vibrational frequencies are affected much less by the droplet environment. Typically, they are only shifted by ± 5 - 10 $cm^{-1}$ [CLSS01, TV04].

Moreover, the intensity pattern of the signals in supersonic jet spectra may differ from the one observed in helium droplet spectra. The reason for this is the state specificity of the radiative and non-radiative decay mechanisms [AHJ88, KM95]. As shown in fig. 3.1, in the case of isolated molecules in the gas phase emission originates only from states, which are isoenergetic to the state populated by the excitation process. In helium droplets, however, emission stems only from the vibrational ground state of the $S_1$. Vibrational energy and other excess energy upon excitation of the dopant dissipates into the helium environment prior to radiative decay [Leh04, ST08]. This relaxation competes with the relaxation into other non-emissive states. Thus, the relaxation mechanism and the fluorescence quantum yield of the vibrational ground state of the dopant's $S_1$ are decisive for the signal intensities in the excitation spectra in helium droplets.

The most noticeable difference to gas phase spectra is, however, the appearance of phonon wings (PWs) in helium droplet spectra. They accompany the pure molecular transitions called zero phonon lines (ZPLs) and are a result of the coupling of the dopant's transitions with the droplet environment. The PWs are assigned to transitions from the electronic ground state of the dopant to collective excitation states of the superfluid helium matrix [TV04]. Therefore, they always appear on the blue side of the ZPLs in the excitation spectra. This is illustrated in fig. 3.1 on the right side, where the phonons of the helium environment are depicted as quasi continuous levels accompanying each molecular state. In the case of glyoxal the PW observed in the excitation spectrum is seen as evidence of the superfluidity of helium droplets, since its structure could be reproduced using the density of states spectrum of bulk HeII [HMTV96]. In fig. 3.2 the high resolution excitation spectrum of glyoxal in helium droplets (a) is compared to the computer simulations of the PW (b). The gap of 5.6 cm$^{-1}$ between the ZPL and the PW as well as the spectral structure of the PW can be explained this way. In the context of helium droplet spectroscopy the term PW generally includes all elementary excitations of the helium environment coupled to the molecular transitions. This can also be seen in fig. 3.2.

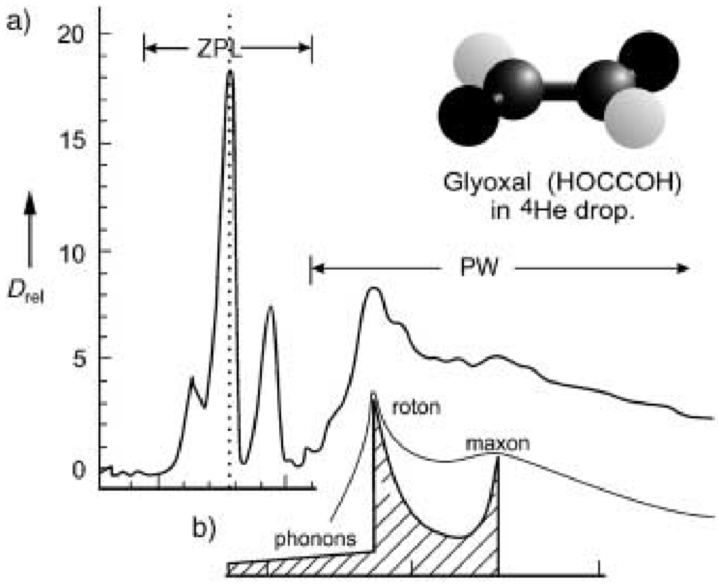

**Fig. 3.2:** Comparison of the excitation spectrum of glyoxal in helium droplets (a) with simulations of the PW using the density of states of elementary excitations in bulk HeII (b) (from [TV04]).

Yet, the phonon gap and the structure of the PW vary with the dopant under investigation. Often sharp lines are observed in the PW fine structure, e.g. for tetracene, pentacene, porphin and phthalocyanine [HLTV02]. These deviations from the spectral structure of elementary excitations of superfluid helium are seen as an indication for a non-superfluid layer of helium atoms localized on the surface of the dopant species [HLTV02, TV04]. Hence, the structure of a PW is determined by excitations of this helium solvation layer in addition to excitations of the superfluid droplet. This explains why the spectral shape of PWs is quite distinct for different dopant species and their excitation signals, ranging from broad features to sharp peaks. Therefore, ZPLs and PWs can not necessarily be distinguished by the shape of the signal [PWP$^+$14].

As ZPLs and their accompanying PWs belong to different transitions they normally exhibit different transition moments. As a consequence, they differ in their saturation behavior in the excitation spectrum. In most cases including phthalocyanine [HLTV02] and anthracene [PS12], the pure molecular transitions have the larger transition probabilities and thus the ZPLs are dominating the spectrum for measurements with moderate laser intensities. With an increasing photon flux, however, these transitions become more easily saturated than the corresponding PWs.

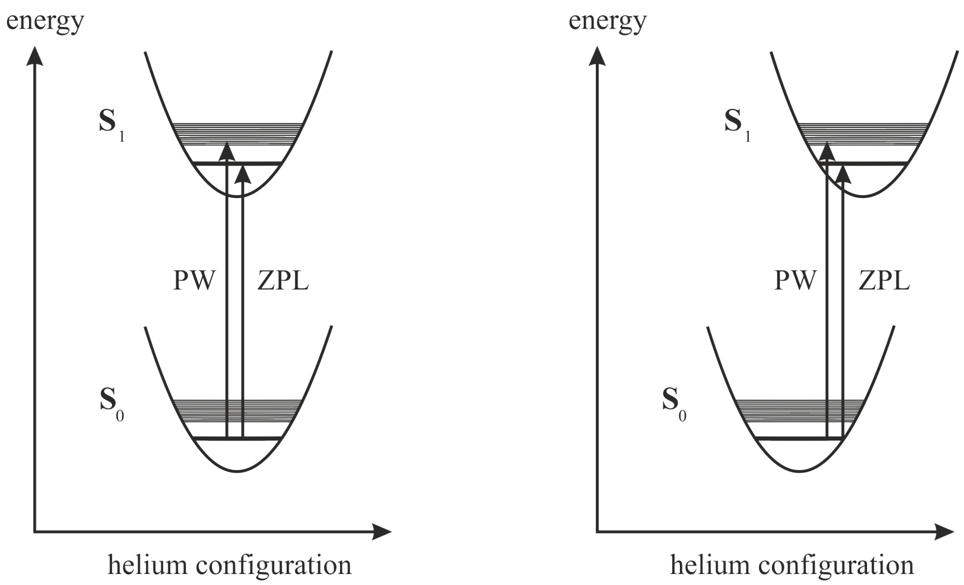

**Fig. 3.3:** Configuration coordinate model showing the displacement of potential energy curves, which corresponds to a weak (left) and strong (right) electron phonon coupling.

However, for some dopant species the PWs are the dominating signals in the excitation spectrum even for measurements with low laser intensities, i.e. even without a saturation of the ZPLs. This was reported e.g. for aniline [LRD05], phenol [Log08], fluorazen [Pen10] and 4-aminophthalimid [Wir10]. The phenomenon is explained with the interaction of the dopant and the non-superfluid helium solvation layer around it. If the configuration of this layer of localized helium atoms differs for $S_0$ and the $S_1$ a change in the ratio of the transition probabilities of ZPL to PW is caused. This is illustrated in the configuration coordinate model of fig. 3.3 showing the dependence of the dopant's potential energy curves on the configuration of the helium solvation layer for a one-minimum potential. The so-called electron phonon coupling responsible for the dominance of the PWs becomes stronger with a growing displacement of the potential energy curves, i.e. with an increasing difference between the configurations of the helium solvation layer in $S_0$ and $S_1$ [Log08, Pen10]. In addition, it has to be assumed that the potential energy surfaces in $S_0$ and $S_1$ may exhibit more than one stable minimum and have a more complex structure than depicted in fig. 3.3. Transitions of metastable configurational variants of the dopant-helium solvation complex might occur, which do not inevitably exhibit stronger oscillator strengths than the PWs. For these reasons a definite assignment of excitation signals to ZPLs or PWs is impossible on the basis of their saturation behavior [PWP+14].

As indicated in the preceding paragraph and fig. 3.3, the helium droplet environment also influences the line width and fine structure of the ZPLs. Ideally, the line width in excitation spectra is homogeneous and only determined by the life time of the excited state, which leads to Lorentzian shaped lines. Often, however, the line width of the excitation laser is the limiting factor. Also Doppler broadening or power broadening can influence the signals line width. In helium droplet spectra sharp signals with Lorenzian line shapes are observed for many organic molecules, e.g. in the case of phthalocyanine [PRV+11] and porphine [Rie11]. However, the droplet size distribution affects the line shape as it leads to a small inhomogeneous broadening [DS01, SDHT01]. In addition, for some molecules in helium droplets, e.g. pentacene [HLTV01] and 9,10-dichloroanthracene [PS13], single vibronic transitions in the excitation spectrum appear broadened. In the case of substituted pyrromethene dyes in helium droplets only the electronic origin remains sharp [PRV+11]. For other molecules, as e.g. 3-hydroxyflavone [LPV+09], 9-phenylanthracene [PGDS10] and 2-methylanthracene [PGDS10], the broadening is even observed for the $0_0^0$ transition and no sharp signals remain in the excitation spectrum. The broadening is explained as a result of a drastic change in the electron density distribution of the dopant upon electronic excitation, which induces an enhanced coupling of the helium environment to the dopant [PRV+11].

Another influence of the solvation of a molecule in helium droplets is a splitting of the ZPLs in the excitation spectrum, which has been reported, among others, for tetracene, anthracene, some metal-phthalocyanines and idole species [HLTV98, LLTV01, LSK+04, KRH05, BMLS07, PS12]. This phenomenon was investigated most thoroughly for tetracene showing a 1.1 $\mathrm{cm}^{-1}$ splitting into an $\alpha$ and $\beta$ line for all ZPLs in the excitation spectrum in helium droplets [HLTV98, HLTV01, PVH01, LTV04, LTV06]. It could be explained by different structures of the helium solvation layer around the dopant analogously to different sites appearing in solid matrices [HLTV01, LS05]. These observations confirm the possibility of several minima in the potential energy surfaces of dopant-helium solvation complexes in $\mathrm{S}_0$ and $S_1$, which was discussed in the preceding paragraphs.

Many of the described phenomena regarding the fine structure of ZPLs and PWs reveal the strong influence of a non-superfluid solvation layer around the chromophore on fluorescence excitation spectra measured in helium droplets. Apart from these observations also rotational spectra indicated the existence of a shell of localized helium atoms around the sample species. It was deduced from the observation that the effective moment of inertia of the solvated molecule was significantly larger than the one of the isolated system [HMTV95, CLSS01, TV04, CDF+06]. Moreover, theoretical studies confirmed the assumption of a coexistence of a superfluid phase and a normal-fluid solvation layer for doped helium droplets, too [WHKW05, WDW09].

## 3.2 Dispersed Emission Spectroscopy

To understand the principle of dispersed emission spectroscopy fig. 3.1 can be regarded again. The basis of the technique is to keep the frequency of the excitation laser $\nu_L$ fixed on resonance with one of the transitions. Thus, the excited state gets populated and emission with the frequencies $\nu_F$ can be recorded in the case of an adequate fluorescence quantum yield. To record a spectrum the emission is dispersed and the fluorescence intensity is plotted according to its frequency. The signals in the spectrum provide information on the (ro)vibrational structure of the sample's ground state. Their intensity pattern is determined by the transition moments, which are given by Franck-Condon-factors depending on the geometry of the dopant species in the ground state and in the excited state [Fra26, Con26].

In the case of isolated molecules in the gas phase emission is only observed from states, which are isoenergetic to the state populated by the excitation, as shown on the left side of fig. 3.1. Thus, the vibrational excess energy and therefore the excitation frequency of the laser $\nu_L$ is decisive for the vibrational frequencies and the signal intensities observed in the emission spectrum. However, in helium droplets the main characteristic of dispersed emission spectroscopy is the fact that fluorescence only occurs after any vibrational or other excess energy of the excited dopant has dissipated into the helium environment. This is shown on the right side of fig 3.1. As a consequence emission measured in helium droplet experiments exclusively stems from the vibrational ground state of the dopant's $S_1$. If the origin of the dispersed emission spectrum coincides with the excitation frequency it can definitely be assigned to the $0_0^0$ transition of the dopant system. Thus emission spectroscopy helps to identify the electronic origin of a chromophore in helium droplet spectra and can be used to distinguish between isomeric clusters, as they show differing emission spectra. However, this analysis is limited by the resolution of the spectra, which depends to a large extent on the experimental conditions (cf. chap. 4.2.3.2). In contrast to gas phase spectra the dispersed emission recorded for molecules or clusters in helium droplets is generally independent of the excitation frequency $\nu_L$ and molecules excited into high-energy vibrational states show the same emission frequencies $\nu_F$ as those excited at the electronic origin [LS03, LS04b, LS04a, LS05, PS12, PS13]. Thus, emission spectra in helium droplets are only comparable with gas phase spectra measured for the excitation of the $0_0^0$ transition.

As in the case of fluorescence excitation spectroscopy, however, the droplet environment affects the fine structure of the signals also in dispersed emission spectra. In addition to the usually sharp lines of the molecular transitions, whose line width is normally limited by the experimental conditions, PWs are observed as well. This is depicted in fig. 3.1 on the right side for the PW accompanying the transition from the excited state into the vibrational ground state of $S_0$.

Also the influence of the non-superfluid solvation layer of localized helium atoms on the dopant's surface can be observed in emission spectra recorded in helium droplets. For some molecules and clusters, e.g. Pc, Mg-Pc and Pc(Ar)$_k$ with $k = 1, 2, 3$ [LS03, LS04a, LS04b, LSS07], it provokes a line splitting of the emission signals. As each isomer of the dopant-helium solvation complex exhibits its own emission this phenomenon indicates a relaxation dynamic upon the excitation of a distinct isomer. This theory was confirmed for Pc by path-integral Monte-Carlo calculations, which identified two different configurations of the helium solvation layer around the chromophore [WHKW05]. A more detailed explanation on the spectroscopy of Pc is discussed in chap. 5.1.

## 3.3 Stark Spectroscopy

The basic principle of Stark spectroscopy is to disturb an initially isotropic molecular ensemble by the application of an external electric field. In the gas phase molecules or clusters can rotate freely and thus show isotropy. Free rotation is also ensured in superfluid helium droplets, as was demonstrated in spectroscopic experiments revealing the fully-resolved rotational fine structure of molecules in helium droplets [HMTV95, GTV98]. A homogeneous electric field can be used in order to transform the molecules or clusters under investigation into an anisotropic ensemble. For the interaction with the external field the sample particles are required to possess a permanent dipole moment. Then the potential induced upon the molecular electric dipole $\vec{\mu_p}$ by the external electric field $\vec{E_f}$ can be described according to equ. 3.1. The angle between the electric field and the dipole moment is given by $\vartheta$.

$$E_{pot} = -\vec{\mu_p} \cdot \vec{E_f} = -\mu_p \cdot E_f \cdot cos\vartheta \qquad (3.1)$$

Thus, the isotropy of the molecular ensemble is broken by the application of an external electric field. It hinders the free rotation of the molecules or clusters, which leads to a splitting of initially degenerated rotational states. This phenomenon is known as Stark effect. However, an alignment of the sample particles in the external electric field is only achieved for $E_{rot} << \mu_p \cdot E_f$, i.e. if the energy gained by the orientation of the molecular dipoles in the external field significantly exceeds the rotational energy. This results in an oscillating movement of the dipoles around the direction defined by the electric field and the rotational states of the particles undergo a change into so-called pendular states. Therefore, the spectroscopic technique to investigate this anisotropy is also known as pendular state spectroscopy.

In order to achieve information about the alignment of molecules or clusters under investigation the probe technique has to be sensitive to detect the anisotropic angular distribution generated by the static electric field. The method applied in the present work is based on recording the laser-induced fluorescence of the sample particles. The fluorescence intensity recorded for an adjustment with the laser polarization parallel to the electric field is compared to the fluorescence intensity recorded for a perpendicular adjustment. In the case of an anisotropic ensemble of chromophores these intensities differ depending on the orientation of the transition dipole moment $\vec{\mu_t}$ with respect to the electric dipole moment $\vec{\mu_p}$. Fig. 3.4 illustrates the correlation between the orientation of $\vec{\mu_t}$ and $\vec{\mu_p}$, the laser polarization, the direction of the electric field and the resulting transition intensity. Generally, the best transition probability is observed when the laser polarization matches the direction of the transition dipole moment $\vec{\mu_t}$.

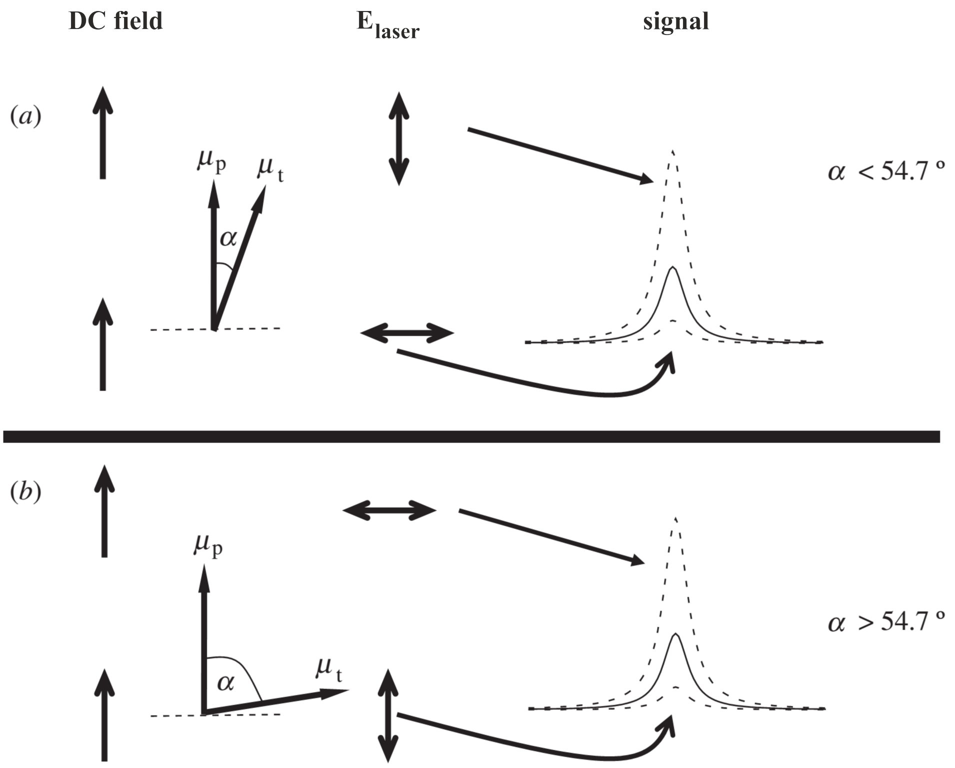

**Fig. 3.4:** Schematic depiction illustrating the effect of a DC electric field on the intensity of a transition signal for different directions of the laser polarization $E_{laser}$, parallel and perpendicular relative to the electric field. Chromophores with a transition dipole moment $\vec{\mu_t}$ rather parallel (a) and rather perpendicular (b) to the electric dipole moment $\vec{\mu_p}$ are distinguished. The solid lines represent the field free experiment. (from [CDM05])

In the upper panel (a) of fig. 3.4 the transition dipole moment of the chromophore is almost parallel to the electric dipole moment. In such a case the signal is most intensive for a parallel adjustment of the laser polarization with respect to the electric field. The signal decreases significantly for a perpendicular adjustment. The reverse is the case for the situation depicted in the lower panel (b) of fig. 3.4, where the transition dipole moment of the chromophore is close to perpendicular to the electric dipole moment. These situations are compared to the field free experiment. The corresponding signal is represented in fig. 3.4 by a solid line. The difference between the absorption of light polarized parallel and perpendicular to an orientation axis is also known as linear dichroism.

# 4 Experimental Setup

This research work was performed with two different experimental setups. One consists of a vacuum apparatus for continuous droplet beams combined with continuous laser systems. Comparable helium droplet machines have been described frequently e.g. in [BKN$^+$90, TV98, TV04]. The second setup combines pulsed laser systems with a vacuum apparatus for pulsed droplet beams equipped with an Even Lavie Valve for cryogenic application. It was first described in [PRD$^+$09, Pen10]. This chapter is devoted to the detailed description of both setups.

## 4.1 Continuous Droplet Beam Experiments

### 4.1.1 Helium Droplet Apparatus

A picture of the vacuum apparatus for continuous droplet beams used for this study can be seen in fig. 4.2. It consists of two differentially pumped vacuum chambers, the source chamber and the detection chamber. The schematic drawing of fig. 4.1 illustrates the essential components for the droplet beam formation, skimming, doping and detection. For the experiments undertaken with this machine conditions near the ultra high vacuum range are indispensable. The typical pressure values are listed in tab. 4.1. In each chamber the vacuum is measured with an Active Inverted Magnetron Gauge / Penning Gauge (Edwards AIMSL-NW25) and the prevacuum with an Active Pirani Gauge (Edwards APG-M-NW16). They are read out with an Active Gauge Controller (Edwards RS232 Option).

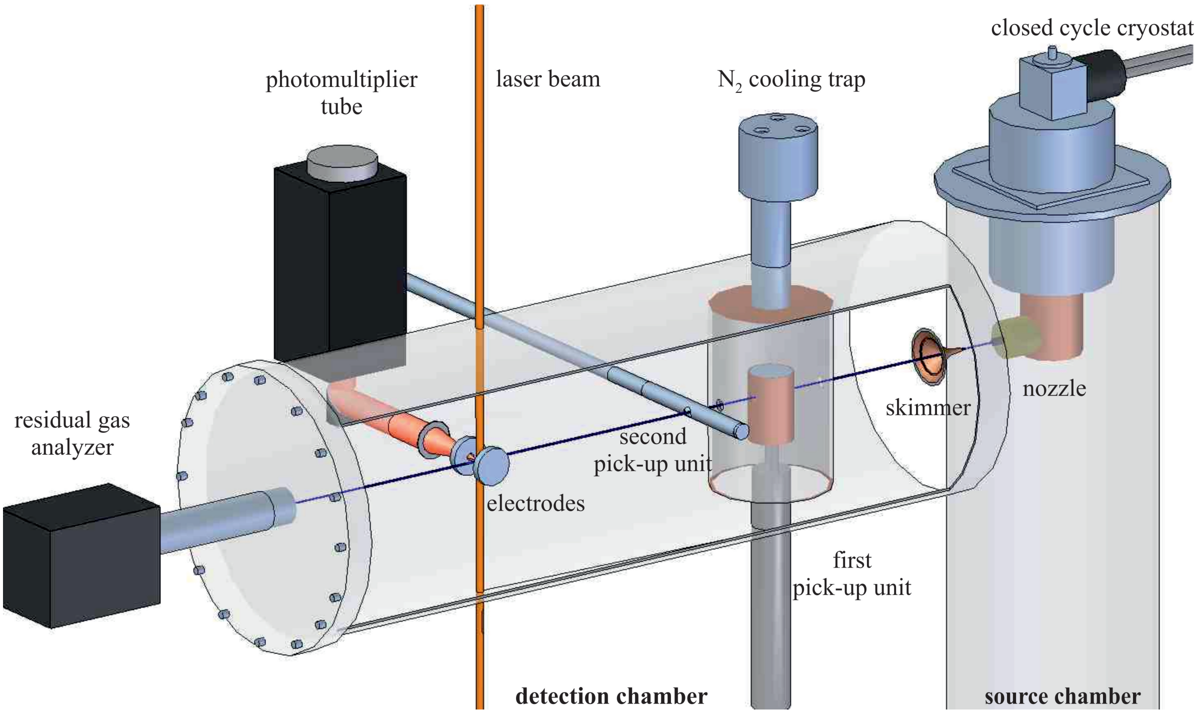

**Fig. 4.1:** Schematic depiction of the helium droplet apparatus.

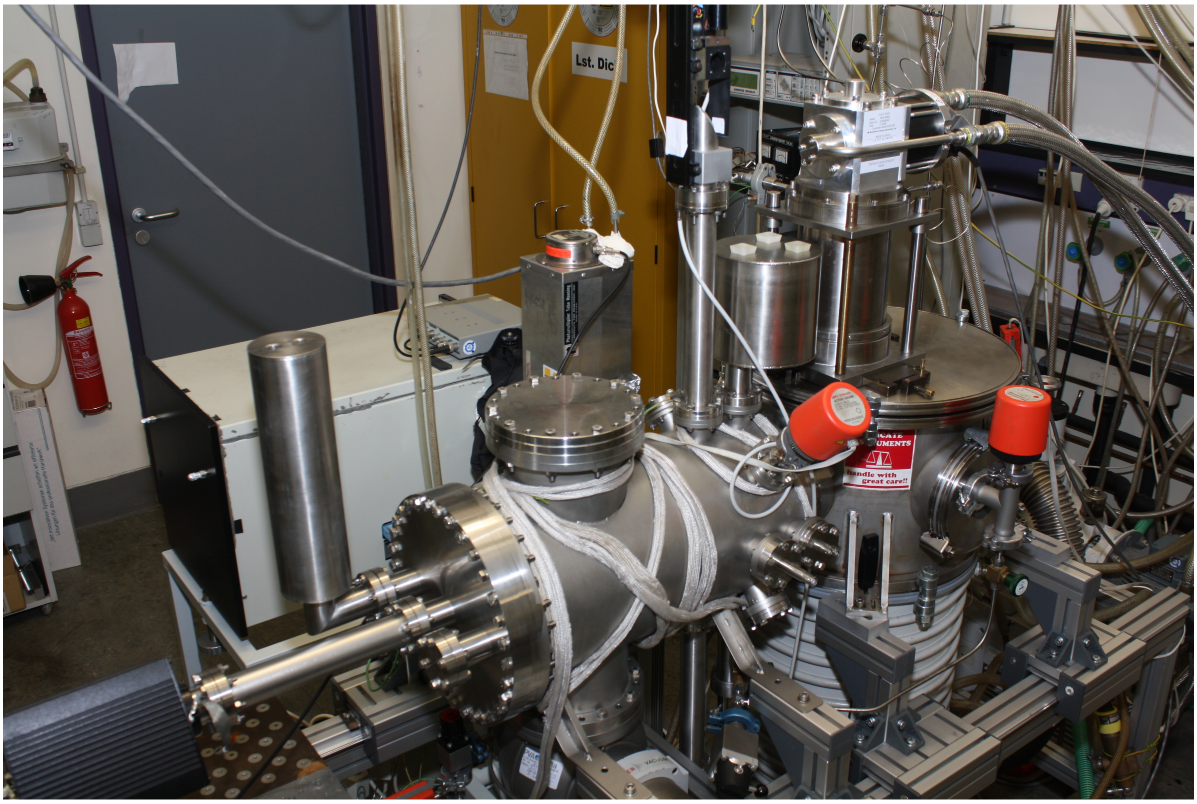

**Fig. 4.2:** Photo of the helium droplet machine for measurements with a continuous droplet beam.

**Tab. 4.1:** Base and operating pressures in mbar. The operating pressure refers to beam generation at 11 K and 20 bar.

| chamber | base pressure | operating pressure |
|---|---|---|
| source chamber | $2 \cdot 10^{-6}$ | $6 \cdot 10^{-5}$ |
| detection chamber | $5 \cdot 10^{-8}$ | $4 \cdot 10^{-7}$ |

The formation of a directed helium droplet beam takes place in the source chamber of the apparatus, which is evacuated by an oil diffusion pump (pumping rate 6000 l/s, Leybold DI 6000 E). A roots pump (Leybold Ruvac WAU 251) and a rotary vane pump (Leybold Trivac D65B) act as booster pumps. The droplet beam is generated by supersonic expansion through a continuous flow nozzle with a diameter of 5 $\mu$m. The nozzle is mounted to the second stage of a closed cycle helium cryostat (Sumitomo cold head RDK-40852 and compressor unit F-50Hw), which suffices to cool down to a nozzle temperature of 7.5 K. Higher temperatures are accomplished with an accuracy of ± 0.2 K by counter heating with a thermal resistor. A silicon diode mounted on the second stage of the cryostat is used as sensor for reading the so-called “nozzle temperatures”. The temperature is stabilized by a remote control system (Neocera LTC-11). Temperatures between 10.3 K and 12 K were used for the experiments undertaken with this apparatus. Through the nozzle pre-cooled $^4$He (purity 99.9999 %, Linde Helium 6.0) at a stagnation pressure of 20 bar is adiabatically expanded into the source chamber. This results in the formation of droplets with an average size in the order of $10^4$ helium atoms per droplet. In order to adjust the droplet beam axis the whole expansion unit can be moved in the three directions in space. At 1.8 mm distance from the nozzle the continuous droplet beam passes a skimmer, which separates the two vacuum chambers. It is mounted to a conically-shaped wall and exhibits an opening diameter of 0.7 mm.

In the detection chamber vacuum is generated by a turbo molecular pump (pumping rate 500 l/s, Pfeiffer TPU 510) and a rotary vane pump (Edwards RV12). The doping of the droplets, the excitation of the sample and the measurements are undertaken in this chamber. For the research of inhomogeneous clusters inside superfluid helium droplets two separate pick-up units are required. About 9 cm within the detection chamber the droplet beam enters the first pick-up cell consisting of a cylindrical oven for solid probe substances. The length $L$ of the pick-up cell is equal to the inner diameter of the cylinder, which is 20 mm. The helium droplets pass the oven via two opposite holes with a diameter of 4 mm each. The sample is provided as a pellet in a holding cap of the oven. For sublimation it can be heated resistively up to 400 °C with a tunable DC-voltage supply (Voltcraft TNG40). The temperature is controlled with a thermocouple (type k, Thermocoax) connected to the oven. To exchange the probe the whole pick-up unit can be removed from the apparatus without breaking the vacuum via an airlock. This pick-up unit was used for doping the helium droplets with Pc. In order to shield the photomultiplier tube from black body radiation the oven is encased in a stainless steel cylinder and the entire pick-up unit is surrounded by a cylindrical copper shield. Both have openings for the droplet beam to pass through, 5 mm and 7 mm, respectively. The copper housing is cooled to 77 K via contact with an external liquid nitrogen reservoir. This ensures a better thermal shielding of the oven and considerably reduces contamination of the detection chamber, for water and other impurities as well as effusing probe molecules from the oven are condensed onto this liquid nitrogen trap.

The second pick-up unit employed to dope the helium droplets with water is located at a distance of about 13 cm from the skimmer and consists of a stainless steel pipe of about 15 cm in length. In order to realize doping a continuous flow of probe molecules is perpendicularly intersected with the droplet beam. The pipe's diameter, which is 6 mm, therefore corresponds to the length $L$ of the pick-up cell. The helium droplet beam passes this pick-up unit via two opposite openings of 4 mm. In order to control the sample flow the pipe is connected to a gate valve and a leak valve. The leak valve (Leybold 283-41-V2) is operated manually and enables a gas flow from $5.0 \cdot 10^{-6}$ mbar l/s up to 1000 mbar l/s. This performance suffices for doping the helium droplets with single molecules, but also enables the building of bigger clusters with up to several hundreds of molecules. Implementing stable pick-up conditions for water doping poses a challenge, because of fluctuations in the gas flow caused by condensation. The distilled water is provided in a small glass container, which is connected to the metering valve via a piping system consisting of stainless steel tubes. This construction is based on the description in [Chr13], but could be considerably improved by shortening the pipeline from 1.5 m down to 15 cm and connecting it directly to the water reservoir. To avoid condensation the stainless steal pipe and the two valves were constantly heated to 35 °C during measurements. A convenient vapor pressure is achieved by cooling the water reservoir with salty ice water, which offers a minimum temperature of -23 °C.

About 17 cm from the skimmer laser excitation and signal detection takes place (cf. chap. 4.1.2). For this purpose the droplet beam is intersected at right angle with a laser beam. The detection of the laser-induced fluorescence is conducted perpendicularly to both beams. Also perpendicular to both beams two capacitor plates are installed to enable the application of a static homogeneous electric field in the detection area. They are mounted at a distance of 1.2 cm and one electrode exhibits a center hole, so as not to block the fluorescence light. The voltages are provided by a commercial high voltage supply regulated via an analogue voltage between 0 V and 10 V so as to be able to change the Stark field continuously. For this research project voltages between 0 V and 20 kV were applied to the electrodes, though voltages up to 25 kV would be possible without emitting of electric sparks. The output voltages are read out and recorded with a data acquisition program on the experiment's PC.

A residual gas analyzer operating on the basis of a quadrupole mass filter (Inficon Transpector H300M) is mounted to the backside of the detection chamber on-axis to the droplet beam. It permits the detection of mass to charge in a range of m/z = 1 - 300 amu and allows to monitor the alignment of the droplet beam during operation. It is used to align the nozzle, to check on the droplet formation and to analyze the doping conditions. To avoid background signal, the analyzer is switched off during measurements.

### 4.1.2 Laser System and Optical Detection

The continuous visible light required for these studies is provided by a tunable continuous wave dye laser (Coherent 899-29 autoscan) pumped by a continuous $Ar^+$-laser

(Coherent Innova Sabre R). The dye laser, which is equipped with a wavemeter, is run in single-mode operation with fully automatic frequency tuning. It offers an accuracy of 0.0017 $cm^{-1}$ and a spectral linewidth $\leq$ 1 MHz. Output powers are typically between 150 mW and 300 mW, but these values are reduced by about 20 % on the way to the excitation region inside the helium droplet apparatus.

An optical fiber is used to guide the beam from the laser to the machine, where it is coupled into the detection chamber from above. To minimize reflections and to avoid interferences the quartz window used for this purpose is mounted at Brewster angle (55,58°). For a good signal to noise ratio (S/N-ratio) in the spectra it is essential to reduce laser stray light as much as possible. Therefore the beam does not directly enter the detection chamber after passing the quartz windows, but is guided through a 20 cm tube with an inner diameter of 4 cm. It is blackened and equipped with baffles in such a way as to minimize stray light of the laser beam entering the vacuum chamber. The beam passes an analogue construction at the exit side. In this study measurements with the laser polarization perpendicular to the Stark field were conducted as well as such with the laser polarization parallel to the electric DC field. Since the transmission of Brewster windows is sensitive to the laser polarization, the entire optical setup had to be turned by 90° when switching between the two arrangements.

Perpendicular to the two intersecting beams the optical detection unit is mounted. A quartz lens collects the fluorescence light at 6 cm from the excitation region. This distance corresponds to the lens' focal length. With a second lens the fluorescence signal is imaged onto the photocathode of a photomultiplier tube (PMT) (Hamamatsu R943-02). To reduce thermal noise the PMT is cooled to -25 °C. Besides, an edge filter can be placed in front of the photocathode to reduce scattered laser light and thus additionally improve the S/N-ratio. The PMT signal is then amplified by a factor of five via a Preamplifier (Stanford Research Systems SR445) before being recorded by a photon counter (Stanford Research Systems SR 400). Finally the data is read out, stored and imaged by a PC, where a LabView program is used for the data acquisition and the graphic display.

### 4.1.3 Measurement Techniques

#### 4.1.3.1 Fluorescence Excitation Spectra

Measuring the laser-induced fluorescence of a molecule or cluster in superfluid helium droplets offers information not only about the probe molecule or its clusters but also about the interaction with the surrounding helium environment, as described in chap 3.1. The basic principle of fluorescence excitation spectroscopy is to record the intensity of the fluorescence light with the PMT, while scanning a certain frequency range with the excitation laser. For this reason the frequency tuning of the laser and the signal acquisition have to be synchronized. At the beginning of a scan the laser is set to a certain wavelength and kept fixed for a previously defined delay time. In this time frame the integrated fluorescence is measured, amplified and finally recorded by the photon counter. Subsequently, the photon counter sends a trigger pulse to the laser and to the data acquisition program. Thereupon the photon counter data are read out by the PC and the laser control tunes the frequency to the next position. After the frequency change is accomplished the laser control triggers the photon counter to initiate the next acquisition cycle. The whole procedure is repeated until reaching the final frequency. Starting and finishing wavelength as well as the increment have to be specified before the initiation of the scan. The stored data on the experiment's PC and the information of the scanned wavelength on the laser's PC are combined after the measurement to form a laser-induced fluorescence excitation spectrum.

#### 4.1.3.2 Stark Spectra

In addition to common fluorescence excitation spectroscopy a static homogeneous electric field can be applied to the excitation region to observe changes in the spectroscopic signals caused by the generated electrical potential. This research offers additional information on the alignment of polar molecules and clusters as described in chap. 3.3. Generally, various techniques of measurement are possible to record the difference in signal intensity for a varying Stark field strength and different adjustments of the laser polarization. In one case a constant high voltage is applied to the capacitor plates while measuring the fluorescence excitation over a certain frequency range. This experiment is repeated with varying voltages. In the present work 0 V, 10 kV and 20 kV were applied. Then the adjustment of the laser polarization with respect to the direction of the electric field is changed before repeating the measurements with the new setup. Comparing the different spectra offers insight on how the Stark field influences the position and line shape of the excitation signals of the chromophore. Another possibility is to keep the laser frequency fixed and to vary the Stark field strength while recording the fluorescence excitation signal. In the present study the high voltage field was slowly increased and decreased on the one hand or quickly switched between 0 V and 20 kV on the other hand. The former procedure offers more information on the signal's response to the Stark field strength, while the latter is faster and suffices for a comparison of data with and without Stark field. Both methods were applied for a parallel as well as a perpendicular adjustment of the laser polarization with respect to the direction of the Stark field.

## 4.2 Pulsed Droplet Beam Experiments

### 4.2.1 Helium Droplet Apparatus

The vacuum apparatus used for pulsed helium beam experiments is comparable to the one for continuous droplet beams characterized above (cf. chap. 4.1). It is shown in the picture of fig. 4.4 and the main parts are depicted in the schematic drawing of fig. 4.3. The two chambers, the source chamber and the detection chamber, are pumped separately reaching conditions near the ultra high vacuum range. As the droplet beam generated in this apparatus is pulsed, a lesser amount of helium is expanded into the two chambers compared to the continuous droplet beam experiments. This accounts for a better vacuum in both chambers. Typical base and operating pressure values can be seen in tab. 4.2.

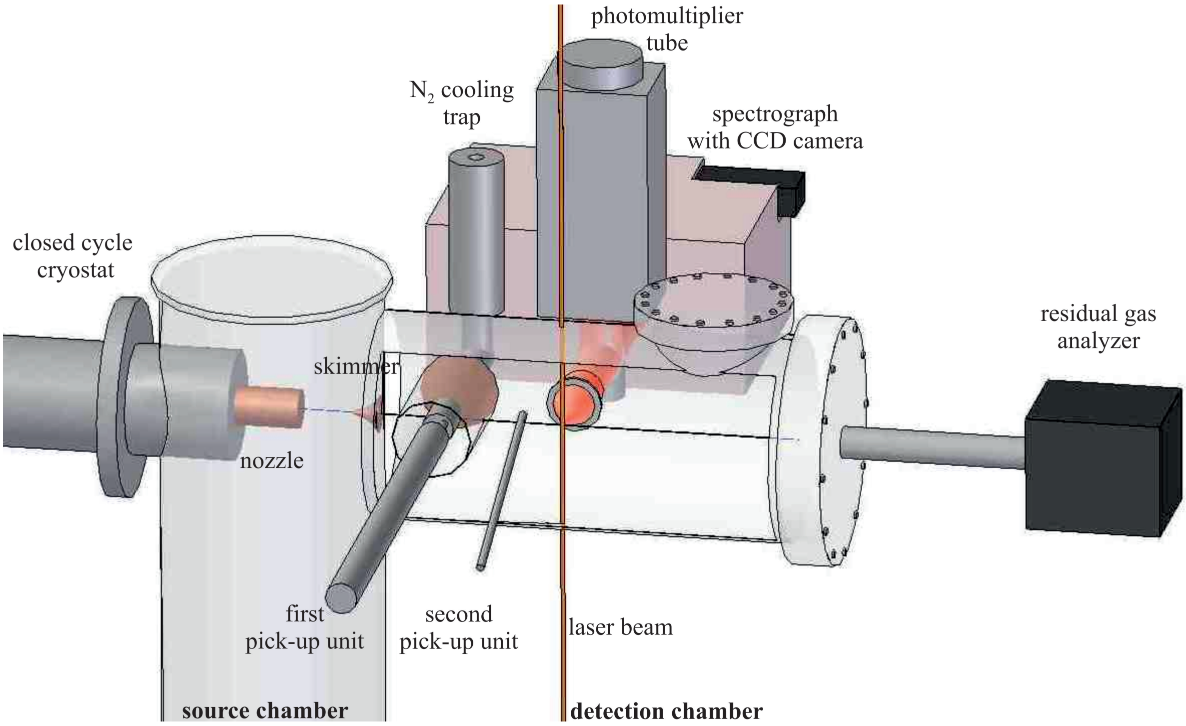

**Fig. 4.3:** Schematic depiction of the helium droplet apparatus.

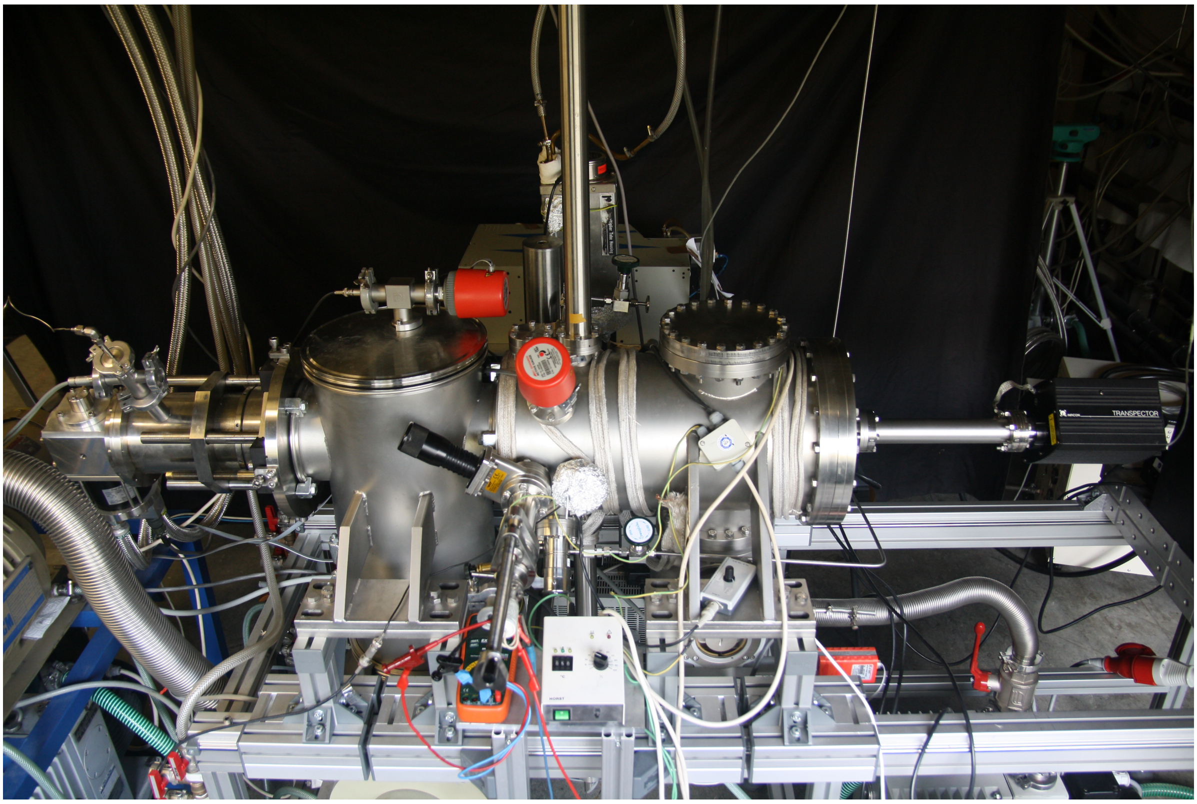

**Fig. 4.4:** Photo of the helium droplet machine for measurements with a pulsed droplet beam.

**Tab. 4.2:** Base and operating pressures in mbar. The operating pressure refers to beam generation at 20 K and 80 bar.

| chamber | base pressure | operating pressure at 20 Hz | operating pressure at 50 Hz |
|---|---|---|---|
| source chamber | $2 \cdot 10^{-8}$ | $5 \cdot 10^{-6}$ | $1 \cdot 10^{-5}$ |
| detection chamber | $2 \cdot 10^{-8}$ | $8 \cdot 10^{-7}$ | $1 \cdot 10^{-6}$ |

The source chamber is evacuated by a turbo molecular pump (pumping rate 2200 l/s, Pfeiffer TPH2200) and a booster pump unit composed of a rotary vane pump (Pfeiffer, DUO 060 A) and a roots pump (ULVAC PMB006CM). To check the pressure both vacuum chambers are equipped with an Active Inverted Magnetron Gauge / Penning Gauge (Edwards AIM-X-NW25). The prevacuum is measured at the exit of the turbo molecular pumps with Active Pirani Gauges (Edwards APG-M-NW16). The read out is undertaken by an Active Digital Gauge Controller (Edwards Enhanced Version).

The crucial component for working with a pulsed helium beam is an adequate valve. In this study an Even Lavie Valve (Even-Lavie Valve Type E.L.-5-C-2005) with a 60 $\mu$m orifice was used, which had been built especially for the generation of cold supersonic beams with helium. It is mounted to the second stage of a closed cycle cryostat (Sumitomo cold head RDK-408D2 and compressor unit CSW-71) and ensures a low energy dissipation for each pulse and a short opening time of about 20 $\mu$s. A more detailed description of the Even Lavie Valve is provided in [PRD+09]. The minimum nozzle temperature accessible with this setup is 7 K. A thermal resistor controlled by a remote control system (Lake Shore Cryotronics Model 331) is used for higher temperatures. This counter heating is performed with an accuracy of ± 0.2 K. The so-called “nozzle temperature” is measured at the second stage of the closed cycle cryostat with a silicon diode. In the presented experiments I worked with nozzle temperatures around 21 K and a stagnation pressure of 80 bar for the expansion of pre-cooled $^4$He (purity 99.9999 %, Linde Helium 6.0) through the valve. Furthermore the repetition rate influences the beam formation, as it causes an additional heating effect of the nozzle with increasing rate [PRD+09]. Although repetition rates up to 1 kHz are accessible with the Even Lavie Valve, the measurements were undertaken at 20 Hz or 50 Hz due to limitations by the pulsed laser systems. The entire cryostat and nozzle unit can be adjusted in the three spacial directions in order to align the beam axis. The pulsed beam of superfluid helium droplets exhibits a bimodal size distribution, but only the droplets with an average size between $10^4$ and $10^6$ helium atoms are of interest for this research, as only those can be doped with probe substances. The two vacuum chambers are separated by a conically-shaped wall with a skimmer at the center. It has an opening with a diameter of 6 mm. Mounted at a distance of 5 cm from the nozzle it assures free jet conditions by skimming the droplet beam when it leaves the source chamber.

In the detection chamber the doping of the droplets, the interaction with the laser and the signal detection take place. This second chamber is pumped by a turbo molecular pump (pumping rate 500 l/s, Pfeiffer TPH 500) and a rotary vane pump (Pfeiffer DUO 030 A). The apparatus is equipped with two pick-up units, one for solid probes and one for gases, enabling sequential doping of the superfluid helium droplets with different species. A solid substance, in this case anthracene, can be provided as a pellet in a cylindrical oven, which the droplet beam passes about 13 cm downstream from the skimmer via two opposite openings of 5 mm in diameter. Thereby the length of the pick-up cell $L$ corresponds to the oven's inner diameter of 26 mm. The oven is heated resistively using a tunable DC-voltage supply (Voltcraft, VLP 1405 pro) and a thermocouple (type k, Thermocoax) attached to the oven detects the temperature. A setup with airlock and gate valve enables the exchange of probe substances without breaking the ultra high vacuum. The whole pick-up unit is enclosed in a stainless steel cylinder, which blocks black body radiation emitted by the oven. An additional thermal shielding of the oven is achieved by a copper cylinder surrounding the entire pick-up unit. Both have openings along the beam axis for the helium droplets to pass through, 5 mm and 7 mm respectively. The copper shield is cooled to 77 K via an external reservoir and acts as a liquid nitrogen trap. It ensures the condensation of contaminating substances in the detection chamber, such as for example water.

The second pick-up unit is used for doping the superfluid helium droplets with argon (purity 99,996 %, Linde Argon 4.6). It consists of a stainless steel pipe of about 15 cm in length and 6 mm in diameter. The helium beam passes the pipe perpendicular to the gas flow via two holes of 4 mm, so that the inner diameter of the pipe equates to the length of the pick-up unit $L$. The gas cell can be installed at different positions on the beam axis depending on the desired pick-up sequence. For a post pick-up procedure the helium droplets first pass the liquid nitrogen trap and the oven, before entering the gas cell about 4 cm further downstream. Thus the doping of the droplets with anthracene is followed by the doping with argon. For a prior pick-up process it is the other way around and the gas cell is mounted such that the helium droplets pass it 1.3 cm before reaching the liquid nitrogen trap. The gas is introduced into the cell by means of a piping system with a gate valve and a metering valve. A very sensitive adjustment of the gas flow is indispensable to enable not only multiple but also single particle doping. This process is influenced by the beam formation as the pick-up cross section of a helium droplet is up to a factor of 100 larger in the pulsed beam than in the continuous beam under the formation conditions described above. This is due to the increased droplet size. Therefore a lower particle density in the pick-up cell is required to reach comparable doping of the droplets. A satisfactory performance could not be achieved with the leak valve (Leybold 283-41-V2) used in the continuous apparatus. It was replaced by a fine metering valve (Pfeiffer UDV 040), which can be operated manually or thermomechanically. It enables a stable gas flow between $1 \cdot 10^{-10}$ mbar l/s and to 600 mbar l/s, which was adequate for this research project.

The helium droplet beam crosses the excitation region 21 cm downstream from the skimmer, where it is intersected perpendicularly with the laser beam. The signal is detected at right angle to both droplet and laser beam (cf. chap. 4.2.2). To enable the analysis of cluster building processes in helium droplets a residual gas analyzer (Inficon Transpector H300M) is mounted on the beam axis at the rear of the machine. It works on the basis of a quadrupole mass filter and facilitates the alignment of the droplet nozzle. Mass to charge values can be detected in a range of m/z = 1 - 300 amu. The residual gas analyzer is switched of during measurements, because it produces background signal detectable with the applied detection units.

### 4.2.2 Laser System and Optical Detection

Three different nanosecond pulsed laser systems were used for the excitation in the ultraviolet range. For rough measurements a tunable dye laser (Lambda Physik Scanmate 2E) pumped by a Nd:YAG laser (Spectron Laser Systems SL803) could be applied. It is pumped with a repetition rate of 20 Hz and produces pulses with a spectral linewidth $\leq 0.2$ cm$^{-1}$ and a pulse duration of 10 ns. For frequency calibration the displayed wavenumbers were compared with the output of the continuous laser system measured with a high precision wavemeter (cf. chap. 4.1.2). In order to get an agreement of these values within ± 1 cm$^{-1}$ the calibration function $\nu_{cal} = 3,76156 + 1,00121\nu_l - 1,78078 \cdot 10^{-8}\nu_l^2$ is applied to the wavenumbers $\nu_l$ given by the laser software. The system can be run in two different operating methods in order to reach UV radiation. In one case the beam emitted by the Nd:YAG laser (1064 nm) is frequency doubled (532 nm) with a DKDP crystal before entering the dye laser. Then an additional second harmonic generation of the laser emitted by the dye laser system is required, which is accomplished with a unit consisting of a BBO III crystal and a compensator crystal. The UV light is separated from the fundamental using a set of Pellin-Broca prisms. In the second case the dye laser is pumped with the fourth harmonic (266 nm) of the Nd:YAG-laser beam achieved with two sequent DKDP crystals. This leads to radiation emitted by the dye laser already in the desired wavelength region. With application of a dye laser amplifier cuvette pulse energies of up to 700 $\mu$J were achieved, but fluctuations in the intensity in both cases of more than 20 % did not permit high precision measurements with this laser system.

The high resolution spectra shown in the following chapters were measured with two tunable dye lasers (Lambda Physik LPD 3002 and Lambda Physik FL 3002, respectively) each pumped with the 308 nm radiation of a XeCl* excimer laser (Lambda Physik LEXtra 100 and Lambda Physik LEXtra 200, respectively). Both systems emit radiation with a pulse durations between 5 ns and 50 ns and a spectral linewidth $\leq 0.2$ cm$^{-1}$. The excimer lasers were operated with a repetition rate of 20 Hz and 50 Hz, respectively. Output pulse energies are typically between 400 $\mu$J and 1.2 mJ, but can be increased by a factor of 10 when an additional amplifier cuvette is installed in the dye laser.

Frequency calibration of the dye lasers was undertaken using a spectrograph. By shifting the displayed wavelengths by a constant value to the red an agreement with the calibrated vacuum values of the transitions of $NO_2$ in the gas phase and of anthracene in helium droplets is achieved with an accuracy of ± 5 $cm^{-1}$. For the FL 3002 the wavelength shift for calibration is + 0.17 nm. For the LPD 3002 the dye laser control was configured during the research and, therefore, the calibration wavelength shift differs from + 0.1 nm before the modification to + 0.3 nm afterward. The pulsed laser beam is guided to the helium droplet apparatus via several quartz prisms, which causes a reduction of the pulse energy of about 20 %. It is coupled into the machine from above through a quartz window installed at Brewster angle (55,58°). To reduce laser stray light and thus improve the S/N-ratio, the beam continues through a blackened tube with 60 cm in length and 4 cm in diameter, which is fitted with baffles. An analogue setup is installed at the exit side of the beam.

For most of the experiments discussed in chap. 6 the pulsed lasers were attenuated. The analysis of the transitions' saturation behavior was conducted by recording the high resolution excitation spectrum three times with different photon fluxes.

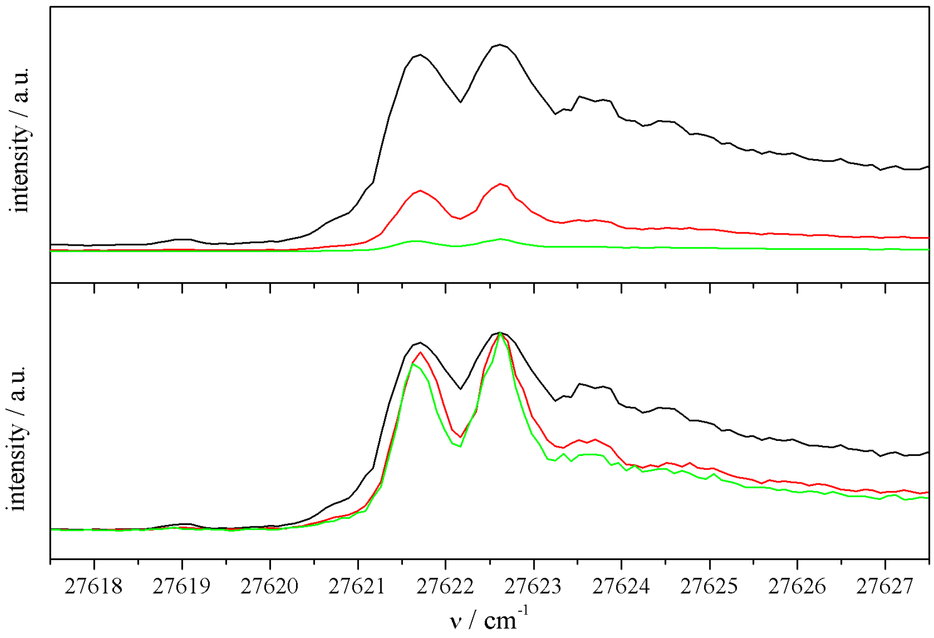

**Fig. 4.5:** Excitation spectrum of the $0_0^0$ transition of An in helium droplets recorded with the laser intensity increasing by an order of magnitude from the green to the black graph (upper panel: absolute signal intensties, lower panel: normalized plots).

Fig. 4.5 shows the electronic origin of An in helium droplets with absolute intensities (upper panel) and normalized to the most intense line (lower panel). Even if only the normalized graphs are shown in the figures of chap. 6 the spectra were recorded with the same attenuation of the laser intensity from the black to the green graphs as in this example depicted in fig. 4.5.

The signal is detected perpendicularly to the helium droplet beam and the laser beam. It is collected and imaged onto the photocathode of a PMT or the entrance slit of a spectrograph by means of two lenses with appropriate focal points. Two photomultipliers were used to record the laser-induced fluorescence. One (Hamamatsu R 943-02) is cooled to -25 °C and the other (Hamamatsu H5783P) is run at room temperature. To reduce scattered laser light an edge filter WG385 was installed in front of the photocathode for all measurements of anthracene and its clusters. Signals from the cooled PMT are amplified by a factor of 200 via a Preamplifier (Ortec VT 120A). A gated integrator and boxcar averager (Stanford Research Systems SR250), A/D converter (Stanford Research Systems SR245 or National Instruments NI USB-6009) and PC are used for the signal acquisition. The data storage and the graphical display is controlled by a LabView program.

To analyze emission the light was dispersed with a Czerny-Turner spectrograph (L.O.T.-Oriel MS257), which exhibits a focal length of 22 cm (F-number 3.9). It was operated with a 1200 lines/mm or a 3600 lines/mm grating, respectively. The detection of the dispersed emission was undertaken by a charge coupled device (CCD) camera (Andor iDus DU 420A-BU2) with a CCD chip consisting of 1024 × 256 pixels. To reduce thermal noise the CCD camera is operated at -80 °C. The signal is read out with a commercial software package (Andor Solis 4.9.30000.0). It is graphically displayed and stored on the laboratory PC.

## 4.2.3 Measurement Techniques

### 4.2.3.1 Fluorescence Excitation Spectra

For excitation spectra the laser-induced fluorescence is measured as a function of the wavenumber, offering information about the chromophore and its interaction with the environment (cf. chap. 3.1). A temporal synchronization of the laser control, the helium droplet beam formation and the signal acquisition is indispensable to ensure optimal excitation and detection times. Accurate delay times between the nozzle operation, the laser triggering and the readout of the signal data are ensured by a home built trigger generator (by Dr. U. Kensy and the electronic workshop of the Faculty of Chemistry and Pharmacy, University of Regensburg). These times, as well as the trigger frequency, are defined previous to a scan with the LabView program on the laboratory PC. They are transmitted via an USB interface to the trigger generator, which subsequently runs internally throughout the experiment. The delay times between the nozzle and laser operation are optimized for each scan. Typical values are about 570 - 590 $\mu$s, which corresponds to a mean velocity of the droplets of roughly 400 m/s. The communication with the pulsed laser systems is arranged by means of an external server connected to the laboratory PC via a LAN-(TCP/IP) interface.

At the beginning of a scan the laser is set to a predefined wavelength and kept fixed for a certain number of pulses corresponding to the desired averaging. The laser sends a software pulse back to the PC as soon as the wavelength is set, whereupon the signal acquisition starts. After a completed acquisition cycle the laboratory PC triggers the laser to tune to the next wavelength position. The signal data as well as the wavelength information is stored and graphically displayed on the laboratory PC for each step. This procedure is repeated until reaching the final wavelength. Starting and finishing wavelength and the increment are defined before the start of the measurement, as well as the number of pulses to be averaged per wavelength.

For the signal acquisition the boxcar integrator, which reads out the PMT data, is triggered by a photodiode recording decoupled laser light. For a good S/N-ratio the position and width of the acquisition gate is optimized for each scan. In the majority of cases the best results were achieved with a gate of about 40 ns opening at the arrival of the laser stray light. Two different A/D converters were used in this work to convert the analogue data from the boxcar integrator. At first the apparatus was equipped with the SR245, which was connected with the external laser server via an RS-232 interface. The digitized data was read out by the server with 15 Hz, which relates to the maximum rate for data transfer limited by the SR245. Subsequently the data was processed and send to the laboratory PC. The slow data transfer of the SR245 made it necessary to average the signal intensities corresponding to one wavelength before the A/D conversion. This was done by means of the exponential averaging offered by the boxcar averager.

However, it turned out that this exponential averaging of analogue data provoked a loss of spectral resolution as well as distortion of the signal intensities. This is due to the fact that the capacitor plates used for the averaging are not totally discharged after the data transfer with the result that the data is effected by the chosen averaging value.

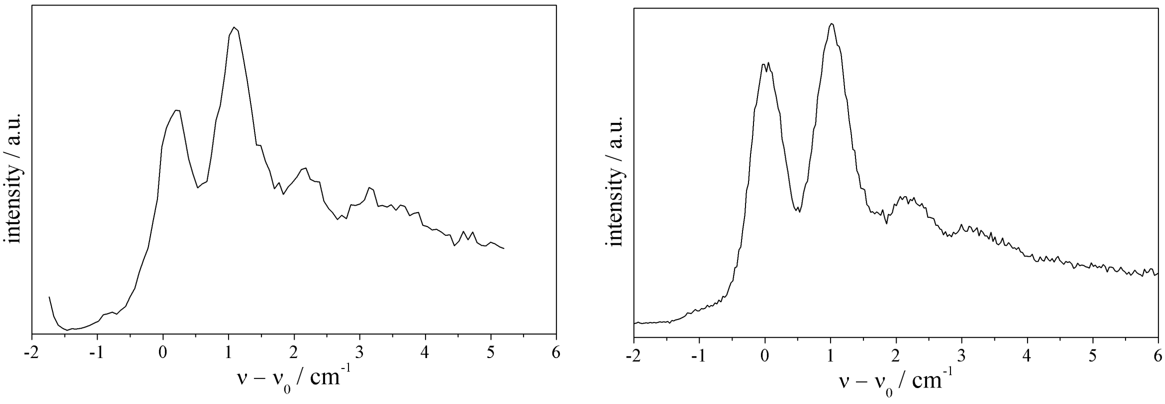

(a) Signal acquisition using a boxcar averager and the A/D converter SR 245.

(b) Signal acquisition using the A/D converter NI USB-6009.

**Fig. 4.6:** Fluorescence excitation spectrum of the electronic origin of anthracene in helium droplets at $\nu_0 = 27622$ cm$^{-1}$ before (a) and after (b) optimization of the signal acquisition.

Therefore the SR245 was replaced by the A/D converter NI USB-6009. It is connected directly to the laboratory PC via an USB interface. The LabView program was modified such as to enable the direct readout and processing of the digitized data. This process is no longer limited by the transfer rate, so that each signal pulse can be converted and stored individually. Instead of using the boxcar averager for the final intensity value the arithmetic mean is calculated by the LabView program from the separately stored data points. How these different techniques of measurement can affect the recorded signal data can be seen clearly in fig. 4.6. It shows the fluorescence excitation spectrum of the electronic origin of anthracene in helium droplets at $\nu_0 = 27622\ \mathrm{cm}^{-1}$ before (a) and after (b) the optimization of the signal acquisition. The distortion of signal intensities due to the exponential averaging of the boxcar is most obvious at the red end of the spectrum in fig 4.6 (a). When recording a new spectrum the exponential averager of the boxcar still includes data from the former measurement, which leads to an increased output signal. Moreover, the signal intensity of the fine structure of anthracene's electronic origin in helium droplets shows the same distortion. Due to the exponential averaging the line at $\nu - \nu_0 = 0\ \mathrm{cm}^{-1}$ appears reduced in signal intensity, while the line shifted $1\ \mathrm{cm}^{-1}$ to the blue appears heightened. These effects are the worst when averaging over few signals per data point. The excitation spectrum of fig. 4.6 (a) was measured with an averaging of only 30 signals per data point. By changing the A/D converter and the averaging process these problems could be solved.

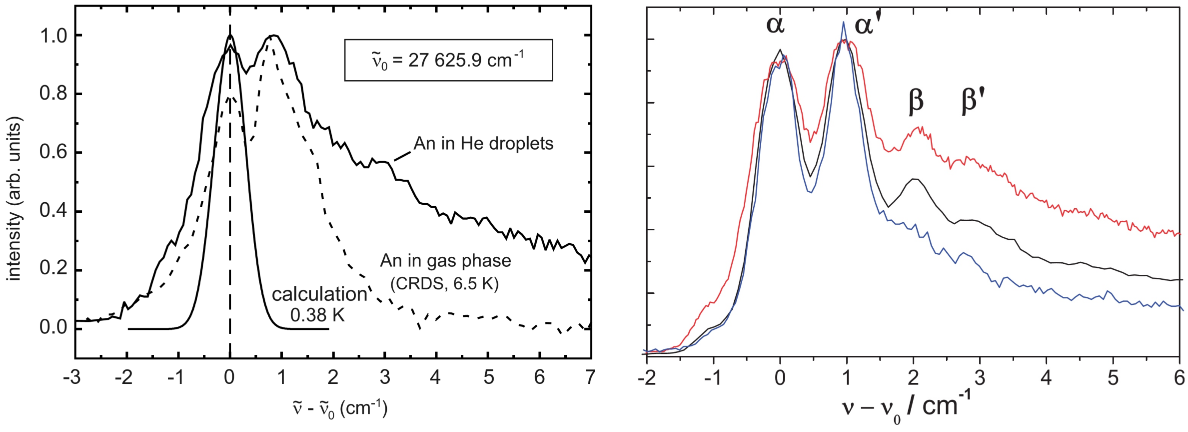

(a) Krasnokutski et al.: Chem. Phys Lett. 2005 ([KRH05])

(b) Pentlehner, Slenczka: Mol. Phys. 2012 ([PS12])

**Fig. 4.7:** Former fluorescence excitation spectra of the electronic origin of anthracene in helium droplets.
(a) was measured with a continuous droplet beam intersected with a pulsed laser. The detailed description of the experimental setup can be seen in [RKH+04].
(b) was measured with the pulsed helium apparatus described in this chapter before the optimisation of the signal acquisition. The spectra were measured with varying laser intensities (blue: lowest intensity; red: highest intensity).

The recorded signal intensity became independent of the data averaging and, in addition, the spectral resolution was improved significantly. The improvement in the spectral resolution also becomes obvious when comparing the spectrum of fig 4.6 (b) with former spectra of this transition, which can be seen in fig. 4.7. (a) shows the first measurement of anthracene in superfluid helium droplets compared with a gas phase spectrum and a calculation [KRH05]. (b) was measured with the apparatus described in this chapter. It displays the best spectral resolution accessible with a signal acquisition using the A/D converter SR245 [PS12].

#### 4.2.3.2 Dispersed Emission Spectra

To measure dispersed emission spectra the frequency of the excitation laser is kept fixed at a molecular resonance and the fluorescence light is fed into the spectrograph. As the accuracy of the frequency setting of the pulsed lasers is in the range of the line widths of some of the investigated transitions the excitation wavelength is not simply given to the controlling PC. Instead an excitation spectrum is recorded stopping the laser exactly at the frequency, which coincides with the molecular transition of interest. Before starting the measurement of the dispersed emission the spectrograph is set to a center wavelength by the Andor camera software. All spectra in this research project were recorded in full vertical binning mode of the CCD-chip. In this mode the charges of all pixels of one column are integrated on the CCD-chip by the camera hardware prior to readout. In doing so, electronic noise generated by the readout of the camera is reduced as the pixels are not regarded separately. Finally the fluorescence intensity is represented by 1024 data points forming the emission spectrum.

To consider background signal the dispersed emission spectra were measured with a background correction. For this purpose a background spectrum was recorded before each scan with identical conditions as the emission spectrum except for the argon supply being disrupted. If the excitation wavelength of the laser was not located in the range of the emission spectrum the background signal was taken with the laser shut off. For the correction of the emission spectrum the background was subtracted by the camera software. Signals from cosmic radiations were also removed automatically by the camera software, which eliminates single pixel events. However, as the accumulation times, which had to be chosen due to the poor duty cycle with the pulsed setup, were rather long, some signals from cosmic events were not eliminated by the software and had to be removed by hand afterward. This was only applied to high signals consisting of only one point of measurement. Typical for the measurement of emission spectra using 50 Hz pulsed lasers were accumulation times of 4 x 900 s or even 6 x 900 s.

The positioning accuracy of the spectrograph's grating does not allow for a reproducible approach of a certain wavelength. Therefore, a wavelength calibration was performed for each new wavelength setting by recording the stray light of a pulsed dye laser. The generated calibration function assigns each of the 1024 columns of the CCD chip to a specific wavelength. Most emission spectra shown in this work were recorded with the 1200 lines/mm grating and a center wavelength of 395 nm. For the corresponding wavelength region the calibration function is essentially linear with a small quadratic correction, showing that the spectrograph disperses the fluorescence light into similar wavelength intervals $\Delta\lambda$. To convert the emission spectra from a wavelength into a wavenumber scale a Jacobi transformation has to be applied due to the nonlinear relation between the parameters $\Delta\lambda$ and $\Delta\nu$. For each $\Delta\lambda$ and $I_{\Delta\lambda}$ the corresponding $\Delta\nu$ and $I_{\Delta\nu}$ is calculated. This conversion yields intensity values, which can be plotted versus a linear wavenumber scale.

## 4.3 Comparison of continuous and pulsed helium droplet beams

The two apparatus used in this work have similar setups. The principal difference lies in the helium expansion, which is continuous in one case and pulsed in the other, each method offering advantages and disadvantages. The best S/N-ratio can generally be achieved with the combination of a continuous droplet source and a cw laser. With this setup the laser excitation of the chromophore is not influenced by time fluctuations. Additionally this process shows the best duty cycle for excitation spectroscopy as well as for dispersed emission measurements.

However, if the research interest includes substances with transitions in the blue or UV range, pulsed laser systems are preferable. Second, third or fourth harmonic generation can be accomplished more easily with these, so that ultraviolet radiation becomes accessible. Moreover, the laser pulses possess a higher power. This is significant especially for the measurement of weak transitions. Pulsed lasers are also beneficial for fast frequency scanning and for time-resolved spectroscopy. If these laser systems are used the worse duty cycle can be compensated partially by combining the laser system with a synchronised pulsed helium droplet beam. This is due to the higher droplet density per pulse, which is increased by about a factor of 20 compared with a continuous helium droplet beam. For a good S/N-ratio it is necessary to additionally conduct the signal acquisition as a pulsed procedure. If a continuous detection unit like a CCD camera is used together with a pulsed laser and droplet beam the duty cycle is by about a factor of $10^{-6}$ lower compared with the entirely continuous setup. This value is calculated for a repetition rate of 20 Hz and a signal duration of 50 ns, which is estimated from the laser pulse duration and typical nanosecond fluorescence decay times. Hence, within one second of detection time the signal duration is only about 1 $\mu$s.

For this reason, the phthalocyanine clusters with transitions in the red region of the visible spectrum were measured with the entirely continuous setup. In contrast, pulsed lasers and a pulsed helium droplet source were used for the anthracene clusters due to their transitions in the ultraviolet range. A more detailed comparison of pulsed and continuous helium droplet beams and the corresponding experimental analysis can be found in [Pen10].

## 4.4 Analysis of the Droplet Doping

Inhomogeneous clusters are formed inside helium droplets by coagulation after the individual pick-up of different particles, as described in chap. 2.3. In this work the clusters under investigation consist of one chromophore and an increasing number of water molecules or argon atoms, respectively. To achieve single particle doping in the case of the chromophores the oven temperature is adjusted to the optimum fluorescence signal of pure phthalocyanine (606 K) or anthracene (301 K), respectively. Corresponding to the Clausius-Clapeyron equation for sublimation this equates to a vapor pressure $p$ in the pick-up cell of $1.34 \cdot 10^{-4}$ mbar for phthalocyanine [SBGI07] and $1.14 \cdot 10^{-5}$ mbar for anthracene [OS98], respectively. Equ. 4.1 shows the integrated form of the Clausius-Clapeyron equation approximated for an ideal gas [Wed97], wherein $p_0 = 1$ atm is the standard pressure, $R$ the gas constant, and $\Delta_{sub}H_T$ and $\Delta_{sub}S_T$ the standard heat and entropy of sublimation, respectively.

$$ln\frac{p}{p_0} = -\frac{\Delta_{sub}H_T}{RT} + \frac{\Delta_{sub}S_T}{R} \tag{4.1}$$

The accuracy of the calculated values given above depends significantly on the literature data for $\Delta_{sub}H_T$ and $\Delta_{sub}S_T$ and on the accuracy of the read out oven temperature. Comparing the published values for $\Delta_{sub}H_T$, which vary considerably [OS98], the difference in the pressure values obtained for single particle doping is not surprising. In the following explanation the pick-up density of the chromophore is considered as constant (single doping) and the particle is neglected when discussing the analysis of the cluster size.

Argon or water doping is conducted to varying degree depending on the desired cluster size. For the analysis of the cluster stoichiometry, the pick-up probability $P_k$ of a helium droplet passing a pick-up cell must be known. It is determined by a Poisson distribution as described in chap. 2.3.

$$P_k(n) = \frac{(\sigma nL)^k}{k!}e^{-\sigma nL} \tag{4.2}$$

The fluorescence intensity $I_k$ of a transition belonging to a cluster with $k$ particles is proportional to the probability $P_k$ of the creation of such a cluster during the droplets flight through the pick-up cell. The graphic representation of $I_k$ as a function of the varying particle density in the pick-up cell $n$ should therefore yield a graph, which can be fitted according to equ. 4.2. The resulting $k$ corresponds to the fit which shows the best agreement with the data. Thus the spectral features can be assigned to a specific cluster size. For a large pick-up rate this result has to be corrected according to equ. 2.7.

Since the pressure inside the gas cell $p$, which determines the particle density $n$, is not directly accessible the cluster size analysis is undertaken using signals of the residual gas analyzer as an indirect measure. The dimensions of the experiment imply that the pick-up cell is practically a Knudsen cell. Therefore the gas pressure $p$ inside it is proportional to the particle flux from it into the detection chamber. The latter is linearly correlated to the gases partial pressure within the vacuum chamber, which can be detected with the residual gas analyzer. Therefore, it is assumed that the mass selective power signal of the residual gas analyzer $I_{mass}$ is proportional to the particle density $n$ for an ideal gas in the pick-up cell and can be applied for the analysis of the cluster size via Poisson distribution. For this purpose equ. 2.4 is modified taking into account the proportionality factor $I_k^0$ between $P_k(n)$ and $I_k$ as well as the proportionality factor $\alpha$ between $n$ and $I_{mass}$.

$$I_k = I_k^0 \frac{(\alpha\sigma L \cdot I_{mass})^k}{k!} e^{-\alpha\sigma L \cdot I_{mass}} \tag{4.3}$$

The constants $I_k^0$ and $(\alpha\sigma L)$ are numerically identified through the fitting procedure for a specific $k$. This method was used to analyze the cluster stoichiometries and assign the different spectral features. It was also applied for large clusters with the modified form of equ. 2.7:

$$k = \frac{N_0}{c}\left[1 - \left(1 - \frac{c\alpha\sigma L}{3N_0} I_{mass}\right)^3\right] \tag{4.4}$$

## 4.5 Chemicals and Laser Dyes

Phthalocyanine (purity 98 %) was purchased from Sigma-Aldrich and used without further purification. Anthracene (purity 99 %) was purchased from Merck Schuchardt. To dispose of impurities, especially water, it was sublimated and kept several days in a vacuum desiccator before measurements.

The laser dyes used according to the desired excitation wavelength range were provided by Radient Dyes. The applied dyes and their characteristics are listed in Tab. 4.3. For the preparation of DCM the dye is dissolved in a small amount of methanol or benzyl alcohol before mixing it with ethylene glycol. The solvents (purity $\geq$ 99.5 %) were purchased from Merck and Acros Organics.

**Tab. 4.3:** Laser dyes and their characteristics as used in this work.

| dye | range / nm | pump source | solvent | concentration / g/l |
|---|---|---|---|---|
| DCM | 600 - 695 | $Ar^+$ (514 nm) | Ethylene Glycol | 0.9 |
| Pyridine 2 | 685 - 760 | Nd:YAG (532 nm) | Methanol | 0.128 |
| BPBD | 354 - 388 | Nd:YAG (266 nm) | Cyclohexane | 1.773 |
| DMQ | 350 - 378 | XeCl* (308 nm) | P-Dioxane | 0.23 |

# 5 Phthalocyanine Water Clusters in Helium Droplets

This study continues an extensive research project on high resolution spectroscopy of Phthalocyanine (Pc) in helium nanodroplets undertaken within the last decade (see e.g. [SDHT01, Leh04, PRD$^+$09, Rie11, Chr13]). Pc water clusters formed inside helium droplets were investigated with fluorescence excitation spectroscopy and Stark spectroscopy in order to gain information about the stoichiometry, the rigidity and, if possible, also the configuration of the individual cluster isomers. The influence of the homogeneous external electric field on the signals of the cluster spectra in helium droplets was investigated with the laser polarization perpendicular and parallel to the field. All experiments described in this chapter were performed with the continuous helium droplet apparatus characterized in chap. 4.1. The droplets are of medium size with about $2 \cdot 10^4$ helium atoms per droplet (nozzle temperature $T_0 = 10.3$ K, stagnation pressure $p_0 = 20$ bar).

## 5.1 Introduction

Phthalocyanine ($C_{32}N_8H_{18}$) is a highly symmetric, macrocyclic aromatic compound with a deep blue colour. Its planar structure, which can be seen in fig. 5.1, belongs to the point group $D_{2h}$. The substance and its derivatives are mostly used in dyes. They account for 25 % of the organic pigment production [LÖ0]. Other fields of application are for example organic semiconductor materials (see e.g. [KSK04, BZB$^+$07, CPG$^+$09]) or catalysts (see e.g. [SS75, Kro72, HNH$^+$84]).

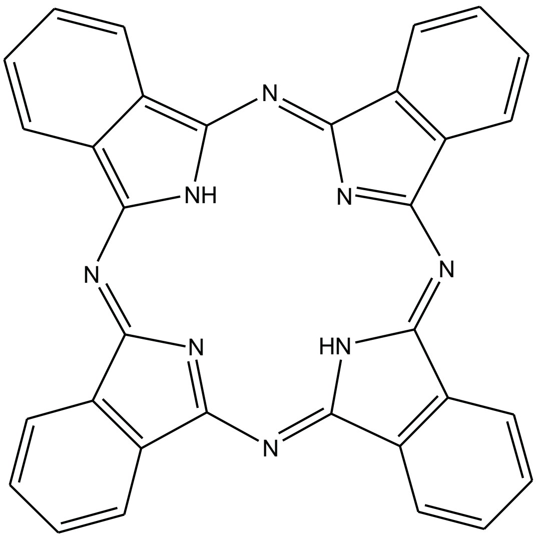

**Fig. 5.1:** Chemical structure of free-base phthalocyanine.

The physical and chemical properties of Pc and its derivatives have been extensively studied since the discovery of the substance in 1907 [BT07]. They are reviewed for example in [LÖ0, MT63, MT83]. Free-base Pc is well adapted for spectroscopic research as it offers high chemical and thermal stability, a strong absorption in the visible range and a fluorescence quantum yield of $\Phi_f \approx 0.7$ [VVR71]. Its laser induced fluorescence and dispersed emission have been analyzed in supersonic jet measurements [FWL78, FHL80, FHL81, MB87, PJ99] and in matrix experiments [BE79, HRV82, MDM$^+$11]. Profound spectroscopic analysis has been undertaken in helium droplets as well, both on free-base Pc and on many of its derivatives [SDHT01, DS01, SKMV02, HLTV02, LS03, LSK$^+$04, LS04b, LS04a, PRD$^+$09, PRV$^+$11]. Furthermore spectra of Pc clusters and metal Pc clusters with noble gas atoms or small molecules in supersonic jet experiments [MB87, ChYK00] and in helium droplets [LS04b, LSS07, KGMNS$^+$07] have been published.

Pc shows the typical spectroscopic signature of a rigid molecule. In fluorescence excitation and dispersed emission spectra it exhibits a similar vibrational structure with sharp signals. This can be seen in fig. 5.2 showing the excitation spectrum (upper pannel) and the dispersed emission spectrum (lower pannel) of bare Pc inside helium droplets [Leh04]. The measurements were undertaken in a continuous droplet beam and emission was recorded after excitation of the $0_0^0$ transition of Pc in helium droplets at $\nu_0 = 15088.9\ \mathrm{cm}^{-1}$. The signals in the excitation spectrum consist of a single, asymmetric ZPL and a struc-

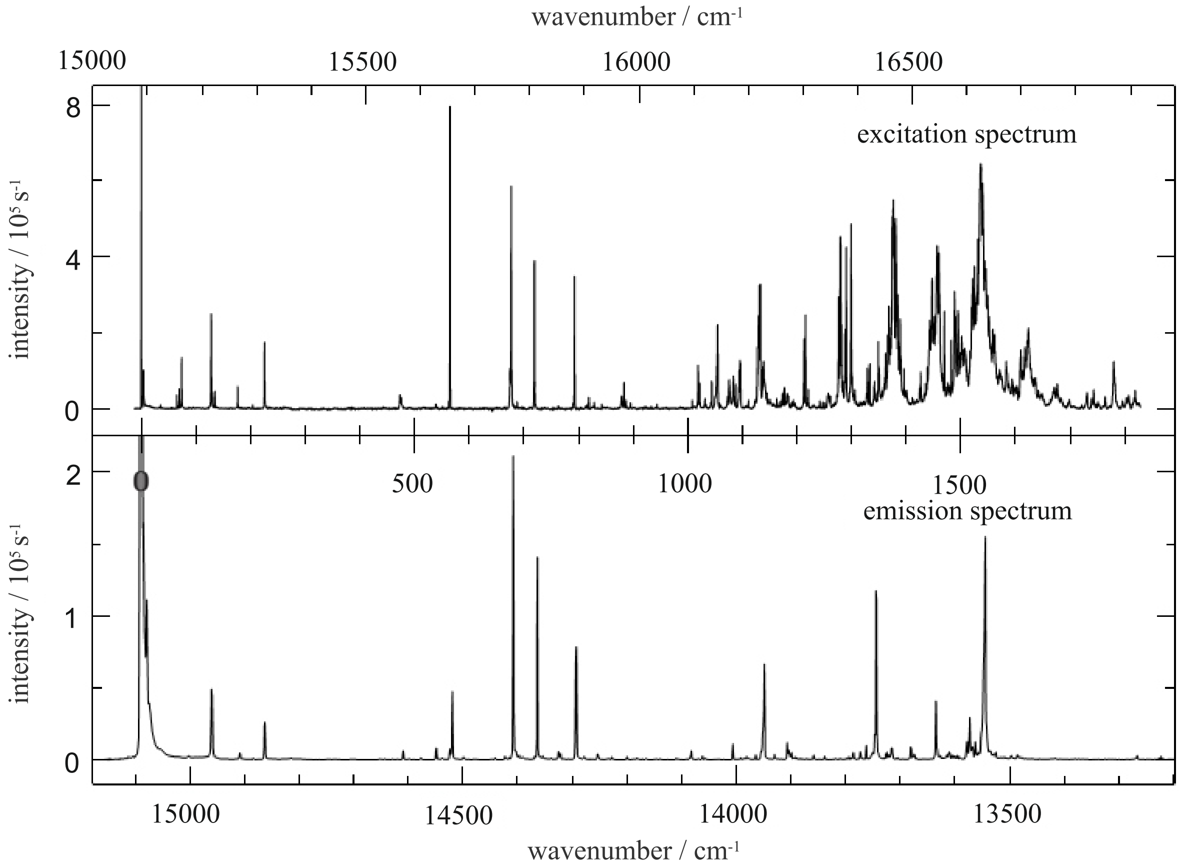

**Fig. 5.2:** Exciation spectrum (upper pannel) and dispersed emission spectrum (lower pannel) of free-base Pc in a continuous beam of helium droplets (from [Leh04]). The emission was recorded after excitation of the $0_0^0$ transition at $\nu_0 = 15088.9$ cm$^{-1}$.

tured PW. It is assumed that the line shape of the ZPL reflects the size distribution of the helium droplets, which leads to an inhomogeneous distribution broader than the rotational substructure [SDHT01]. The excitation spectrum of Pc measured with a pulsed helium droplet beam corresponds basically to the one from the cw experiment except for different line shapes of the ZPLs as a result of the different size distribution of the helium droplets [SKMV02, PRD$^+$09]. Concerning the quantity and the relative positions of the signals a similarity to the gas phase spectrum is also evident.

The solvation dynamics of Pc in helium droplets is illustrated in the configuration coordinate model of fig. 5.3. It shows that the ground state and the first excited state of Pc both exhibit a double minimum potential in helium droplets. The two minima in the $S_0$ and the $S_1$ correspond to different helium configurations of the first solvation layer, which is located around Pc [LS03, WHKW05]. This manifests itself in a splitting of the emission spectrum of Pc in helium droplets [LS03, Pen10]. The double minimum potential of the ground state becomes obvious in pump-probe experiments revealing a relaxation rate of about $1.9 \cdot 10^5\ \mathrm{s}^{-1}$ for the $S_0$ [Leh04, ST08]. Thus, the splitting observed in the spectra of Pc in helium droplets provides information about the relaxation dynamics of the helium environment and illustrates the efficient coupling of the chromophore to the otherwise very gentle droplet environment.

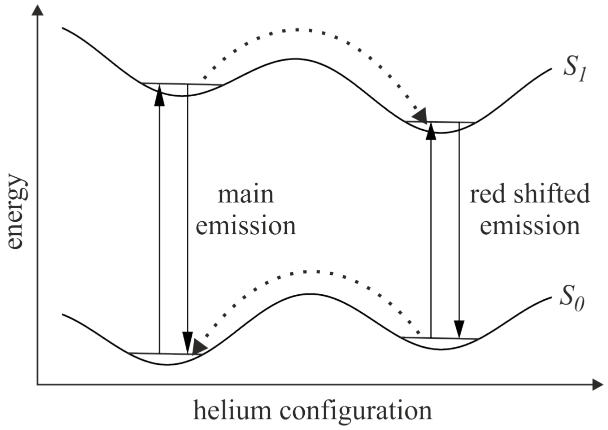

**Fig. 5.3:** Configuration coordinate model according to [LS04b]. The varying configuration corresponds to different structures of the first helium solvation layer around Pc in helium droplets.

## 5.2 Excitation Spectrum

Van der Waals clusters of Pc with water have already been investigated in supersonic jet experiments [MB87]. The excitation spectrum shows that the electronic transitions of the Pc($H_2O$) clusters are shifted up to 70 $\mathrm{cm}^{-1}$ to the red compared to the electronic origin of bare Pc. This red shift could also be observed in first measurements of Pc$(H_2O)_k$ clusters in helium droplets [Chr13]. Fig. 5.4 shows the fluorescence excitation spectrum of Pc$(H_2O)_k$ clusters in helium droplets in the range from 15008 $\mathrm{cm}^{-1}$ to 15095 $\mathrm{cm}^{-1}$. In addition to the electronic origin of bare Pc signals belonging to Pc($H_2O$) and Pc$(H_2O)_2$ clusters are observed. They are assigned as indicated in fig. 5.6 and tab. 5.1 of the following section.

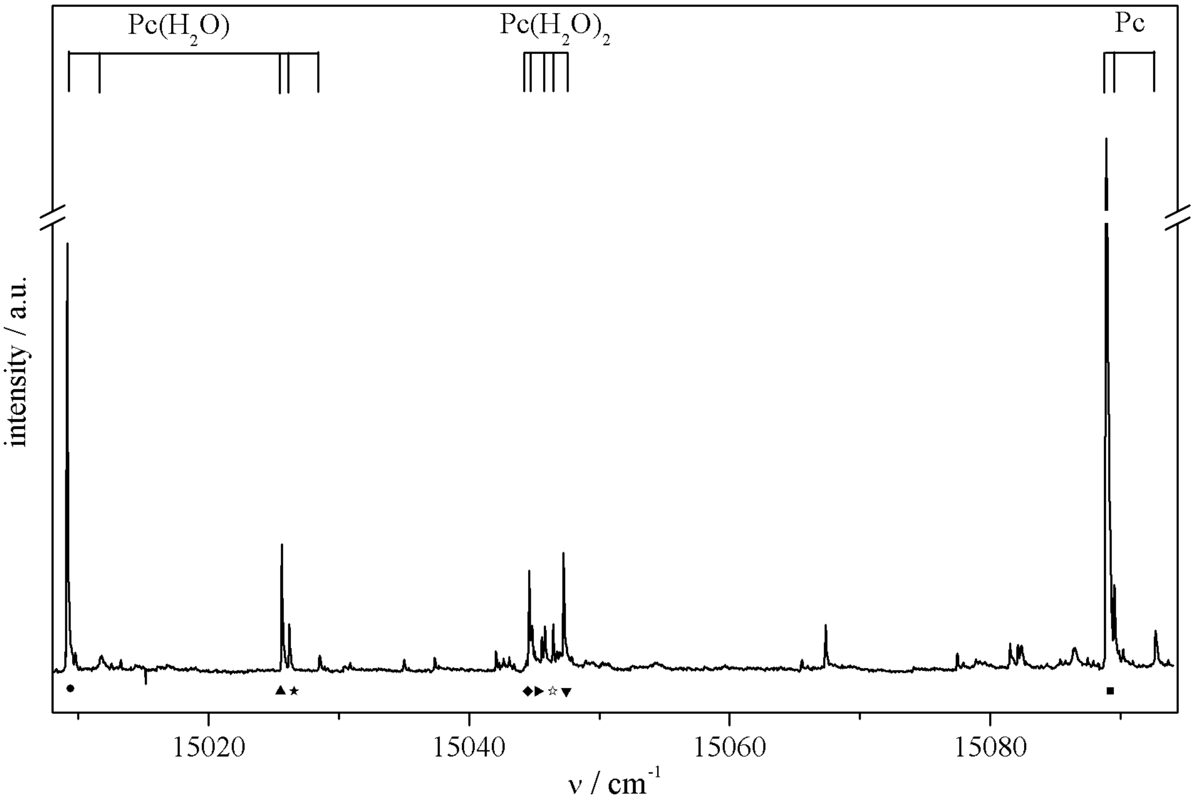

**Fig. 5.4:** Excitation spectrum of Pc and Pc($H_2O$)$_k$ clusters measured in a continuous beam of helium droplets. The particle density of water in the pick-up cell was optimized for maximum intensities of the Pc($H_2O$)$_2$ transitions. The van der Waals clusters were formed inside the helium droplets after a post pick-up process.

The clusters containing one Pc and $k$ water molecules were formed in a post pick-up process, i.e. water molecules coagulated around the chromophore inside the droplets. For this spectrum the particle density of water was adjusted in such a way in the gas pick-up cell as to result in the maximum intensity of the transitions belonging to the Pc($H_2O$)$_2$ clusters.

The marked signals in fig 5.4 are the ones chosen for further investigations with Stark spectroscopy. Fig. 5.5 shows these selected excitation signals of Pc and Pc($H_2O$)$_k$ clusters on an expanded scale. The measurements were undertaken with 250 datapoints per 1 cm$^{-1}$. All panels show a frequency range of 1.2 cm$^{-1}$ and the assignment to the cluster stoichiometry is as indicated in tab. 5.1. The spectra are arranged according to decreasing transition energies.

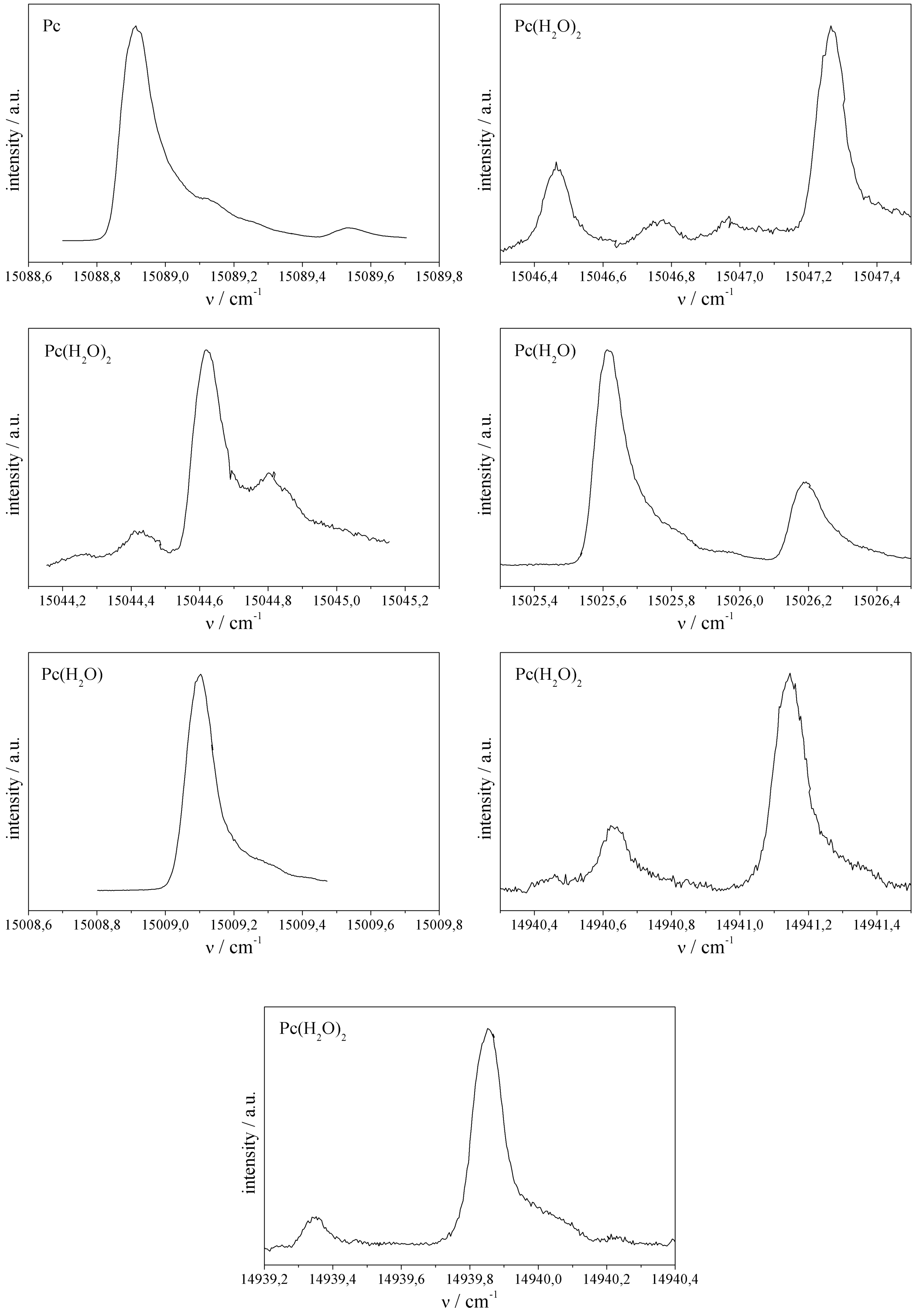

**Fig. 5.5:** Signals of the excitation spectrum of Pc and Pc($H_2O$)$_k$ in helium droplets on an expanded scale measured with 250 datapoints per 1 cm$^{-1}$.

In addition to the spectral features appearing in the excitation spectrum of fig. 5.4 transitions in the range of 14939.2 $\text{cm}^{-1}$ to 14941.5 $\text{cm}^{-1}$ are regarded as well. Their existence and assignment to $\text{Pc(H}_2\text{O)}_2$ clusters is known from ref. [Chr13]. Each excitation spectrum was recorded for optimized water doping corresponding to the respective cluster stoichiometry. The spectra show that the main signals all exhibit a similar line width of about 0.1 $\text{cm}^{-1}$ and an asymmetric line shape similar to the one of the ZPL of Pc's electronic origin in helium droplets.

## 5.3 Assignment of the Clusters

The helium droplets were doped with Pc and water in two separate pick-up units, as described in chap. 4.1.1. To assign the excitation signals of fig. 5.4 to certain cluster stoichiometries, the spectrum was measured several times under varying pick-up conditions. While the particle density of Pc in the first pick-up cell was left constant to ensure single particle pick-up, the water density in the second pick-up cell was successively increased. The assignment of the clusters can then be derived from the correlation between the particle density $n$ of water in the second pick-up cell and the signal intensity $I_k$ of the different transitions in the spectrum as explained in chap. 2.3.

In fig. 5.6 the signal intensities of different transitions are plotted as functions of the signal of the residual gas analyzer at 18 amu $I_{mass}$. As shown in chap. 4.4 the analyzer's mass selective signal $I_{mass}$ is proportional to the particle density $n$ in the pick-up unit and, therefore, an adequate measure for this application. Poisson distributions in the form of equ. 4.3 are fitted to the data sets. For this purpose the parameters $k$, $I_k^0$ and $(\alpha\sigma L)$ are varied for each fitting procedure in order to reach the best agreement with the data points. The fitting was performed with the data analysis procedure of OriginPro 8. From these Poisson distribution fits the mean value of the parameter $(\alpha\sigma L)$ was determined as $9.1 \cdot 10^8\ \text{A}^{-1} \pm 1.0 \cdot 10^8\ \text{A}^{-1}$. It was kept fixed on this value for a second fitting of the Poisson distribution to the data sets. This procedure yielded the curves plotted as solid lines in fig. 5.6. The data sets and the fitted graphs are arranged according to

$k$ showing whether the corresponding signal belongs to bare Pc ($k = 0$), a Pc($H_2O$) cluster ($k = 1$) or a Pc($H_2O$)$_2$ cluster ($k = 2$). The dotted lines in fig. 5.6 mark the positions of the maxima for $k = 1$ and $k = 2$ at $1.1 \cdot 10^{-9}$ A and $2.2 \cdot 10^{-9}$ A, respectively. $I_{mass}^{max} = k/(\alpha\sigma L)$ applies according to equ. 2.5 in chap. 2.3. However, the pick-up and coagulation cross section $\sigma$ can not be deduced from this as the proportionality factor $\alpha$ between $n$ and $I_{mass}$ is not known.

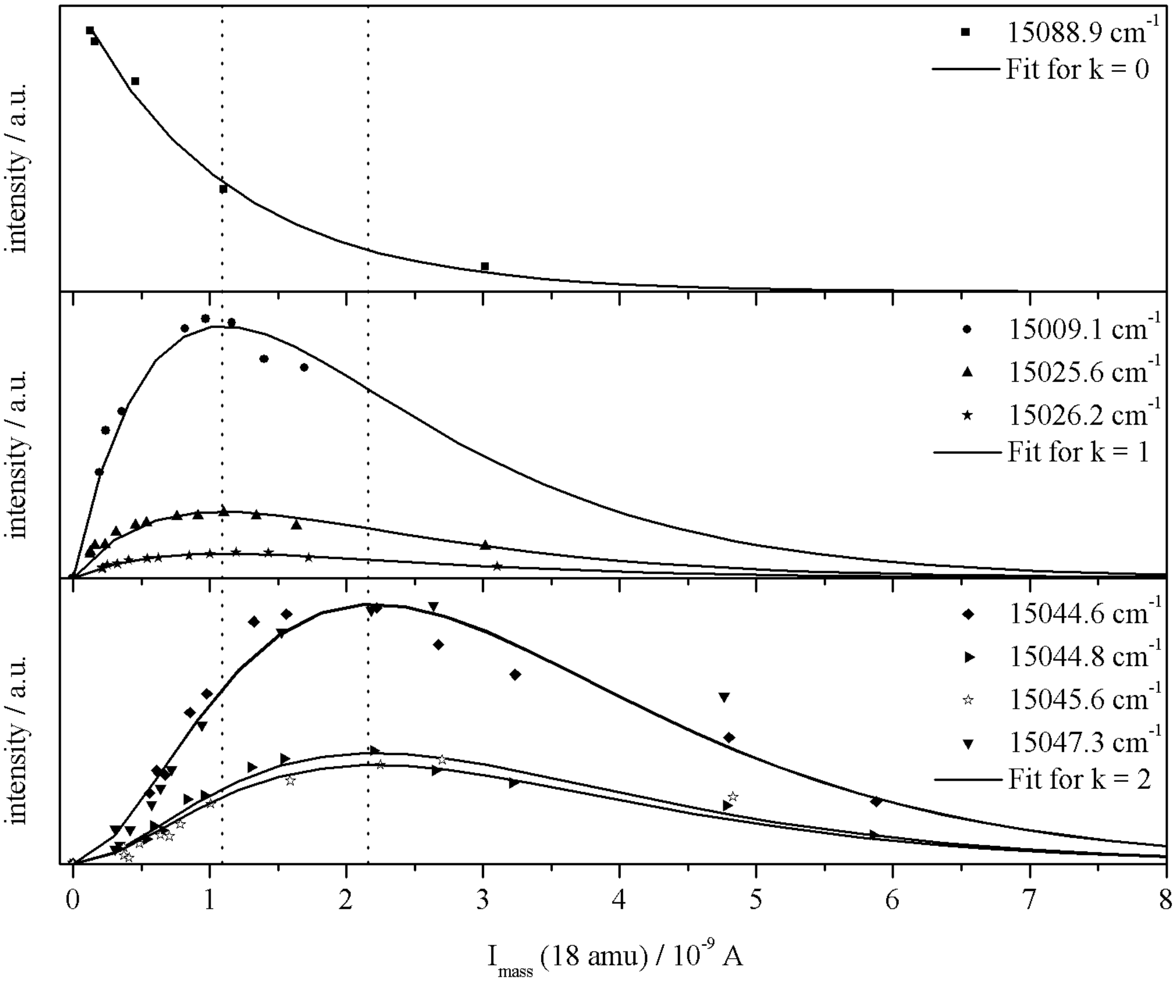

**Fig. 5.6:** Intensities of the signals in the excitation spectrum of Pc and Pc($H_2O$)$_k$ in helium droplets as functions of the signal $I_{mass}$ of the residual gas analyzer at 18 amu (mass of water). The solid lines show Poisson distributions fitted to the data points according to equ. 4.3 with the denoted $k$. The dotted lines mark the positions of the fitted graphs' maxima.

In addition to the information yielded by the Poisson fits of fig. 5.6 earlier investigations are also taken into account for the assignment of the signals in the excitation spectrum of fig. 5.4. Bare Pc is well investigated and the signal shifted 3.8 cm$^{-1}$ to the blue of the

ZPL of the electronic origin in helium droplets is attributed to the PW of the $0_0^0$ line [SDHT01, HLTV02]. The weak signal at 15089.5 $\mathrm{cm}^{-1}$ is assigned to the electronic origin of a Pc isotopomer with a $^{13}$C atom replacing one of the $^{12}$C atoms [LSK+04]. Moreover, earlier measurements of the dispersed emission of $\mathrm{Pc(H_2O)}_k$ clusters indicate that the small signals at 15011.8 $\mathrm{cm}^{-1}$ and 15028.5 $\mathrm{cm}^{-1}$ are PWs belonging to the transitions at 15009.1 $\mathrm{cm}^{-1}$ and 15025.6 $\mathrm{cm}^{-1}$, respectively [Chr13]. Thus, they also originate from transitions of clusters with one water molecule attached to Pc and are therefore assigned to $\mathrm{Pc(H_2O)}$ in fig. 5.4.

Tab. 5.1 lists the main spectral features of the excitation spectrum of $\mathrm{Pc(H_2O)}_k$ clusters in helium droplets according to their assignment to certain cluster stoichiometries. The frequency shift $\nu - \nu_0$ is given compared to the $0_0^0$ transition of bare Pc in helium droplets at $\nu_0 = 15088.9$ $\mathrm{cm}^{-1}$. The relative signal intensity is given with respect to the strongest line found for each cluster stoichiometry.

**Tab. 5.1:** Assignment of the signals in the excitation spectrum of Pc and $\mathrm{Pc(H_2O)}_k$ clusters in helium droplets (fig. 5.4). $\nu - \nu_0$ denotes the frequency shift compared to the $0_0^0$ transition of bare Pc in helium droplets at $\nu_0 = 15088.9$ $\mathrm{cm}^{-1}$. The relative intensity of each line is given with respect to the most intense signal of the respective cluster size. For the assignment also earlier investigations are considered: [1] refers to ref. [Leh04] and [2] to ref. [Chr13].

| k | $\nu$ / $\mathrm{cm}^{-1}$ | $\nu - \nu_0$ / $\mathrm{cm}^{-1}$ | rel. int. | assignment |
|---|---|---|---|---|
| 0 | 15092.7 | 3.8 | 0.05 | PW [1] |
| 0 [1] | 15089.5 | 0.6 | 0.09 | $0_0^0$ with one $C_{13}$ [1] |
| 0 [1] | 15088.9 | 0 | 1 | $0_0^0$ [1] |
| 1 | 15028.5 | -60.4 | 0.06 | PW [2] |
| 1 | 15026.2 | -62.7 | 0.14 | $0_0^0$ [2] |
| 1 | 15025.6 | -63.3 | 0.32 | $0_0^0$ [2] |
| 1 | 15011.8 | -77.1 | 0.06 | PW [2] |
| 1 | 15009.1 | -79.8 | 1 | $0_0^0$ [2] |
| 2 | 15047.3 | -41.6 | 1 | |
| 2 [2] | 15046.5 | -42.4 | 0.46 | |
| 2 | 15045.6 | -43.3 | 0.44 | |
| 2 | 15044.8 | -44.1 | 0.44 | |
| 2 | 15044.6 | -44.3 | 0.86 | |

## 5.4 Stark Spectra

To gain information about the rigidity and configuration of the Pc($H_2O$)$_k$ clusters in helium droplets they were investigated with Stark spectroscopy applying a static homogeneous electric field to the excitation and detection region. The influence of this electric field on the signals observed in the excitation spectrum was studied with the laser polarization perpendicular and parallel to the field. Thus, the alignment of the cluster ensemble in helium droplets could be analyzed and interpreted as described in chap. 3.3.

### 5.4.1 Bare Phthalocyanine

Bare Pc in helium droplets was used to check the experiment for systematic errors appearing for a molecule, which should not be influenced by the Stark field. The structure of bare free-base Pc exhibits an inversion center (cf. fig. 5.1). Therefore, the molecule does not possess a permanent dipole moment and its orientation should be independent of the application of an electric field. Fig. 5.7 shows the fluorescence excitation signal of bare Pc in helium droplets at 15088.9 cm$^{-1}$ as a function of the Stark field strength.

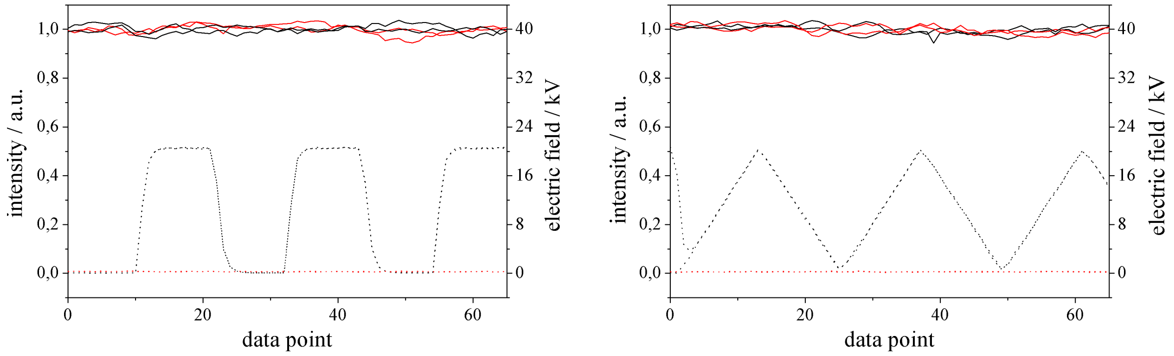

**Fig. 5.7:** Influence of an external homogeneous field on bare Pc in helium droplets. The fluorescence excitation signal was recorded at 15088.9 cm$^{-1}$ for a scan with the field switching quickly between 0 V and 20 kV (left) or increasing and decreasing slowly between the two values (right). The signal intensity (solid lines) is given on the left axis and compared for scans with (black) and without (red) application of the electric field. The field strength (dotted lines) is given on the right axis.

The solid lines represent the signal intensity, which is given on the left vertical axis, while the dotted lines represent the field strength, which is given on the right vertical axis. The black spectra refer to measurements with varying field strength, while the red spectra were taken without the application of a Stark field. For the spectra in the left panel the electric field was switched between 0 V and 20 kV. The spectra in the right panel were recorded while varying slowly between these two voltage intensities.

As expected for bare free-base Pc the fluorescence excitation signal at 15088.9 $cm^{-1}$ shows no reaction to the applied Stark field. This indicates that systematic errors in the experimental method can be excluded for a molecule showing no reaction to an applied electric field. This is an obvious improvement to earlier measurements undertaken in our lab [Chr13]. However, the spectra are not identical, but vary slightly in signal intensity independent of the Stark field strength. These small fluctuations in the signal intensity are in the order of 5 % of the signal and reveal the limitations of the experimental accuracy. Therefore, a verifiable influence of the Stark field on the excitation spectra has to be well above 5 % of the absolute intensity of the corresponding signal.

### 5.4.2 Parallel Adjustment

In order to draw conclusions regarding the orientation of the transition dipole moment $\vec{\mu_t}$ in relation to the electric dipole moment $\vec{\mu_p}$ of a $Pc(H_2O)_k$ cluster, fluorescence excitation spectra with the laser polarization perpendicular to the electric field are compared to those with a parallel adjustment. At first, the parallel arrangement was implemented and the fluorescence signal was recorded for the main transitions of the electronic spectrum of $Pc(H_2O)_k$ clusters in helium droplets. The electronic origin of bare Pc in helium droplets was regarded as well serving as a complement to the measurements described in chap. 5.4.1. Instead of measuring the signal dependance on the field strength at a fixed frequency the transitions were recorded over a range of at least 0.6 $cm^{-1}$ in order to regard the full extent of the spectral lines. This procedure was repeated several times under application of a 10 kV or 20 kV Stark field and under field free conditions.

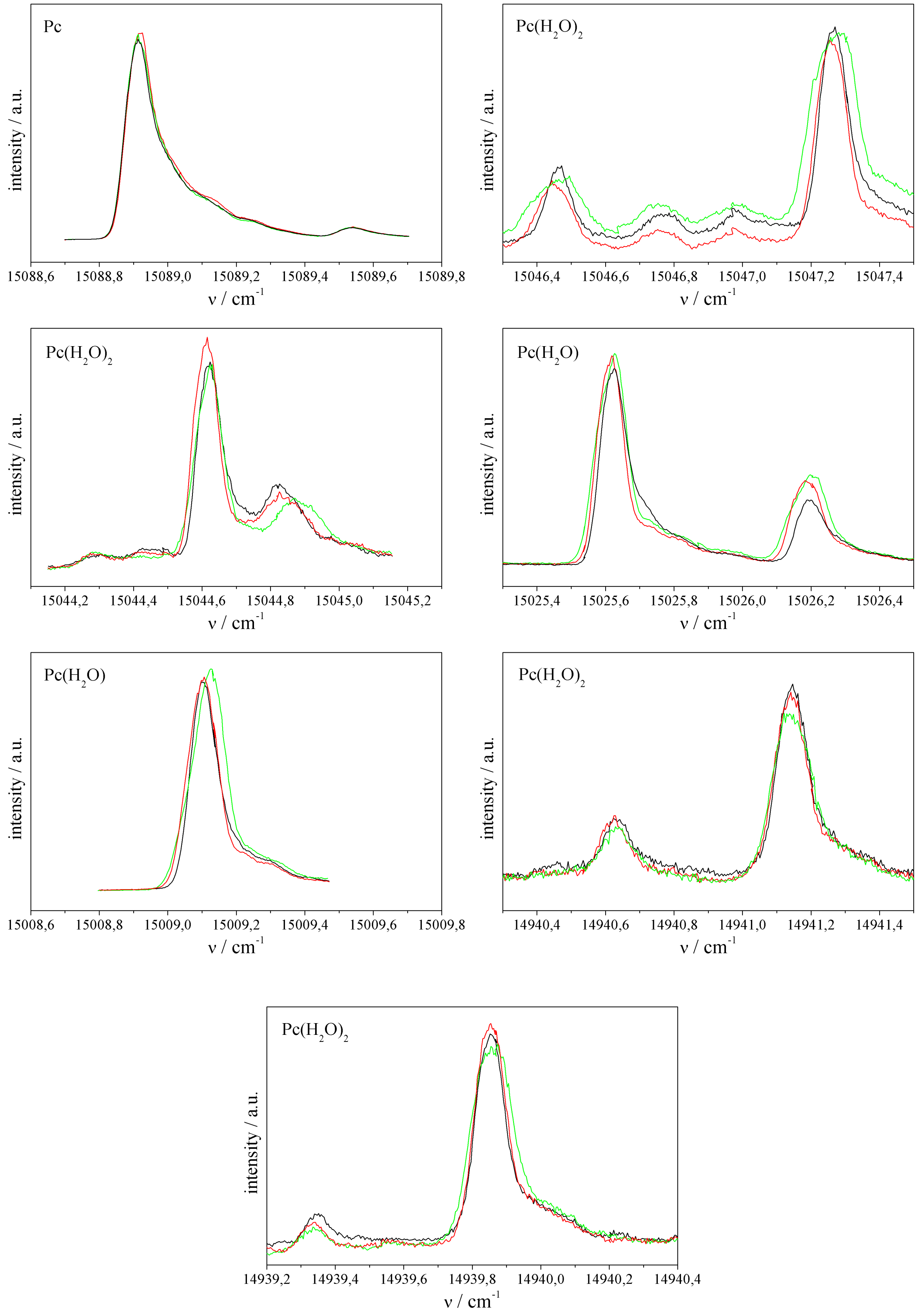

**Fig. 5.8:** Excitation spectra of Pc and $Pc(H_2O)_k$ clusters in helium droplets recorded field free (black) and under application of a Stark field with 10 kV (red) and 20 kV (green), respectively. The laser polarization is oriented parallel to the electric field and the spectra are measured with 250 datapoints per 1 $cm^{-1}$.

Fig. 5.8 shows the high resolution excitation spectra for the selected transitions of bare Pc and $Pc(H_2O)_k$ clusters in helium droplets. The spectra are listed according to decreasing transition energies and assigned to the cluster stoichiometries as indicated in tab. 5.1. They were recorded with 250 datapoints per 1 $cm^{-1}$ at different field strength of 0 V (black), 10 kV (red) and 20 kV (green). All panels extend over a frequency range of 1.2 $cm^{-1}$ and show the signals at optimized water doping corresponding to the respective cluster size.

As expected, the application of a homogeneous electric field does not influence the excitation spectrum of bare Pc in helium droplets. Small variations in the signal intensity are in the order of the accuracy of the experiment and they are not reproducible. However, a significant influence of the Stark field can be observed for the signal intensities of the $Pc(H_2O)$ and $Pc(H_2O)_2$ clusters' transitions. The change in signal intensity is most obvious at the edges of the lines, while being relatively weak at the lines' maxima. This influences the line shapes and positions of the peaks. With increasing field strength the lines become broader and shift slightly. These effects are reproducible and can be observed in all spectra of $Pc(H_2O)_k$ clusters in helium droplets of fig. 5.8 though to a varying extent.

A plot with the Stark spectra set into relation with the field free spectra illustrates these effects more explicitly. This can be seen in fig. 5.9. In contrast to the small fluctuations observed for bare Pc (cf. chap. 5.4.1) the influence of the electric field on the cluster signals becomes obvious. The graphs originate directly from the ones of fig. 5.8 and they are achieved by normalizing the spectra to the corresponding field free signal (black). The thick black line in each panel shows the field free spectrum normalized to the signal maximum. The normalization to the field free spectrum accentuates the line broadening effect at the edges of the transitions, which becomes more significant with higher field strength. A stronger percentage change can be observed at the red side of the peaks as compared to the blue side. This is most obvious for the intense lines of the $Pc(H_2O)$ clusters at 15009.1 $cm^{-1}$ and 15025.6 $cm^{-1}$.

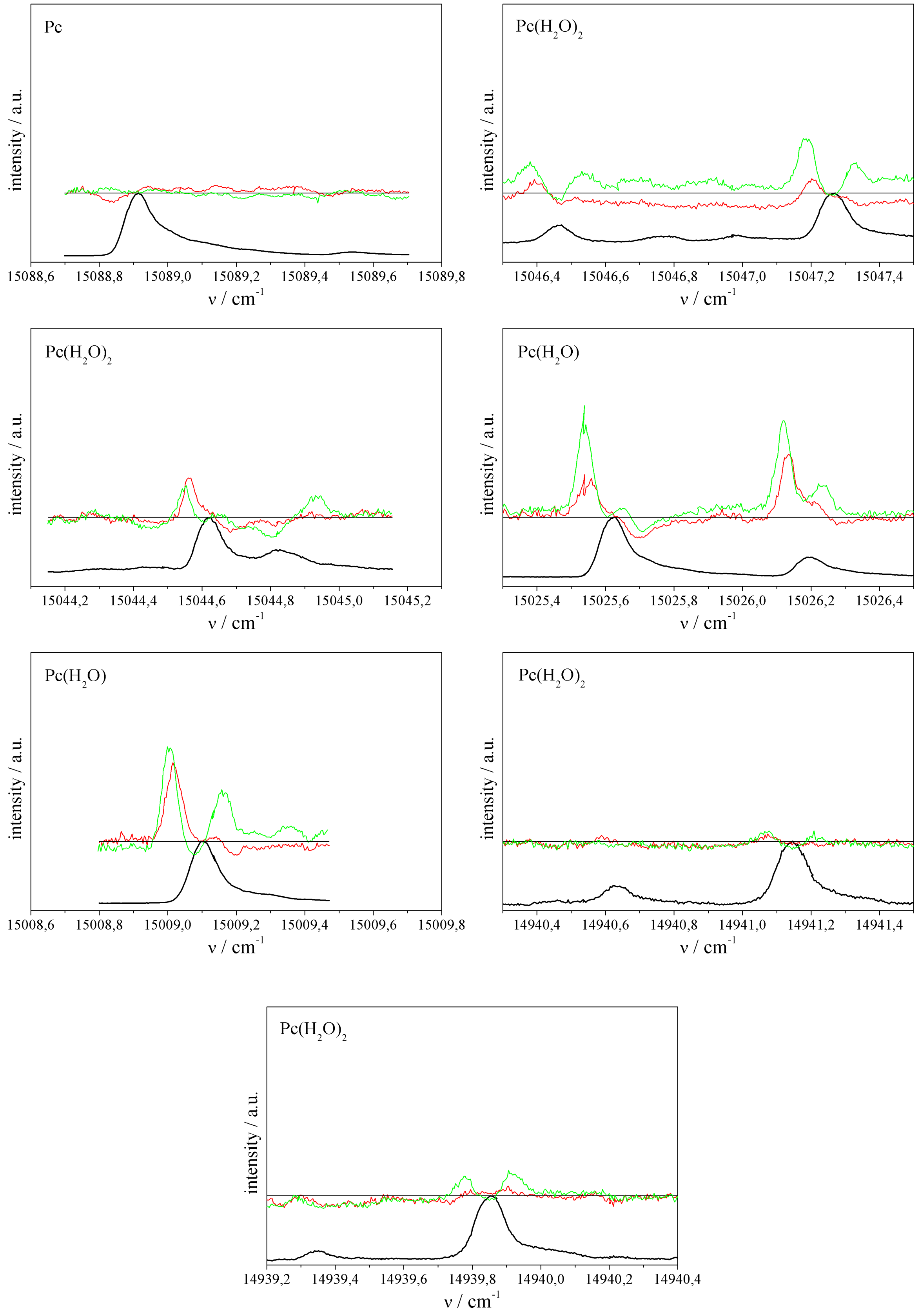

**Fig. 5.9:** Electronic spectra of Pc and Pc($H_2O$)$_k$ clusters in helium droplets recorded under application of a 0 V (black), 10 kV (red) and 20 kV (green) electric field oriented parallel to the laser polarization. The signals are normalized to the field free spectra. The thick black line in each panel shows the field free spectrum normalized to the signal maximum.

The influence of the electric field on the $Pc(H_2O)_k$ clusters also shows that these clusters exhibit a certain rigidity. This can be deduced from the observation that the Stark field influences the free rotations of the whole clusters instead of only orientating the water molecules. Apparently the van der Waals interaction between the water molecules and the Pc chromophores suffices to form stable structures in helium droplets.

However, the excitation signals do not exhibit the characteristic reaction expected for an aligned molecular ensemble, as depicted in fig. 3.4 in chap. 3.3. A clear increase or decrease of the signal intensity at the maximum of the regarded lines is not observed in the spectra. This indicates that the energy gainable by the orientation of the $Pc(H_2O)_k$ clusters in the electric field does not suffice to induce an alignment of the cluster ensemble and to transfer the particles into pendular states. The value of $(E_f \cdot \mu_p)$ seems to be in the same order of magnitude as the rotational energy $E_{rot}$ of the clusters. Thus, the electric field provokes merely a splitting of initially degenerated rotational states of the $Pc(H_2O)_k$ clusters for field strength $\leq$ 17 kV/cm. As the rotational fine structure of the clusters can, however, not be resolved with the experimental method applied in this research work, the Stark effect manifests in a broadening of the spectral lines of the electronic transitions.

### 5.4.3 Perpendicular Adjustment

Bare Pc, $Pc(H_2O)$ clusters and $Pc(H_2O)_2$ clusters in helium droplets were also investigated with the laser polarization orientated perpendicular to the Stark field. The same transitions as in the parallel arrangement were regarded but for the ones between 14939.2 $cm^{-1}$ and 14941.5 $cm^{-1}$. They were neglected as the electric field's influence on them could hardly be observed in the previous measurements due to their small signal intensity.

The fluorescence excitation spectra are shown in fig. 5.10. The plots are listed according to decreasing transition energies and show a frequency range of 1.2 $cm^{-1}$. The spectra were recorded under the same conditions as the ones with a parallel adjustment of the laser polarization and the electric field so as to regard again the full spectral extend of the signals at 0 V (black), 10 kV (red) and 20 kV (green). To receive a high resolution the spectra were recorded with 250 datapoints per 1 cm$^{-1}$. The cluster signals are optimized for single water doping in the case of Pc($H_2O$) and double water doping in the case of Pc($H_2O$)$_2$.

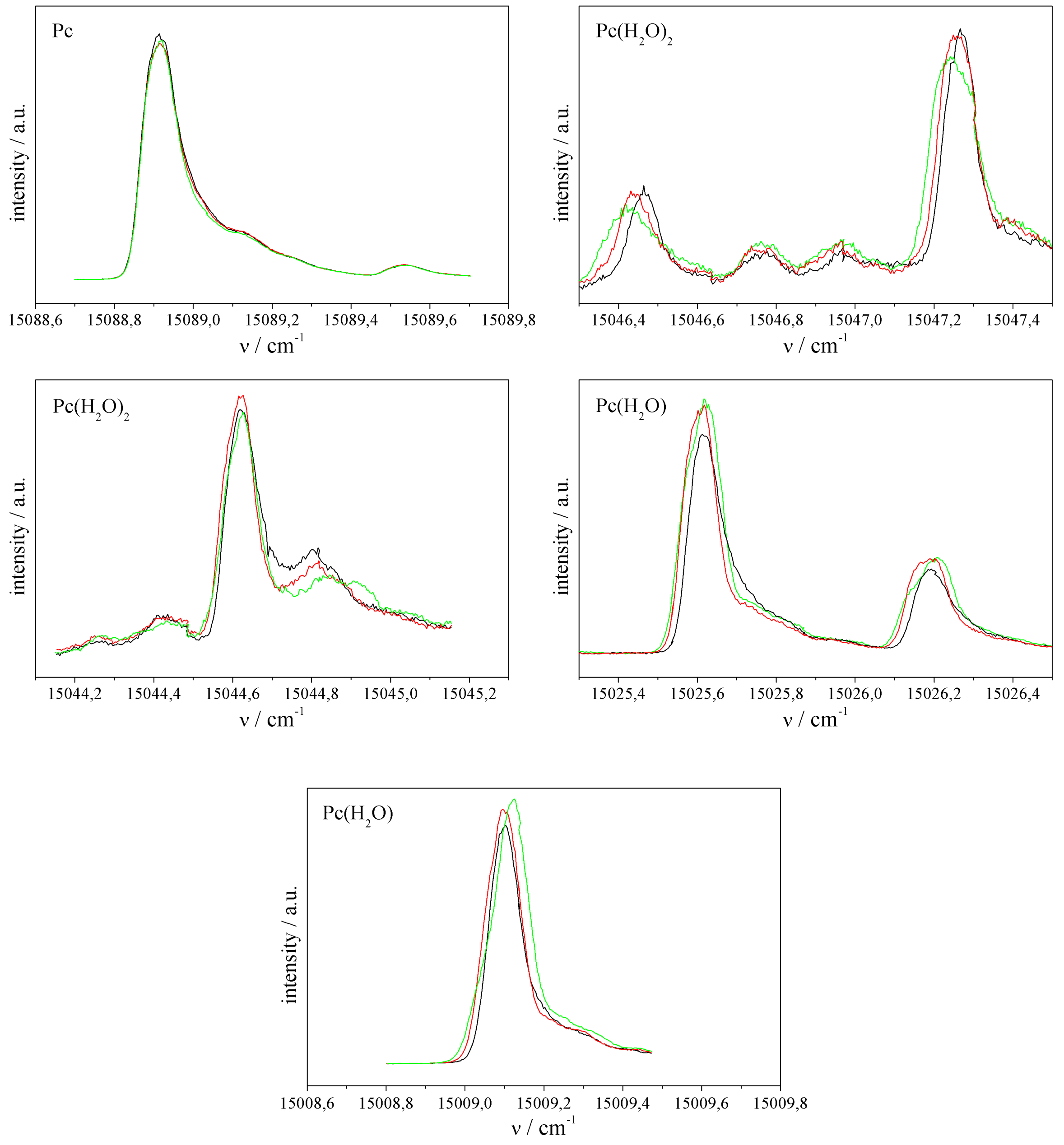

**Fig. 5.10:** Excitation spectra of Pc and Pc($H_2O$)$_k$ clusters in helium droplets recorded field free (black) and under application of a Stark field with 10 kV (red) and 20 kV (green), respectively. The laser polarization is oriented perpendicular to the electric field and the spectra are measured with 250 datapoints per 1 cm$^{-1}$.

The spectra show similar field effects as the ones observed before for the parallel adjustment of the laser polarization relative to the Stark field. A broadening of the lines can clearly be observed for the Pc($H_2O$) and Pc($H_2O$)$_2$ clusters' transitions and some transitions shift slightly. Both phenomena become more significant with a higher Stark field strength. The normalized plots illustrate this even more clearly. Fig. 5.11 shows the spectra taken under application of an electric field (red, green) normalized to the field free spectrum. Additionally the field free spectrum normalized to its maximum is given in each panel as a thick black line. The normalization to the field free spectrum shows that the percentage change in signal intensity is stronger at the edges of the transitions. The graphs confirm the similarity to the spectra taken with a parallel adjustment of laser polarization and electric field. This analogy of the electric field's influence on the excitation signals for the two adjustments of the laser polarization substantiates the conclusions reached in chap. 5.4.2. For a field strength $\leq$ 17 kV/cm the Pc($H_2O$)$_k$ clusters do not reach pendular states. Otherwise a differences in the signals' intensities depending on the orientation of the laser polarization relative to the direction of the electric field would be observed, as explained in detail in chap. 3.3.

As Pc does not possess a permanent dipole moment, the potential energy gain for the orientation of a Pc($H_2O$) cluster in a DC field can be estimated even if the exact configuration of the cluster is unknown. The electric dipole moment of Pc($H_2O$) is determined mainly by the water molecule and thus has an absolute value of about $\mu_p = 1.85$ D. The field strength in the present setup reaches a maximum value of 17 kV/cm for the application of a 20 kV voltage. This results in a potential energy of $E_{pot} = -1.05 \cdot 10^{-23}$ J. The line broadening in the Stark spectra, which can be explained by the splitting of rotational states of the Pc($H_2O$) clusters, indicates that this value does not considerably exceed the rotational energy of the clusters in helium droplets. In order to confirm these assumptions and draw conclusions on the configuration of the cluster, it was planed to simulate the Stark spectra for Pc($H_2O$). However, the orientation of the electric dipole moment could not be calculated satisfactorily for Pc($H_2O$) in superfluid helium droplets. Only the energetically favorable position of the water molecule over the center of the Pc structure could be determined, but not its orientation. To avoid this problem in further measurements one should choose a Pc species with a known dipole orientation as sample e.g. Chloroaluminiumphthalocyanine, which exhibits a dipole moment perpendicular to the Pc plane.

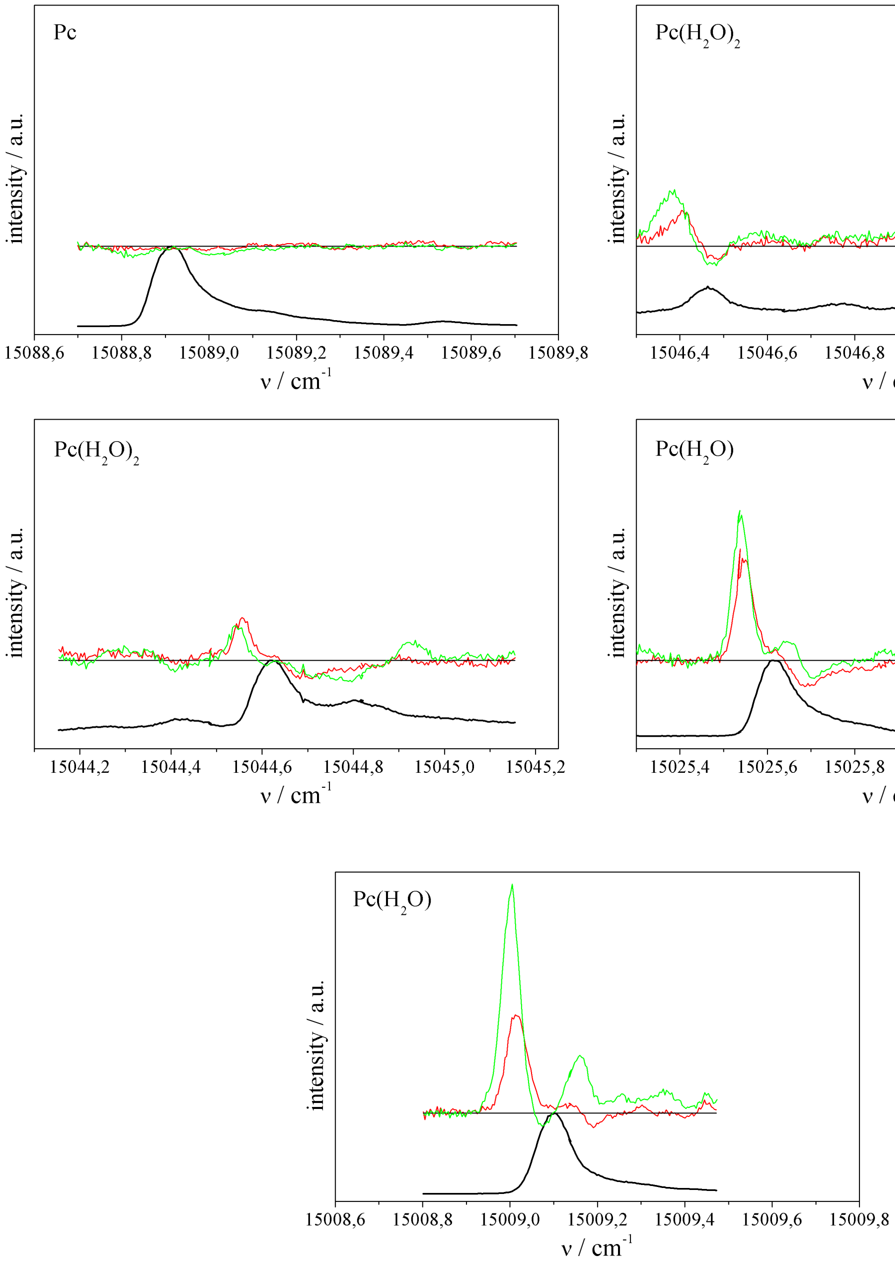

**Fig. 5.11:** Electronic spectra of bare Pc, Pc($H_2O$) and Pc($H_2O$)$_2$ in helium droplets recorded under application of a 0 V (black), 10 kV (red) and 20 kV (green) electric field oriented perpendicular to the laser polarization. The signals are normalized to the field free spectra. The thick black line in each panel shows the field free spectrum normalized to the signal maximum.

## 5.5 Summary

The fluorescence excitation spectrum of bare Pc, Pc($H_2O$) clusters and Pc($H_2O$)$_2$ clusters in superfluid helium droplets was investigated in the range from 15008 cm$^{-1}$ to 15095 cm$^{-1}$. All transitions observed in this region show sharp spectral lines with a line width of about 0.1 cm$^{-1}$. The signals could be assigned to the different clusters via the Poisson statistics of the pick-up procedure.

The main interest of this research was to gain insight on isomeric structures of the Pc($H_2O$)$_k$ clusters by using Stark spectroscopy. To this purpose the cluster transitions were recorded at high resolution over a range of at least 0.6 cm$^{-1}$ under the application of a 0 V, 10 kV and 20 kV Stark field, respectively. The spectra were recorded for the laser polarization adjusted parallel and perpendicular to the direction of the electric field. In both cases a reproducible broadening of the spectral lines could be observed for the transitions of the Pc($H_2O$) and Pc($H_2O$)$_2$ clusters. The spectra show no significant difference for the two adjustments of the laser polarization. The line broadening is interpreted as a result of the splitting and shifting of the clusters' rotational states, known as Stark effect. The measurements show that the clusters exhibit a certain rigidity and that their free rotation becomes hindered in an electric field. However, a field strength $\leq$ 17 kV/cm does not suffice to induce an alignment on a Pc($H_2O$)$_k$ ($k$ = 1,2) cluster ensemble in helium droplets. As the clusters do not reach pendular states conclusions regarding the orientation of the clusters' electric dipole moments and transition dipole moments can not be drawn directly from the spectra and no suggestions can be made regarding the different isomeric configurations of the clusters.

# 6 Anthracene Argon Clusters in Helium Droplets

In the literature van der Waals clusters of anthracene (An) have been considered in gas phase experiments [HHSS81, AEJ82, HYS$^+$85, HBSZ91, CL93, CK94, ORF95, MKH$^+$98, UBD$^+$98, PDM$^+$02] and in theoretical studies [GHH$^+$82, HYS$^+$85, ABPW91, SBHEJ91, SBJ91, UBD$^+$98, HEJ01, HJ03]. Their investigation in helium droplets is of special interest, since it provides information on how the interaction between An and the helium environment is influenced by adding additional molecules or atoms to the droplets. Thus, the doping variation offers insight on the microsolvation of An in helium droplets and the dopant's influence on the helium-chromophore interaction. In this context, the analysis of the spectral shift and the fine structure of the electronic transitions is of particular relevance especially in comparison with the spectra of bare An and also with other similar cluster experiments as for example of tetracene argon clusters in helium droplets [HLTV98, PVH01, KNT$^+$11] and pentacene argon clusters in helium droplets [HLTV98].

In this chapter the fluorescence excitation spectra and the dispersed emission spectra of An(Ar)$_k$ clusters in helium droplets are presented and discussed. Not only small clusters with $k < 5$ shall be regarded, but also the gradual transition to An fully embedded into Ar atoms is considered. The experiments include the electronic spectroscopy of An(Ar)$_k$ clusters formed in helium droplets after a post pick-up procedure as well as the measurements of the clusters formed in helium droplets after a prior pick-up procedure.

All experiments discussed in this chapter were performed with the pulsed helium droplet apparatus described in chap. 4.2. The droplets were generated with a stagnation pressure of 80 bar, nozzle temperatures between 21 K and 23 K and a repetition rate of 20 Hz or 50 Hz.

## 6.1 Introduction

Anthracene ($C_{14}H_{10}$) is a colorless, polycyclic aromatic compound. Fig. 6.1 shows its highly symmetric, planar structure, which belongs to the point group $D_{2h}$. The substance was discovered in 1832 and is primarily used for the production of anthroquinone, a dyestuff precursor. In addition, it is employed as an organic scintillator for detectors of high energy radiation [CH00].

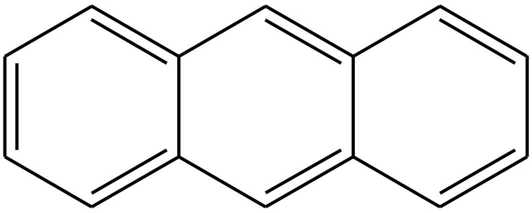

**Fig. 6.1:** Chemical structure of anthracene.

The physical and chemical properties of An make it well suited as a model compound for spectroscopic research. It shows a strong absorption in the near ultraviolet range and offers a high fluorescence quantum yield of $\Phi_f \approx 0.7$ [SAJ84]. Accordingly, An and many of its derivatives have been investigated intensively by various spectroscopic methods. Spectra measured in supersonic jet experiments [LFSZ84, SAJ84, KZ85, Ami87, PKSZ88, Ami88, AHJ88, NGH97, SRS$^+$04] and in matrix isolation experiments [CG82, LN90, FSHD93, WH94] have been reported in the literature. Various theoretical studies are known as well [Ohn79, DH81, ZZ88, ZSFH94, GNB94, ZHS95, JWKJ96, JK97, LBH$^+$98, ZSGL04, SSMS05]. Furthermore, spectra of An and some of its derivatives in superfluid helium droplets have been published in recent years [KRH05, PGDS10, PRV$^+$11, PS12].

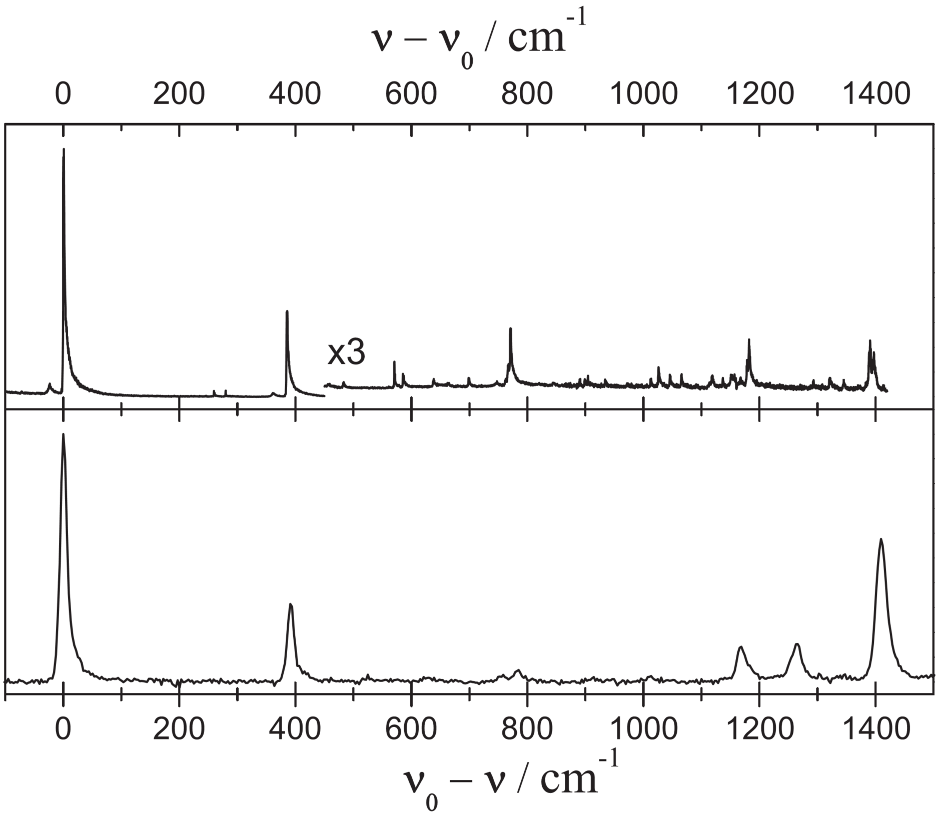

**Fig. 6.2:** Excitation spectrum (upper pannel) and dispersed emission spectrum (lower pannel) of An measured in a pulsed beam of helium droplets. The origin is at $\nu_0 = 27622$ cm$^{-1}$ for both spectra. The emission was recorded after excitation of the mode with an excess energy of $\nu = 385$ cm$^{-1}$ (from [PS12]).

The experimental results as well as the theoretical work identify An clearly as a rigid molecule. It exhibits a similar vibrational structure with sharp signals in the fluorescence excitation and dispersed emission spectra. Fig. 6.2 shows the fluorescence excitation spectrum (upper pannel) and the dispersed emission spectrum (lower pannel) of An measured in a pulsed beam of helium droplets [PS12]. Emission was recorded upon excitation of a vibronic transition exceeding the electronic origin by a vibrational quantum of 385 cm$^{-1}$. As expected for a rigid molecule the excitation spectrum is dominated by the electronic origin at $\nu_0 = 27622$ cm$^{-1}$ and intense low frequency modes are missing completely. This is in agreement with the spectra measured in the gas phase and in solid matrices.

The main difference to gas phase spectra is a helium induced fine structure, which can be observed for each transition of An in helium droplets. Among the polyacenes, which have been studied in helium droplets including benzene [ScD$^+$04, LBD08], naphthalene

[Lin99], anthracene [KRH05, PS12], tetracene [HLTV01, LS05], and pentacene [HLTV02, LS05], only the transitions of anthracene and tetracene appear as multiplets followed by a PW in the excitation spectrum. As this multiplet splitting does not appear in the gas phase it is seen as a spectral indication of the solvation of the molecule in helium droplets. The quartet fine structure of the electronic origin of An in helium droplets can be seen in the high resolution excitation spectra of fig. 6.3. The three spectra correspond to measurements with the laser intensities increasing by an order of magnitude from the blue to the red spectrum. The signals are normalized to the second of the two leading peaks and the lines are assigned as a quartet of ZPLs. Those specified as $\alpha$ and $\alpha'$ exhibit a common emission spectrum and so do the ones assigned as $\beta$ and $\beta'$ [PS12].

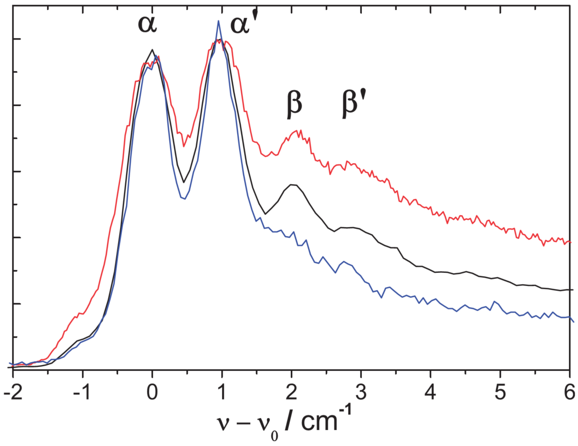

**Fig. 6.3:** High resolution excitation spectrum of the electronic origin of An in helium droplets normalized to the second of the two leading peaks. The graphs correspond to measurements with the laser intensities increasing by an order of magnitude from the blue to the red spectrum (from [PS12]).

## 6.2 Excitation Spectrum

From supersonic jet experiments on van der Waals clusters of An with Ar it is known that in the gas phase the $0_0^0$ transitions of small An(Ar)$_k$ clusters ($k \leq 4$) are shifted between about 30 cm$^{-1}$ and 200 cm$^{-1}$ to the red compared with the electronic origin of bare An [HHSS81, UBD$^+$98]. However, in helium droplet measurements the first signal belonging to an An(Ar)$_k$ cluster is recorded with a red shift of only about 10 cm$^{-1}$ to the $0_0^0$ transition of bare An, as can be seen in fig. 6.4.

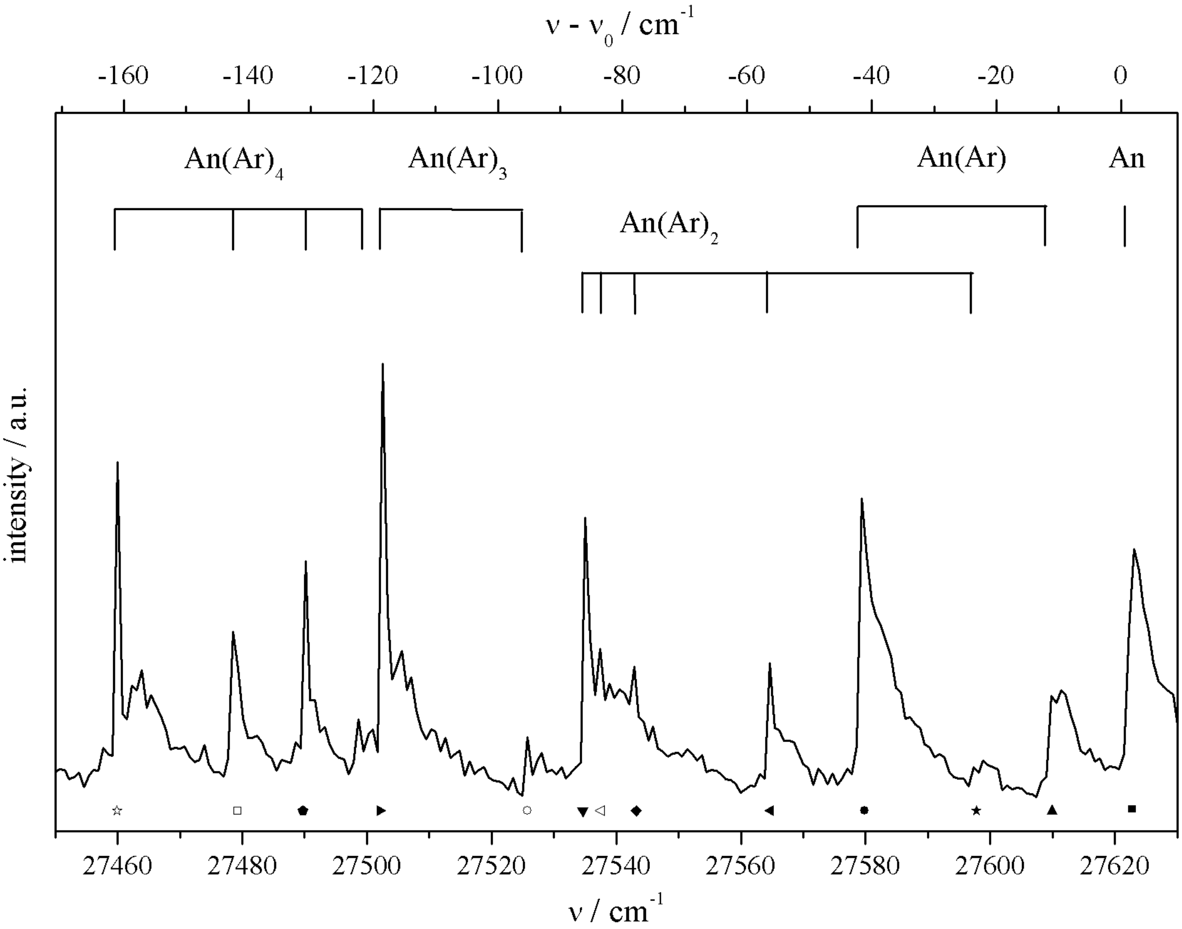

**Fig. 6.4:** Excitation spectrum of anthracene and anthracene-argon clusters measured in a pulsed beam of helium droplets. The particle density of argon in the pick-up cell was optimized for maximum intensities of the An(Ar)$_4$ transitions. The droplet doping was performed in a post pick-up process and the signals are assigned as indicated in fig. 6.8 and tab. 6.1.

The figure shows the fluorescence excitation spectrum of An(Ar)$_k$ clusters in helium droplets in a frequency range from 27450 cm$^{-1}$ to 27630 cm$^{-1}$. The helium droplets were doped in a post pick-up procedure, i.e. Ar atoms were added after the doping of the droplets with a single An molecule each. The particle density of Ar was adjusted in such a way in the pick-up cell as to result in the maximum intensity of the transitions belonging to An(Ar)$_4$ clusters. The signals are assigned as indicated in tab. 6.1. The signs below the lines added in fig. 6.4 mark those signals, which were considered for an assignment to a cluster size in chap. 6.3. They resemble the signs used in fig. 6.8. In the regarded frequency range the An(Ar)$_k$ clusters show sharp spectral lines, whose fine structure is, however, not resolved. It will be regarded in the following sections, which discuss the high resolution excitation spectra of the individual signals. The transitions selected for this detailed discussion and the cluster size analysis of chap. 6.3 are pointed out in fig. 6.4 by solid vertical lines. They were singled out, because they all show a similar saturation behavior. This distinguishes them from other transitions discernible in the excitation spectrum of $\mathrm{An(Ar)}_k$ clusters in helium droplets, which saturate only at significantly higher laser intensities. As discussed in chap. 3.1 this might be indicative for PWs. On the other hand, the different saturation behavior of the signals can also be explained with the excitation of $\mathrm{An(Ar)}_k$ clusters in helium droplets, which exhibit lower transition moments. Thus, a definite assignment of these signals is not possible with the applied experimental methods.

Fig. 6.5 also shows the excitation spectrum of An and $\mathrm{An(Ar)}_k$ clusters in helium droplets in a frequency range from 27450 $\mathrm{cm}^{-1}$ to 27630 $\mathrm{cm}^{-1}$.

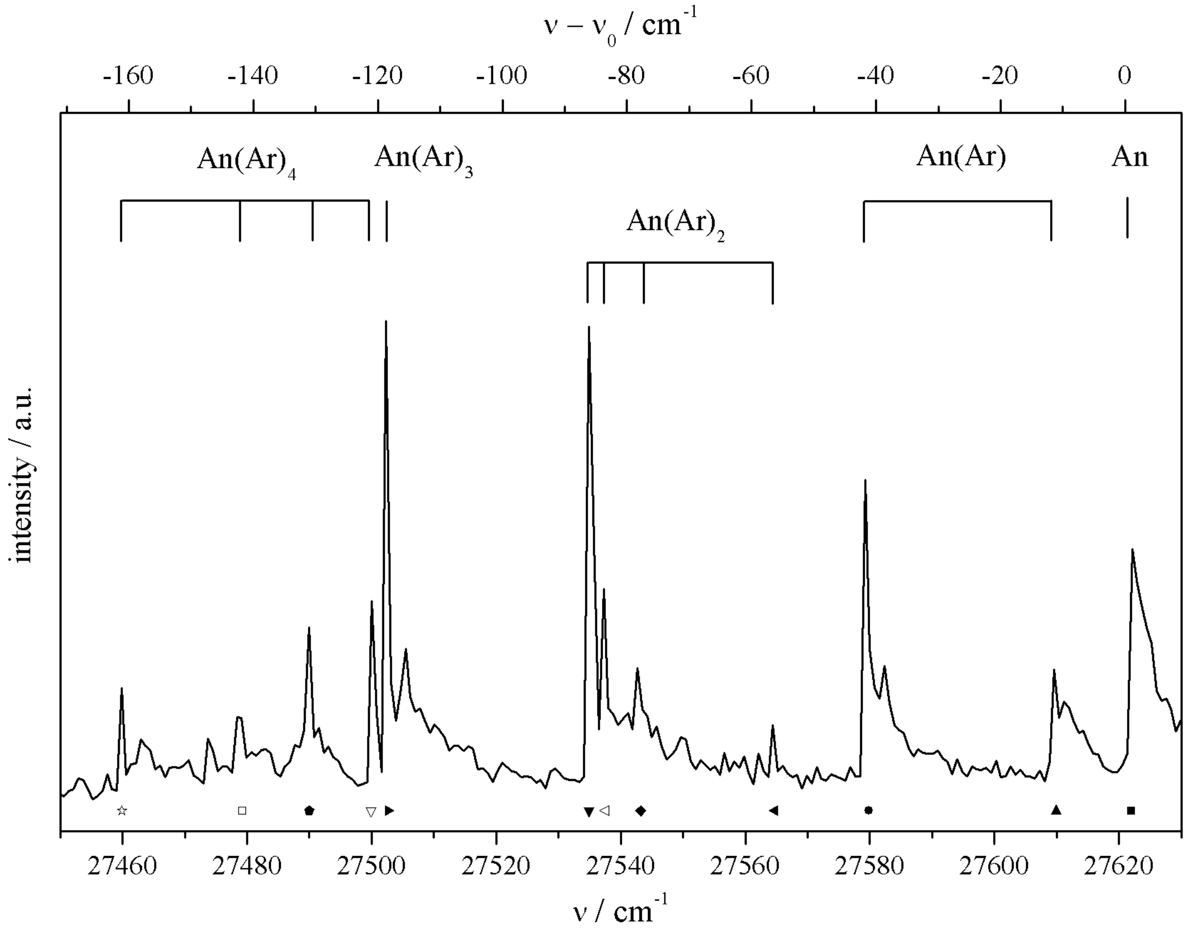

**Fig. 6.5:** Excitation spectrum of anthracene and anthracene-argon clusters measured in a pulsed beam of helium droplets. The argon pressure in the pick-up cell was optimized for maximum intensities of the $\mathrm{An(Ar)}_4$ transitions. The droplet doping was performed in a prior pick-up process and the signals are assigned as indicated in fig. 6.9 and tab. 6.1.

The assignment of the signals is as indicated in tab. 6.1. The marks below the spectral lines resemble the signs used for the data sets in fig. 6.9. The spectrum was recorded under similar conditions as the one of fig. 6.4, but the doping order of An and Ar was changed. Instead of a post pick-up process the droplets were doped in a prior pick-up process, i.e. the Ar atoms coagulate inside the helium droplets before An is picked up. This results in a significant difference in the intensity pattern of the transitions, since the alteration in the pick-up order changes the probabilities for the formation of distinct clusters. In a prior pick-up procedure isomers with all Ar atoms on the same side of the An plane are formed preferably, while the formation of isomers with Ar atoms on both sides of the An plane becomes less likely. Therefore, some transitions in the excitation spectrum of $\mathrm{An(Ar)}_k$ in helium droplets decrease considerably in signal intensity or miss completely, as the ones at 27526 $\mathrm{cm}^{-1}$ and 27597 $\mathrm{cm}^{-1}$. Other transitions show an increase in intensity, as the ones at 27499 $\mathrm{cm}^{-1}$, 27535 $\mathrm{cm}^{-1}$, 27539 $\mathrm{cm}^{-1}$ and 27543 $\mathrm{cm}^{-1}$.

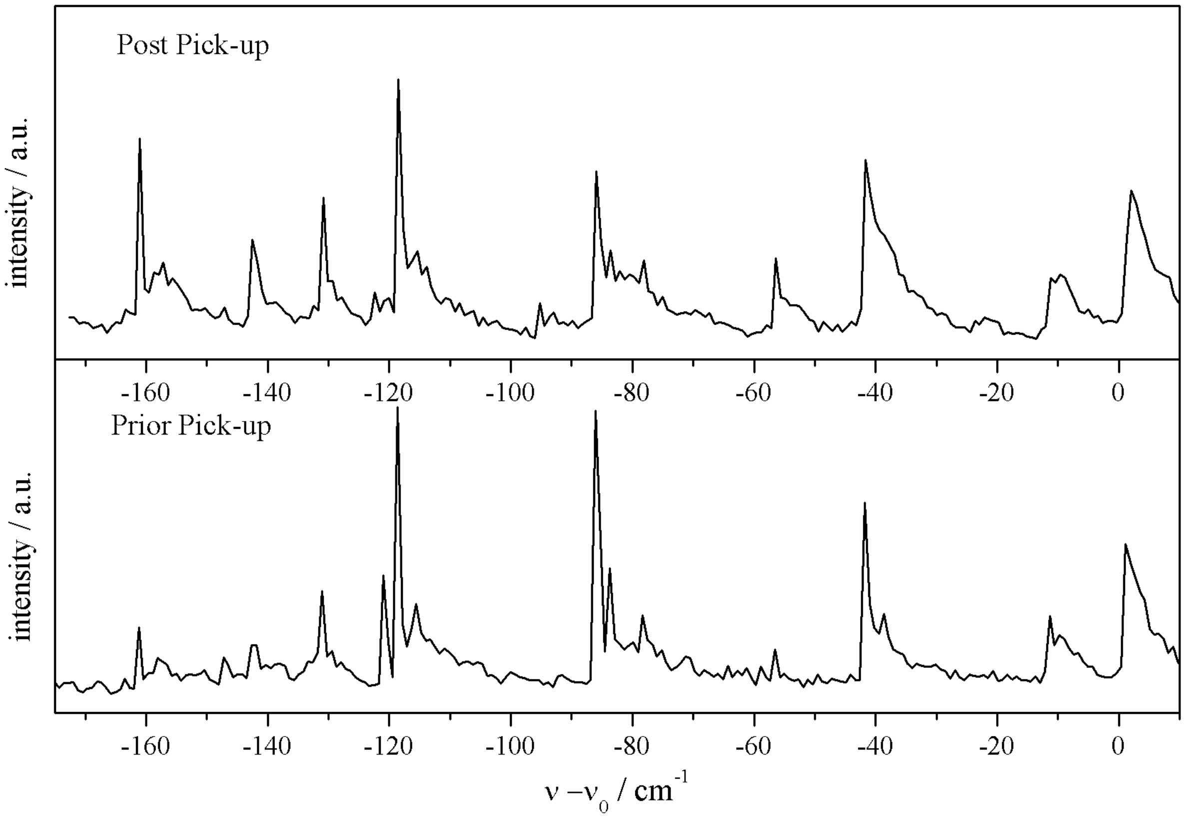

**Fig. 6.6:** Comparison of the excitation spectra of $\mathrm{An(Ar)}_k$ clusters in helium droplets for post and prior pick-up processes. The wavenumber is given relative to the electronic origin of bare An in helium droplets at $\nu_0 = 27622$ $\mathrm{cm}^{-1}$. The argon pressure in the pick-up cell was optimized for maximum intensities of the $\mathrm{An(Ar)}_4$ transitions.

These differences are most obvious when comparing the spectra directly as in fig. 6.6. The wavenumber is given relative to the electronic origin of bare An in helium droplets at $\nu_0 = 27622$ cm$^{-1}$. The crucial point, when comparing the two pick-up conditions by analyzing the excitation spectra, is to work with the same particle density of Ar in the pick-up cell for both measurements. It can be shown that this was the case for the spectra of fig. 6.6 by comparing the signal intensities of the transitions belonging to bare An and An(Ar) clusters. According to the explanations in chap. 2.3 the signal intensity of transitions belonging to bare An should decrease exponentially with increasing Ar pressure, while the signals of the An(Ar) clusters' transitions should follow the Poisson equation (equ. 2.4) with $k = 1$. Thus, the intensity ratio of these signals is a measure for the relative development of the Ar pressure in the pick-up cell. Moreover, the formation of both species is independent of the pick-up order and, therefore, an analog intensity ratio of their signals in the spectra of fig. 6.6 implies similar Ar doping pressures for both measurements.

For some intensive vibronic transitions a similar peak pattern as compared to the one observed with a red shift to the electronic origin of bare An was found when adding Ar to the droplet doping process. This can be seen in fig. 6.7 showing the excitation spectrum of bare An and An(Ar)$_k$ clusters in the region of the electronic origin and of the vibronic transitions with $\nu_{vib} = 385.5$ cm$^{-1}$ and $\nu_{vib} = 771.5$ cm$^{-1}$. The panels extend over a frequency range of 135 cm$^{-1}$ and the spectra are shifted so as to enable a comparison of the peak positions. The clusters were formed in a post pick-up procedure and the argon pressure in the pick-up cell was optimized for maximum intensities of the An(Ar)$_2$ transitions. From comparison of the three panels of fig. 6.7 it becomes apparent that the cluster signals, which can be resolved, show identical red shifts to the respective peaks belonging to bare An. The transitions also exhibit similar relative intensities. The differences in the intensity pattern are within the experimental accuracy considering that the S/N-ratio worsens considerably from the upper to the lower panel. Based on these observations the signals in the middle and lower panel of fig. 6.7 are assigned to vibronic transitions of the respective An(Ar)$_k$ cluster isomers with $\nu_{vib} = 385.5$ cm$^{-1}$ and

$\nu_{vib}$ = 771.5 cm$^{-1}$. The similarity of the vibronic transitions of the clusters and those of bare An in helium droplets shows that the addition of a small number of Ar atoms does not influence the vibrational frequencies of the excited state of the molecule.

According to [Pen10] the signal at 28389 cm$^{-1}$ marked with an asterisk also belongs to a vibronic transition of bare An in helium droplets. However, no transitions of An(Ar)$_k$ clusters are observed with the characteristic red shifts relative to this signal. This indicates that either this vibrational mode becomes hindered by the complexation of An with Ar atoms or that the assignment of the signal to bare An may be questioned.

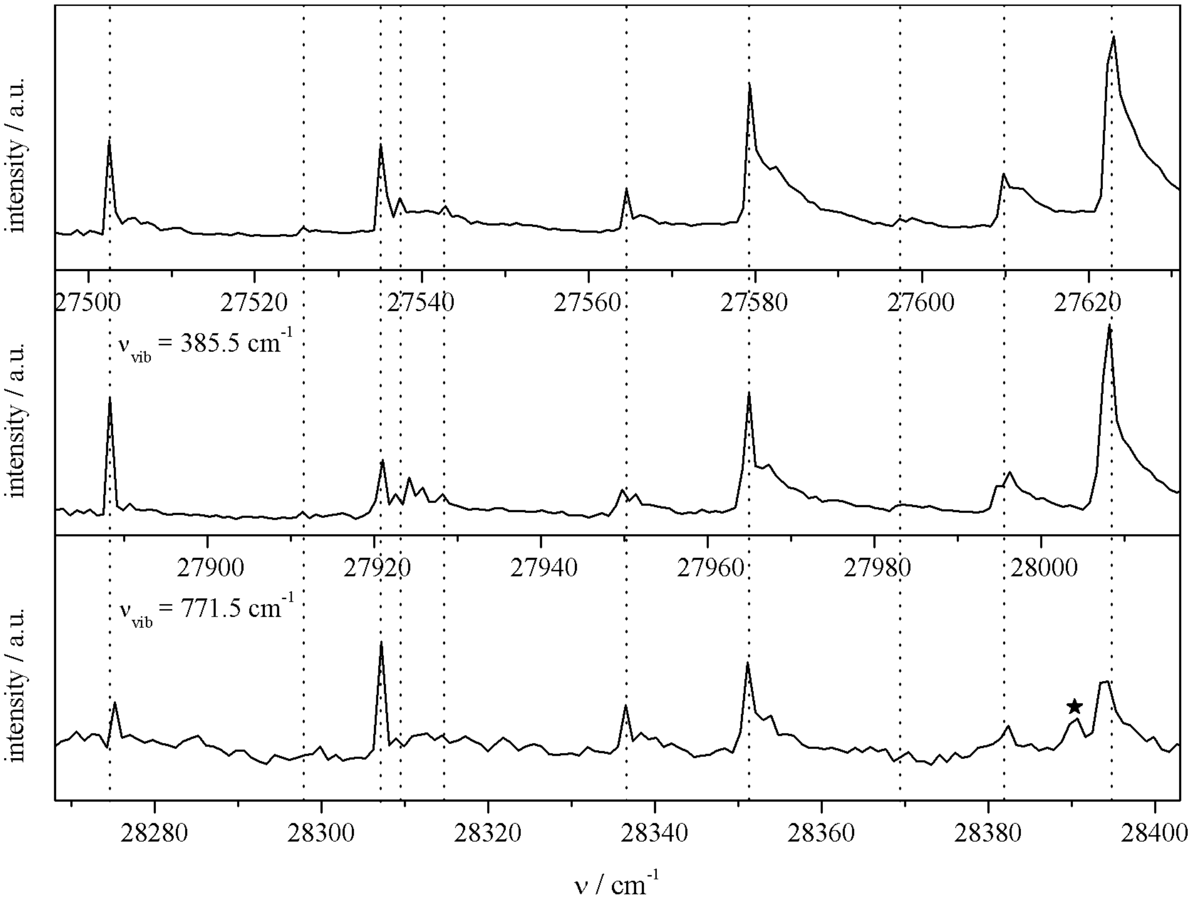

**Fig. 6.7:** Selected parts of the fluorescence excitation spectrum of bare An and An(Ar)$_k$ clusters in helium droplets. Each section extends over a frequency range of 135 cm$^{-1}$. The argon pressure in the pick-up cell was optimized for maximum intensities of the An(Ar)$_2$ transitions and the clusters were formed in a post pick-up process. The assignment of the signals marked with dotted lines and of the signal marked with an asterisk is discussed in the text.

## 6.3 Assignment of the Clusters

In order to determine the stoichiometry of the $\mathrm{An(Ar)}_k$ clusters, whose spectra are shown in fig. 6.4 and fig. 6.5, the fluorescence excitation for both pick-up sequences was measured for various particle densities in the Ar pick-up cell. The stagnation pressure of An in the oven was optimized for single particle doping and kept constant, while the particle density of Ar was successively increased in the gas pick-up cell from one measurement to the next. As described in chap. 2.3 the assignment of the cluster signals to particular cluster stoichiometries can then be derived using the correlation between the Ar density $n$ in the pick-up cell and the signal intensity of corresponding transitions $I_k$. Of course, this procedure is independent of the pick-up order and the assignment of the signals appearing in both spectra of fig. 6.6 should not differ.

For the $\mathrm{An(Ar)}_k$ clusters formed in a post pick-up procedure the intensities of the excitation signals are plotted as functions of the residual gas analyzer signal at 40 amu $I_{mass}$ in fig. 6.8. As explained in chap. 4.4 the analyzer's mass selective signal $I_{mass}$ is assumed to be proportional to the particle density $n$ in the pick-up unit and, thus, an appropriate measure for this application. The data analysis procedure of OriginPro 8 is used to fit Poisson distributions in the form of equ. 4.3 to the data sets. To reach the best agreement with the data points the parameters $k$, $I_k^0$ and $(\alpha\sigma L)$ are varied for each fitting procedure. From these Poisson distribution fittings the mean value of $(\alpha\sigma L)$ was determined as $1.9 \cdot 10^9$ $\mathrm{A}^{-1} \pm 0.4 \cdot 10^9$ $\mathrm{A}^{-1}$. For a second fitting of the Poisson distribution to the data sets $(\alpha\sigma L)$ was kept fixed at the mean value. The corresponding curves are shown as solid lines in fig. 6.8. The plots are arranged according to increasing $k$ demonstrating whether the regarded data set belongs to a transition of bare An $(k = 0)$, an An(Ar) cluster $(k = 1)$, an $\mathrm{An(Ar)}_2$ cluster $(k = 2)$, an $\mathrm{An(Ar)}_3$ cluster $(k = 3)$ or an $\mathrm{An(Ar)}_4$ cluster $(k = 4)$ . The positions of the graph's maxima are marked as dotted lines in fig. 6.8. Corresponding to $I_{mass}^{max} = k/(\alpha\sigma L)$ (cf. equ. 2.5 in chap. 2.3) they take the value of $5.3 \cdot 10^{-10}$ A for $k = 1$, $10.5 \cdot 10^{-10}$ A for $k = 2$, $15.8 \cdot 10^{-10}$ A for $k = 3$ and $21.1 \cdot 10^{-10}$ A for $k = 4$.

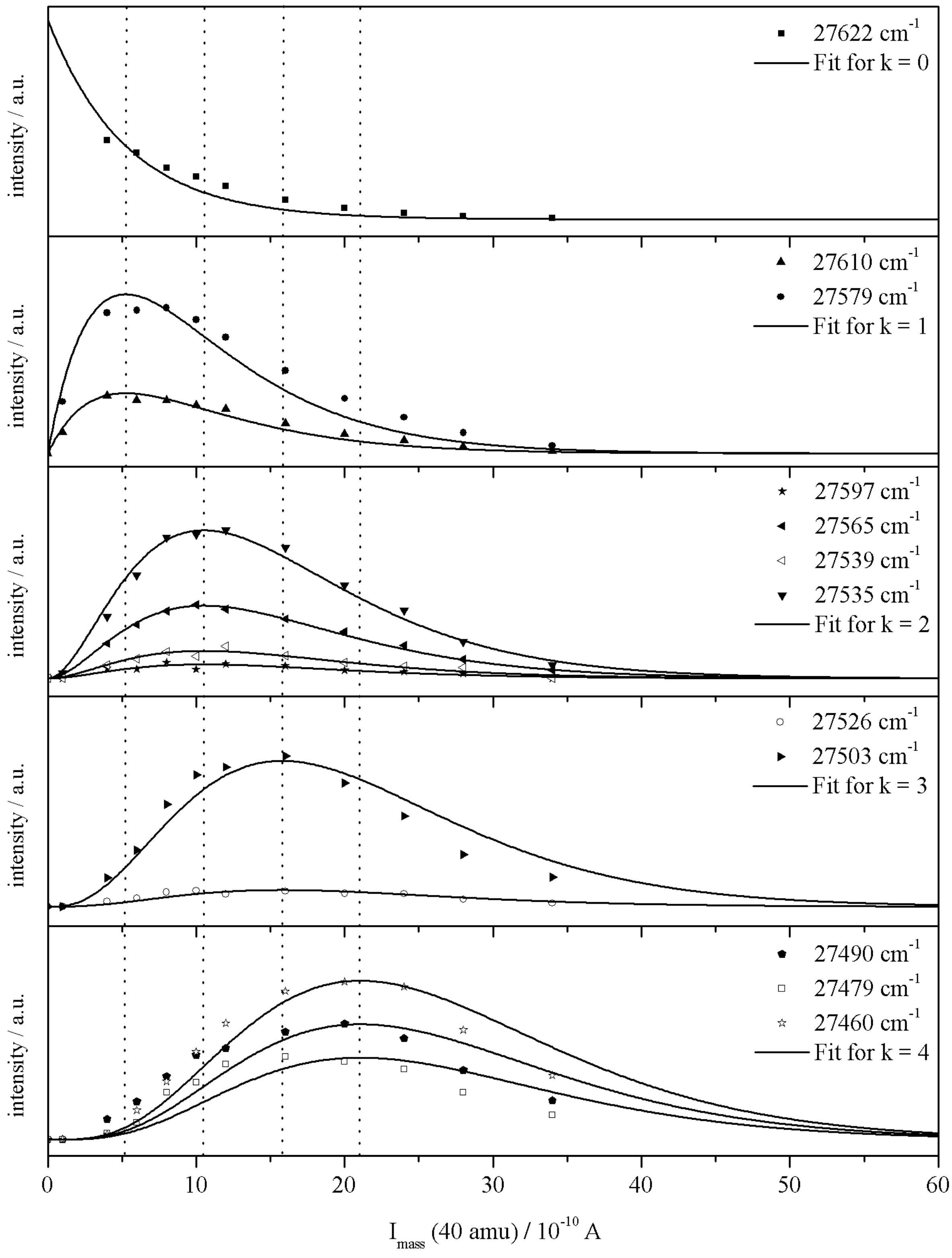

**Fig. 6.8:** Signal intensities in the fluorescence excitation spectrum of $An(Ar)_k$ clusters in helium droplets as functions of the signal $I_{mass}$ of the residual gas analyzer at 40 amu (mass of argon). The clusters are formed in a post pick-up procedure. The solid lines show Poisson distributions fitted to the data points according to equ. 4.3 with the denoted $k$. The dotted lines mark the positions of the fitted graphs' maxima.

For the smallest $\mathrm{An(Ar)}_k$ clusters in helium droplets with $k \leq 3$ the fitted graphs are in good agreement with the data sets. However, a discrepancy can be observed for the graphs belonging to $k = 4$, where the Poisson curves appear shifted to the right compared to the data points. For all signals regarded in the lowest panel of fig. 6.8 the deviation between the data points and the Poisson graphs is in the same order of magnitude, which may suggest a systematic error. The experimental approach and the assumptions underlying the data interpretation have to be questioned according to this observation. For example, to presume linearity between the Ar particle density $n$ in the gas pick-up cell and the mass selective power signal $I_{mass}$ of the residual gas analyzer may be an oversimplification of the experimental conditions (cf. chap. 4.4). An overlap of the regarded signals in the laser-induced fluorescence excitation spectrum may also have an effect on the analysis, as it influences the attribution of the signal intensities to the individual transitions. Furthermore, the experimental accuracy plays an important role when regarding rather weak signal intensities with a poor S/N-ratio. Unfortunately, due to the large number of parameters influencing the described assignment procedure the exact reason for the discrepancy between the data sets and the Poisson graphs for $k = 4$ cannot be defined with certainty. However, the value of $(\alpha\sigma L)$ for the fits of $k = 4$ differs only about 20 % from the mean value and therefore an assignment is still possible within the experimental accuracy.

The same approach as in the post pick-up case was repeated for the analysis of the signals belonging to $\mathrm{An(Ar)}_k$ clusters formed in helium droplets after a prior pick-up process. The signal intensities of the individual transitions are shown in fig. 6.9 as functions of the residual gas analyzer signal at 40 amu. From the first fitting procedure of Poisson distributions in the form of equ. 4.3 to the data sets the mean value of the parameter $(\alpha\sigma L)$ was determined to be $1.1 \cdot 10^9\ \mathrm{A}^{-1} \pm 0.1 \cdot 10^9\ \mathrm{A}^{-1}$. With $(\alpha\sigma L)$ kept fixed at this value the second fitting of the Poisson distribution to the data points yielded the graphs shown as solid lines in fig. 6.9. They are in good accordance with the recorded data sets. The plots are arranged according to increasing $k$ illustrating the assignment of the fluorescence excitation signals to a distinct $\mathrm{An(Ar)}_k$ cluster stoichiometry.

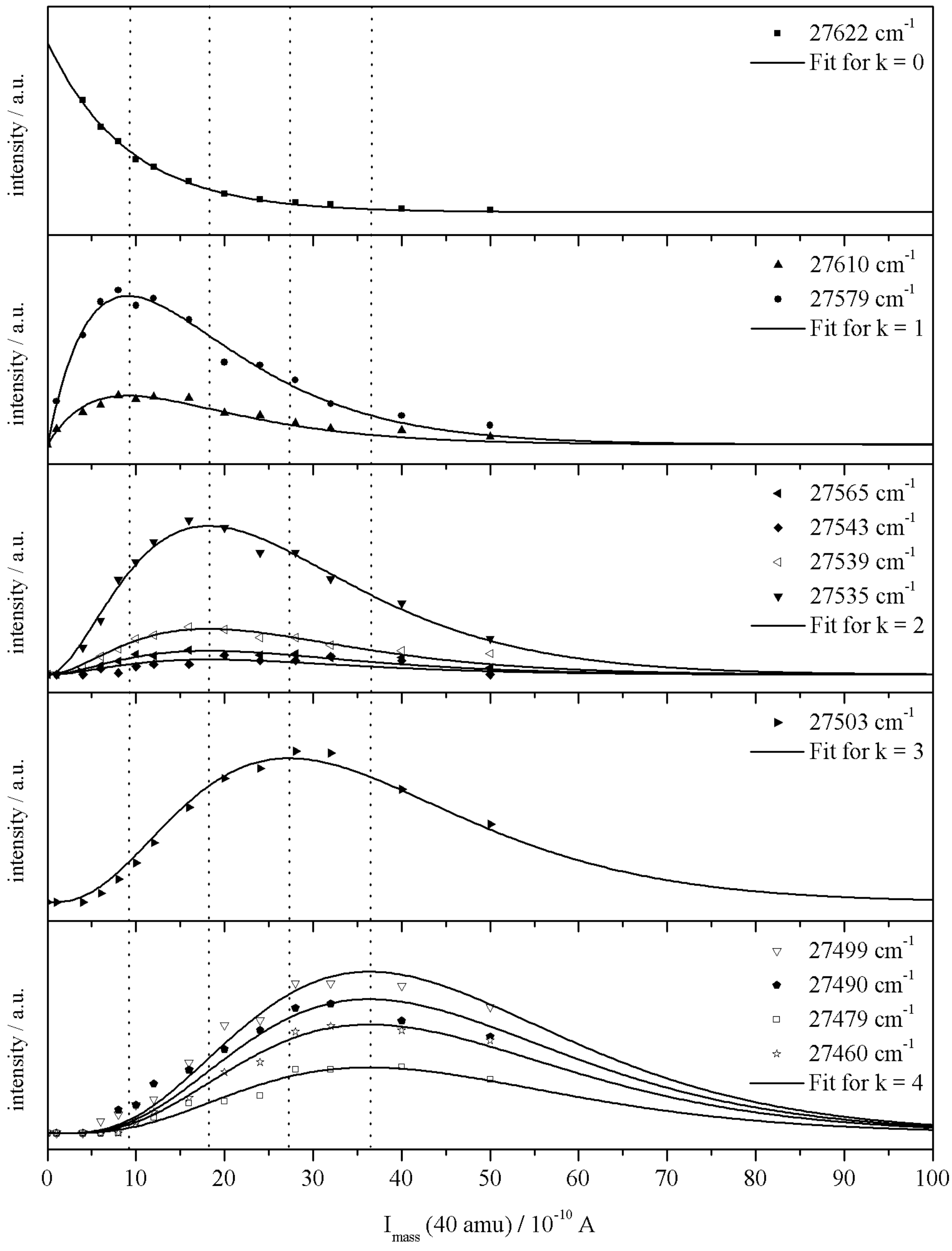

**Fig. 6.9:** Signal intensities in the fluorescence excitation spectrum of An(Ar)$_k$ clusters in helium droplets as functions of the signal $I_{mass}$ of the residual gas analyzer at 40 amu (mass of argon). The clusters are formed in a prior pick-up procedure. The solid lines show Poisson distributions fitted to the data points according to equ. 4.3 with the denoted $k$. The dotted lines mark the positions of the fitted graphs' maxima.

The maxima of the Poisson curves, which are marked as dotted lines in fig. 6.9, are at $9.1 \cdot 10^{-10}$ A for $k = 1$, at $18.2 \cdot 10^{-10}$ A for $k = 2$, at $27.3 \cdot 10^{-10}$ A for $k = 3$ and at $36.4 \cdot 10^{-10}$ A for $k = 4$. In the case of prior pick-up measurements of $\mathrm{An(Ar)}_k$ clusters in helium droplets a small discrepancy between the data sets and the Poisson graphs can again be observed for the signals assigned to $k = 4$. As in the post pick-up case regarded in fig. 6.8 the Poisson curves appear shifted to the right compared to the data points and the optimized value for $(\alpha\sigma L)$ differs about 20 % from the mean value. The assumption of a systematic error as discussed above would explain the similarity of the situations for $k = 4$ in fig. 6.8 and fig. 6.9.

A further observation when comparing the plots of fig. 6.8 and fig. 6.9 is that the fitting procedure leads to the same assignment of the signals for both pick-up orders. The difference between the mean value of the parameter $(\alpha\sigma L)$ results from the change in the experimental setup by repositioning the gas pick-up cell when changing between post and prior pick-up. This repositioning causes a change of the parameter $\alpha$, which regards the relation between the Ar particle density $n$ in the gas pick-up cell and the residual gas analyzer's power signal $I_{mass}$. The droplets' cross section $\sigma$ and the length of the droplets' flight path through the pick-up cell $L$ are not affected by the change in the pick-up order.

The signals of the laser-induced fluorescence excitation spectra of $\mathrm{An(Ar)}_k$ clusters in helium droplets are listed in tab. 6.1. They are arranged according to their assignment to certain cluster stoichiometries. The frequency shift $\nu - \nu_0$ is given compared to the electronic origin of bare An in helium droplets at $\nu_0 = 27622$ cm$^{-1}$. The signal intensity of the transitions is regarded for clusters formed in a post pick-up process and clusters formed in a prior pick-up process. It is given as a relative value in relation to the total intensity of all signals belonging to the same $k$ number, i.e. to clusters with the same stoichiometry. Thus, it shows clearly the influence of the pick-up order for $\mathrm{An(Ar)}_2$, $\mathrm{An(Ar)}_3$ and $\mathrm{An(Ar)}_4$ clusters.

In the following the electronic spectroscopy of $\mathrm{An(Ar)}_k$ clusters in helium droplets is discussed in detail, each chapter regarding all clusters with the same stoichiometry.

**Tab. 6.1:** Assignment of the signals in the excitation spectra of An and An(Ar)$_k$ clusters in helium droplets (fig. 6.4 and fig. 6.5). $\nu - \nu_0$ denotes the frequency shift compared to the $0_0^0$ transition of bare An in helium droplets at $\nu_0 = 27622$ cm$^{-1}$. The relative intensity of each line is given with respect to the total intensity of all signals belonging to the same $k$ number. In this context, a distinction is made between clusters formed in a post pick-up process (post) and clusters formed in a prior pick-up process (prior).

| k | $\nu$ / cm$^{-1}$ | $\nu - \nu_0$ / cm$^{-1}$ | rel. int. (post) | rel. int. (prior) |
|---|---|---|---|---|
| 0 | 27622 | 0 | 1 | 1 |
| 1 | 27610 | -12 | 0.27 | 0.27 |
| 1 | 27579 | -43 | 0.73 | 0.73 |
| 2 | 27597 | -25 | 0.07 | 0 |
| 2 | 27565 | -57 | 0.24 | 0.10 |
| 2 | 27543 | -79 | 0.06 | 0.08 |
| 2 | 27539 | -83 | 0.14 | 0.19 |
| 2 | 27535 | -87 | 0.49 | 0.63 |
| 3 | 27526 | -96 | 0.13 | 0 |
| 3 | 27503 | -119 | 0.87 | 1 |
| 4 | 27499 | -123 | 0.08 | 0.35 |
| 4 | 27490 | -132 | 0.30 | 0.28 |
| 4 | 27479 | -143 | 0.21 | 0.14 |
| 4 | 27460 | -162 | 0.41 | 0.23 |

## 6.4 Anthracene-Ar$_1$

This section discusses the laser-induced fluorescence excitation and the dispersed emission spectroscopy of An(Ar) clusters in helium droplets. The excitation spectra were measured with 13 datapoints per 1 cm$^{-1}$. The emission was dispersed with the 1200 lines/mm grating of the spectrograph leading to a distance between two pixel columns of about 6.5 cm$^{-1}$ at the blue and 5.4 cm$^{-1}$ at the red end of the emission spectra. As only clusters consisting of one An molecule and one Ar atom are regarded, the particle density in both pick-up cells was optimized for single particle doping for all spectra shown in this section.

### 6.4.1 Fluorescence Excitation

Two signals in the fluorescence excitation spectrum of An(Ar)$_k$ clusters in helium droplets could be assigned to clusters consisting of one An molecule and one Ar atom. They are shifted 12 cm$^{-1}$ and 43 cm$^{-1}$ to the red of the electronic origin of bare An in helium droplets at $\nu_0 = 27622$ cm$^{-1}$. As both transitions show high signal intensities the Poisson distribution fitting to the corresponding data sets could be performed with a good accuracy. The resultant graphs are in good accordance with the data points as can be seen in fig. 6.8 and fig. 6.9. The signal at $\nu - \nu_0$ = -43 cm$^{-1}$ exhibits one of the most intense lines in the excitation spectrum of small An(Ar)$_k$ clusters ($k \leq 4$). Relating to this value the signal intensity of the transition shifted $\nu - \nu_0$ = -12 cm$^{-1}$ reaches about 37 %. This ratio of the signal intensities is independent of the pick-up order.

Fig. 6.10 shows the high resolution excitation spectra of the two transitions recorded with different laser intensities. The wavenumber is given relative to the electronic origin of bare An in helium droplets. In (a) the spectra are normalized to the second of the two leading peaks, in (b) the spectra are normalized to the most intense line of the signal. The laser intensities increase by an order of magnitude from the green to the black spectra.

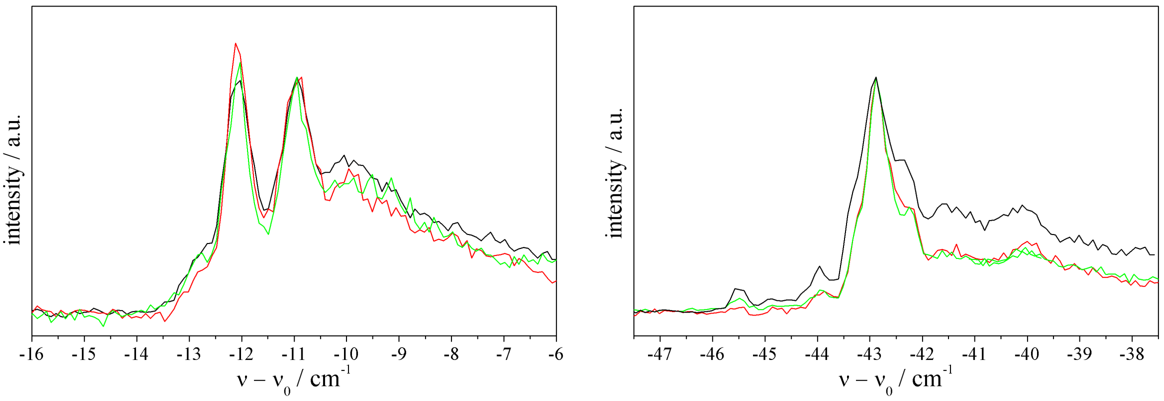

(a) The spectra are normalized to the second of the two leading peaks.

(b) The spectra are normalized to the most intense peak.

**Fig. 6.10:** Fluorescence excitation spectra of An(Ar) clusters in helium droplets recorded with 13 datapoints per 1 cm$^{-1}$. The wavenumber is given relative to $\nu_0 = 27622$ cm$^{-1}$. The graphs correspond to measurements with the laser intensity increasing by an order of magnitude from the green to the black spectrum.

The signal with a red shift of only 12 cm$^{-1}$ stands out in particular, as no intense signal with such a small shift to the $0_0^0$ transition of bare An could be recorded in gas phase measurements of small An(Ar)$_k$ clusters [HHSS81, UBD$^+$98]. The appearance of this additional intense transition can be the consequence of the influence of the helium environment enabling the formation of an An(Ar) isotopomer, which does not occur in the gas phase. Fig. 6.10 (a) shows that the signal in helium droplets exhibits a multiplet fine structure. The two intense leading peaks lie 1 cm$^{-1}$ apart and show a similar saturation behavior. At higher laser intensities an additional peak appears, which is shifted 2 cm$^{-1}$ to the blue of the first peak. This fine structure and saturation behavior resembles the observations made in measurements of the $0_0^0$ transition of bare An in helium droplets [PS12]. It could also be observed for the vibronic transition of bare An and An(Ar) in helium droplets at $\nu_{vib} = 385.5$ cm$^{-1}$. Fig. 6.11 shows the fluorescence excitation spectra of the electronic origin and the vibronic transition at $\nu_{vib} = 385.5$ cm$^{-1}$ for bare An and An(Ar) in helium droplets. All panels extend over a frequency range of 10 cm$^{-1}$ and they are arranged according to increasing transition energies. Due to the good accordance of these excitation spectra the assignment of the separate lines of the signals' fine structure as $\alpha$, $\alpha'$, $\beta$ and $\beta'$ used in [PS12] is also adopted for the transitions of this An(Ar) cluster in helium droplets. Unfortunately, the $\beta'$ peak could not be resolved in the An(Ar) cluster's helium droplet spectra and the $\beta$ peak could only be observed at the electronic origin. The reason for this is probably the lower signal intensity of the transitions compared with those of bare An in helium droplets. The fluorescence intensity of the cluster's transitions is more than an order of magnitude smaller than the intensity of the corresponding transitions of bare An. Therefore, a differentiation of the $\alpha$ and $\beta$ emission, as reported in [PS12], was impractical for the An(Ar) cluster. However, the good agreement of the fine structure in the excitation spectra and the similar saturation behavior of the peaks justify an identical assignment.

As this quartet fine structure does not appear in the gas phase spectra of An or An(Ar)$_k$ clusters it reflects the interaction between the dopant and the helium droplet. Therefore, an identical fine structure of An and An(Ar) implies that in this case the direct helium environment around An is hardly effected by adding one Ar atom. This suggests that the Ar atom is not directly attached to the An molecule, but stays on the helium solvation layer, which surrounds the An molecule inside the droplet. Based on this hypothesis, it is assumed that the excitation signal with a spectral shift of $\nu - \nu_0$ = -12 cm$^{-1}$ belongs to a separate electronic origin of an An(Ar) cluster in helium droplets. The assumed configuration also explains why a $0_0^0$ signal with such a small shift to the electronic origin of bare An could not be recorded in gas phase spectra [HHSS81, UBD$^+$98], as it includes the presence of a helium layer around the An molecule.

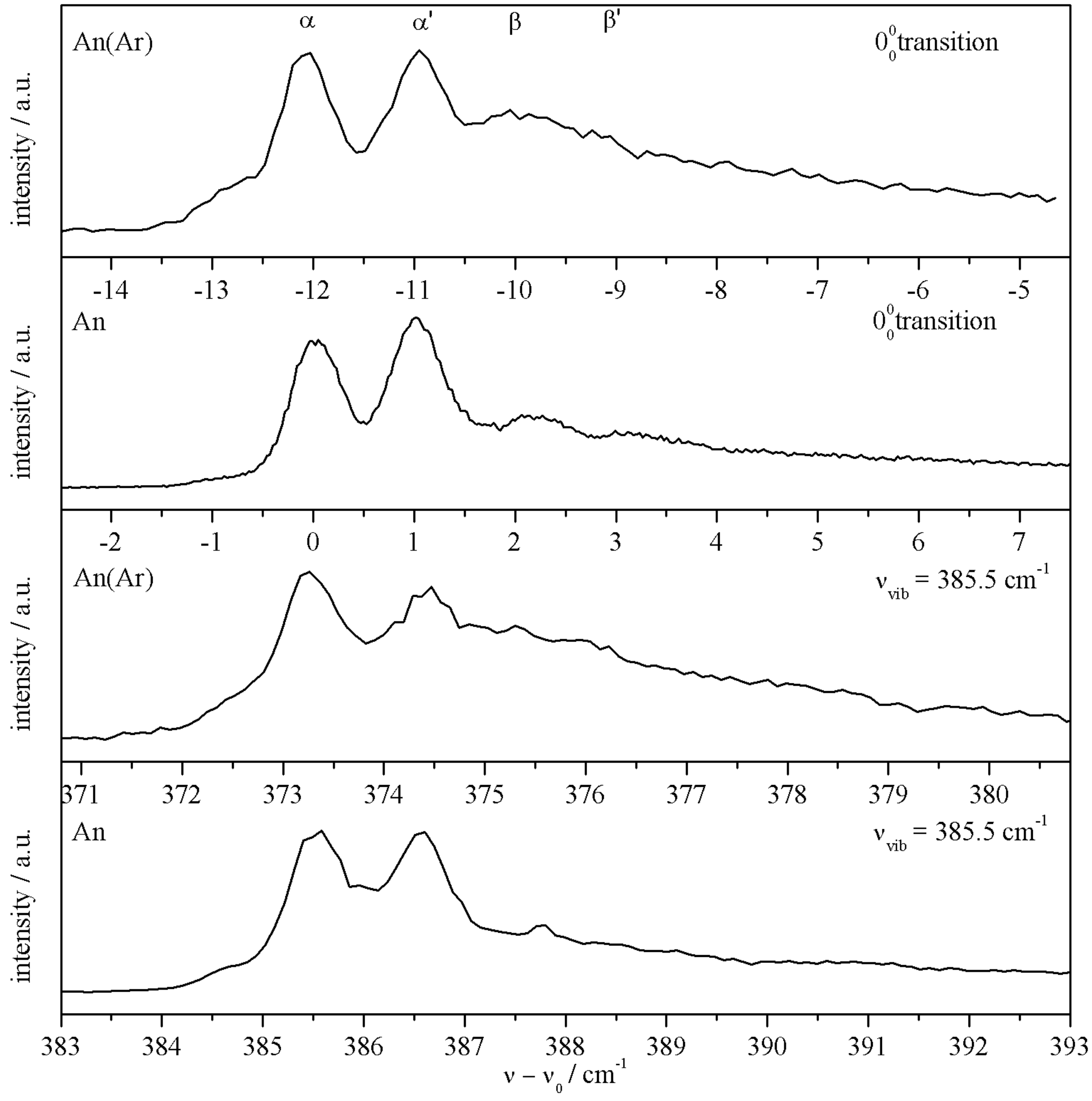

**Fig. 6.11:** High resolution fluorescence excitation spectra of the electronic origin and a vibronic transition at $\nu_{vib}$ = 385.5 cm$^{-1}$ of bare An and an An(Ar) cluster in helium droplets. The wavenumber is given relative to $\nu_0$ = 27622 cm$^{-1}$.

Now the second peak assigned to an An(Ar) cluster in helium droplets is regarded. It is shifted $\nu - \nu_0$ = -43 cm$^{-1}$ relative to the electronic origin of bare An in helium droplets and shows a totally different fine structure. This can be seen in the right panel (b) of fig. 6.10 and in the top panel of fig. 6.12. Around the main peak with a line width of about 0.3 cm$^{-1}$ several small peaks are located. They saturate only at higher laser power and are shifted 2.5 cm$^{-1}$ and 1.0 cm$^{-1}$ to the red and 0.6 cm$^{-1}$, 1.3 cm$^{-1}$ and 3.0 cm$^{-1}$ to the blue of the main peak. The vibronic transition of the cluster at $\nu_{vib}$ = 385.5 cm$^{-1}$ shows a very similar fine structure as can be seen in the lower panel of fig. 6.12. The gross disparity between this fine structure and the one observed for bare An in helium droplets indicates that in this case the interaction between the An molecule and its direct helium environment is considerably affected by the additional Ar atom. This leads to the assumption that the excitation signal with a red shift of $\nu - \nu_0$ = -43 cm$^{-1}$ belongs to a cluster, where the Ar atom is directly attached to the An molecule.

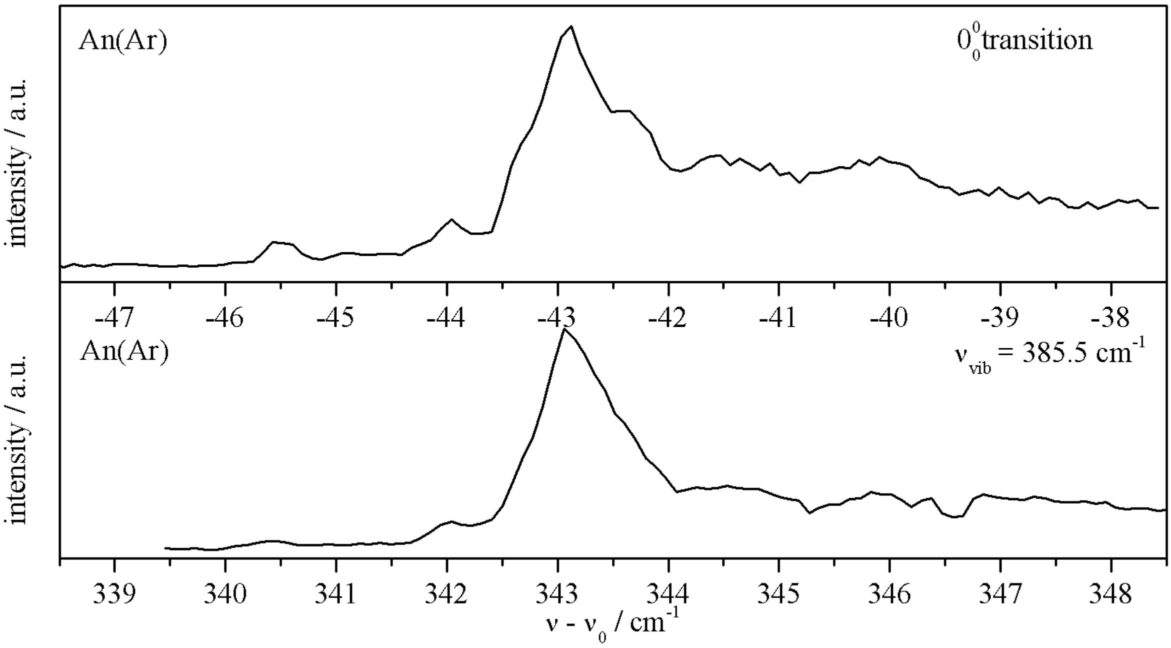

**Fig. 6.12:** High resolution fluorescence excitation spectra of the electronic origin and a vibronic transition at $\nu_{vib}$ = 385.5 cm$^{-1}$ of an An(Ar) cluster in helium droplets. The wavenumber is given relative to $\nu_0$ = 27622 cm$^{-1}$.

In gas phase spectra several excitation signals could be observed for a cluster stoichiometry with one An molecule and one Ar atom. Their shifts relative to the origin of bare An are given as +2 cm$^{-1}$, -14 cm$^{-1}$, -23 cm$^{-1}$, -40 cm$^{-1}$ and -45 cm$^{-1}$ in [UBD$^+$98] and as -43 $\mathrm{cm}^{-1}$ and -48 $\mathrm{cm}^{-1}$ in [HYS+85], respectively. However, in both publications the calculations of the An-Ar intermolecular potential energy yielded only one stable minimum energy configuration, with the Ar atom located above the central ring of the An. The optimized intermolecular distance is given as 3.44 Å in [UBD+98] and 3.43 Å in [HYS+85]. Fig. 6.13 shows the contour map of the An-Ar intermolecular potential energy surface calculated with Lennard-Jones type atom-atom potentials (C-Ar, H-Ar) [UBD+98]. The signal with a red shift of 40 $\mathrm{cm}^{-1}$ [UBD+98] or 43 $\mathrm{cm}^{-1}$ [HYS+85] to the $0_0^0$ transition of bare An was assigned to the electronic origin of this cluster. Hole-burning spectra showed that the low intensity bands shifted +2 $\mathrm{cm}^{-1}$, -14 $\mathrm{cm}^{-1}$ and -23 $\mathrm{cm}^{-1}$ belong to the the same species and can presumably be assigned to excitations of van der Waals modes in the $S_1$ state of this An(Ar) cluster [UBD+98]. According to [UBD+98] also the appearance of the signal at $\nu - \nu_0$ = -43 $\mathrm{cm}^{-1}$ can not be explained with a second minimum configuration, but arises from different dynamical properties, in particular the internal energy content, of the same cluster. This assumption of a hot band in the gas phase fluorescence excitation spectrum is based on the comparison of the experimental data with Monte-Carlo simulations of An(Ar) at different temperatures.

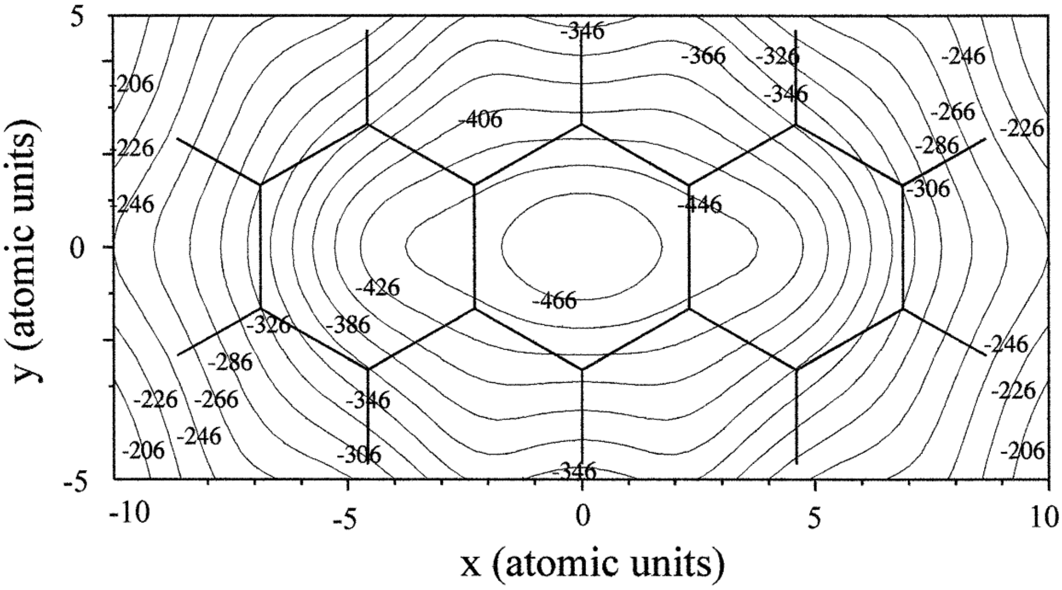

**Fig. 6.13:** Contour map of the An-Ar intermolecular potential energy surface from [UBD+98]. The distance of the Ar atom to the planar An molecule (z coordinate) was optimized and the minimum was found at -486 $\mathrm{cm}^{-1}$ (z = 3.44 Å). The contour lines indicate the potential energy in $\mathrm{cm}^{-1}$.

By comparison with these results, suggestions can be made for the structure of the An(Ar) cluster belonging to the signal at $\nu - \nu_0$ = -43 cm$^{-1}$ in the helium droplet spectrum. It can be assumed that the minimum configuration calculated for the free cluster in the gas phase is also formed in a helium droplet environment. Then the signal at $\nu - \nu_0$ = -43 cm$^{-1}$ would belong to the $0_0^0$ transition of a cluster with the Ar atom located about 3.44 Å above the central ring of the planar An molecule. One of the points indicating this assignment is the similar red shift in helium droplet and gas phase spectra of the cluster signal relative to the electronic origin of bare An. In addition, calculations revealed only one stable configuration, which corresponds to a one minimum potential surface for an An(Ar) cluster. At the same time, it is worth keeping in mind that the droplet environment might modify this potential energy surface due to the interaction between the helium and the An(Ar) cluster. Given this context, a definite assignment of the An(Ar) cluster configuration in helium droplets is not possible. However, it is not surprising that in contrast to the gas phase spectrum signals of 'hot' An(Ar) clusters are missing completely in helium droplet measurements due to the droplet temperature of only 0.37 K.

Thus, the two excitation signals at $\nu - \nu_0$ = -12 cm$^{-1}$ and $\nu - \nu_0$ = -43 cm$^{-1}$ in the helium droplet spectrum of An(Ar)$_k$ clusters discussed in the preceding paragraphs presumably belong to quite distinct AnAr clusters. The isomers are distinguished by the different red shifts and fine structures of their signals. This observation can be compared with the results of spectroscopic investigations on small tetracene-Ar clusters and pentacene-Ar clusters in helium droplets [HLTV98, PVH01]. In the excitation spectrum of tetracene clusters three signals are assigned to isomers with one Ar. One of them, which shows the largest red shift relative to the $0_0^0$ transition of bare tetracene, is expected to be the electronic origin of a cluster with the Ar atom located directly above one of the middle rings of the tetracene plane. This is the only tetracene-Ar signal in the helium droplet spectrum, which exhibits a counterpart in the gas phase. It does not show the characteristic splitting observed in the fine structure of bare tetracene in helium droplets. The other two peaks with a shift $\leq$ 20 cm$^{-1}$ to the red of the electronic origin of the bare molecule in helium droplets did not appear in the gas phase spectrum [BHEJL92]. These peaks show much smaller signal intensities and are seen as the $\alpha$ and $\beta$ line of a transition belonging to a second tetracene-Ar isomer. These observations are quite similar to the ones discussed for An(Ar) in helium droplets except that in the case of the An(Ar) signal at $\nu - \nu_0$ = -12 cm$^{-1}$ the fine structure is almost identical to the one of the free molecule's transitions in helium droplets. However, in the case of tetracene-Ar the gap between the observed $\alpha$ and $\beta$ line is increased compared with the splitting recorded for bare tetracene in helium droplets [PVH01]. This suggests that the addition of Ar has a stronger influence on the interaction between tetracene and its direct droplet environment than on the interaction of An with the surrounding helium. In the case of pentacene-Ar clusters transitions of two stable minimum configurations could be observed in the gas phase and in helium droplets [HLTV98]. Two additional signals in the excitation spectrum appear only in the droplet measurements. As in the case of An and tetracene these signals show lower intensities and a smaller red shift of $\leq$ 20 cm$^{-1}$ to the electronic origin of the bare molecule in helium droplets.

Apparently, similarities can be recognized regarding the formation of clusters consisting of a polycyclic aromatic molecule and one Ar atom in helium droplets. Apart from signals assigned to isomers with a stable minimum configuration calculated for the free clusters, additional transitions are observed in the excitation spectra in helium droplets. In the case of An, tetracene and pentacene these excitation signals are always less intensive than those, which also appear in the gas phase spectra. Moreover, they show red shifts $\leq$ 20 cm$^{-1}$ relative to the electronic origin of the bare molecule in all helium droplet spectra, while in the gas phase no intensive cluster transitions are observed with such a small shift. Due to the signals' fine structure it is assumed that the helium solvation shell, which surrounds molecules embedded in helium droplets, plays an important role in the formation of the corresponding cluster isomers.

### 6.4.2 Dispersed Emission

In order to prove the assumption of two electronic origins of An(Ar) isotopomers in helium droplets the clusters were also investigated with dispersed emission spectroscopy. Fig. 6.14 shows the dispersed emission spectrum recorded upon excitation at $\nu_{exc}$ = 27610 $cm^{-1}$. This corresponds to the excitation of the $\alpha$-line in the An(Ar) transition with a red shift of $\nu - \nu_0$ = -12 $cm^{-1}$ to the $0_0^0$ transition of bare An in the excitation spectrum in helium droplets.

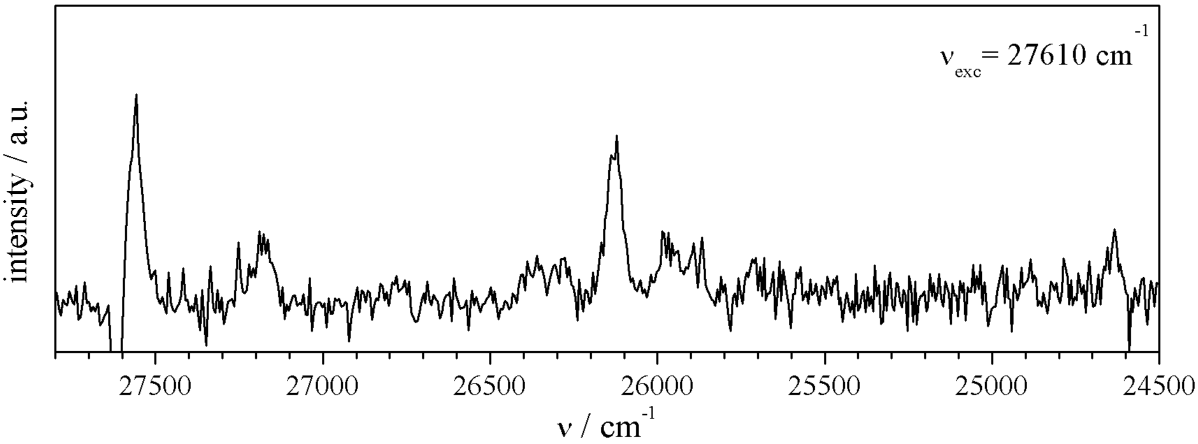

**Fig. 6.14:** Emission spectrum of An(Ar) in helium droplets recorded upon excitation at $\nu_{exc}$ = 27610 $cm^{-1}$. The electronic origin is identified at $\nu$ = 27603 $cm^{-1}$. Emission was dispersed with the 1200 lines/mm grating of the spectrograph. The distance between two pixel columns amounts to about 6.5 $cm^{-1}$ at the blue and 5.4 $cm^{-1}$ at the red end of the spectrum.

The electronic origin in this emission spectrum is identified at $\nu$ = 27603 $cm^{-1}$. However, its exact position is hard to determine due to the strong signal fluctuation in this frequency range, which is a result of the applied background correction method of measurement. The bad duty cycle for this experimental setup has to be compensated by long accumulation times in order to achieve an acceptable S/N-ratio of the spectrum (cf. chap. 4.2.3.2). As the intensity of the excitation laser is not constant for such time frames, the background correction of the emission spectra leads to signal fluctuations, when the excitation frequency is in the range of the spectrum. In the case of the spectrum shown in fig. 6.14 the excitation frequency coincides with the origin of the dispersed emission. This complicates the determination of the intensity and exact position of the signal, but identifies the signal at $\nu = 27610$ cm$^{-1}$ as the electronic origin of an An(Ar) isomer in helium droplets. To avoid the background correction problem the dispersed emission should be recorded upon excitation of a vibronic transition, so that the laser frequency is not in the range of the spectrum. However, the much lower fluorescence intensities of the vibronic transitions did not allow for such a measurement with acceptable S/N-ratio.

The dispersed emission of the second An(Ar) isomer was recorded for excitation at 27579 cm$^{-1}$ and at 27964.5 cm$^{-1}$, the latter corresponding to the excitation of the 385.5 cm$^{-1}$ mode in the $S_1$. The spectra are shown in fig. 6.15.

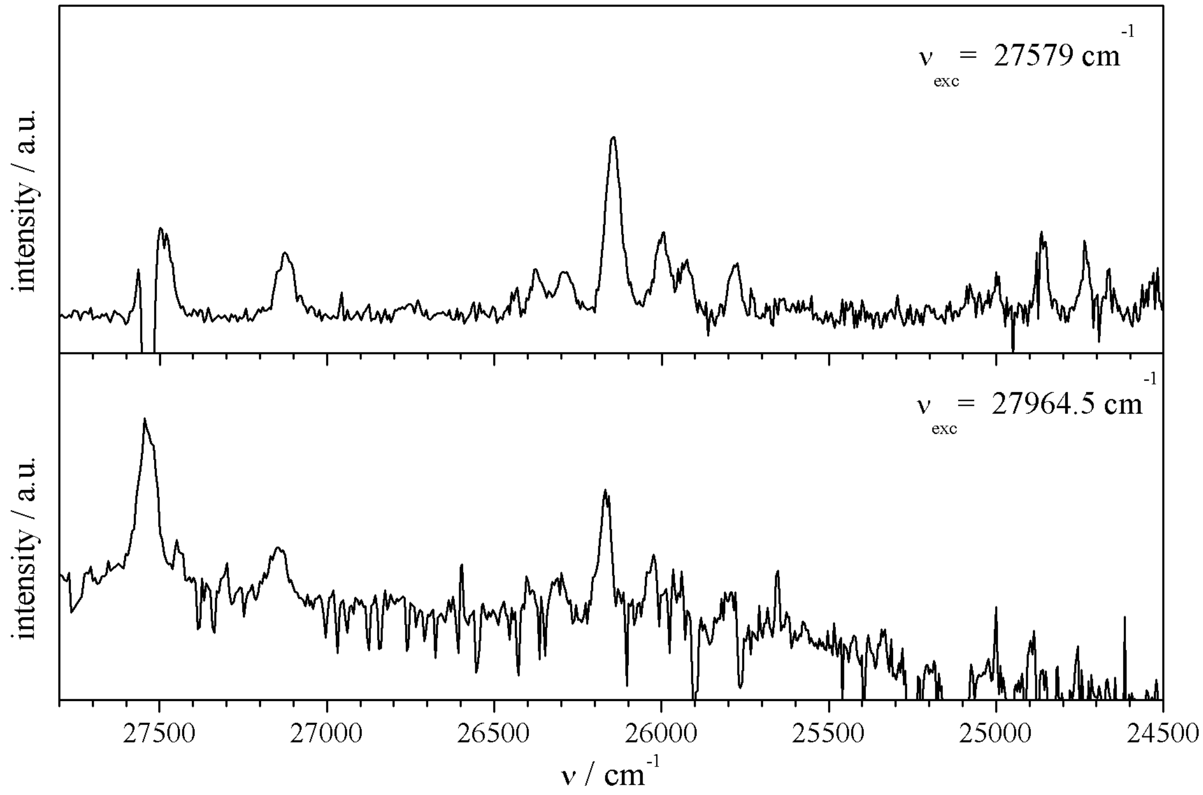

**Fig. 6.15:** Emission spectrum of An(Ar) in helium droplets recorded upon excitation at $\nu_{exc} = 27579$ cm$^{-1}$ and $\nu = 27964.5$ cm$^{-1}$. The electronic origin in both spectra is identified at about $\nu = 27563$ cm$^{-1}$. Emission was dispersed with the 1200 lines/mm grating of the spectrograph. The distance between two pixel columns amounts to about 6.5 cm$^{-1}$ at the blue and 5.4 cm$^{-1}$ at the red end of the spectrum.

As typical for species embedded in helium droplets the emission spectra are identical and therefore independent of the excitation frequency. They differ only in the signal intensity of the origin, which is identified at $\nu = 27563$ cm$^{-1}$. This is again a result of the background correction problem, when the signal coincides with the excitation frequency as in the case of the spectrum shown in the upper panel of fig. 6.15. However, the negative spikes in the spectrum shown in the lower panel of fig. 6.15 indicate that also in this measurement some systematic error might be involved, possibly due to the background correction. Both spectra demonstrate that in consideration of the experimental accuracy the origin of the emission is in agreement with the excitation frequency at 27579 cm$^{-1}$. This proves that the corresponding signal belongs to the electronic origin of a second An(Ar) cluster in helium droplets.

Within experimental accuracy the vibronic transitions observed in the An(Ar) emission spectra (fig. 6.14 and fig. 6.15) possess the same vibrational frequencies and relative intensities as the ones observed for the emission of bare An in helium droplets (fig. 6.2). It shows that the formation of An(Ar) clusters does not change the vibrational energy in comparison with bare An. This applies to the van der Waals cluster with the Ar atom directly attached to the An molecule as well as to the one with the Ar atom attached to the helium layer around An.

## 6.5 Anthracene-Ar$_2$

In the following the An(Ar)$_2$ cluster spectra in helium droplets are discussed in detail. Therefore, the particle density of Ar in the gas pick-up cell was optimized for maximum intensities of the An(Ar)$_2$ transitions for all measurements presented in this section. The fluorescence excitation spectra were measured with 13 datapoints per 1 cm$^{-1}$. Details on the resolution of the emission spectra are discussed in the text.

### 6.5.1 Fluorescence Excitation

In the fluorescence excitation spectrum of An(Ar)$_k$ clusters in helium droplets several signals belonging to van der Waals clusters consisting of one An molecule and two Ar atoms are observed. Both for post pick-up as well as prior pick-up measurements the most intense peak shows a red shift of 87 cm$^{-1}$ to the electronic origin of bare An in helium droplets at $\nu_0 = 27622\ \mathrm{cm}^{-1}$. Several additional signals with lower intensities appear in the frequency range from $\nu - \nu_0 =$ -86 $\mathrm{cm}^{-1}$ to $\nu - \nu_0 =$ -54 $\mathrm{cm}^{-1}$. From these signals the lines with a red shift of 57 $\mathrm{cm}^{-1}$, 79 $\mathrm{cm}^{-1}$ and 83 $\mathrm{cm}^{-1}$ relative to $\nu_0$ were singled out for further investigations because of their saturation behavior, which distinguishes them from neighboring signals. A further signal assigned to an $\mathrm{An(Ar)_2}$ cluster appears only for a post pick-up order of the cluster formation. It shows a small red shift of $\nu - \nu_0 =$ -25 $\mathrm{cm}^{-1}$ and a rather small signal intensity. The assignment of the signals to an $\mathrm{An(Ar)_2}$ cluster stoichiometry was undertaken for both pick-up orders, if possible. For the selected signals the Poisson distribution with $k = 2$ could be fitted with a high accuracy to the data sets. Fig. 6.8 and fig. 6.9 demonstrate that the resultant graphs are in good accordance with the data points.

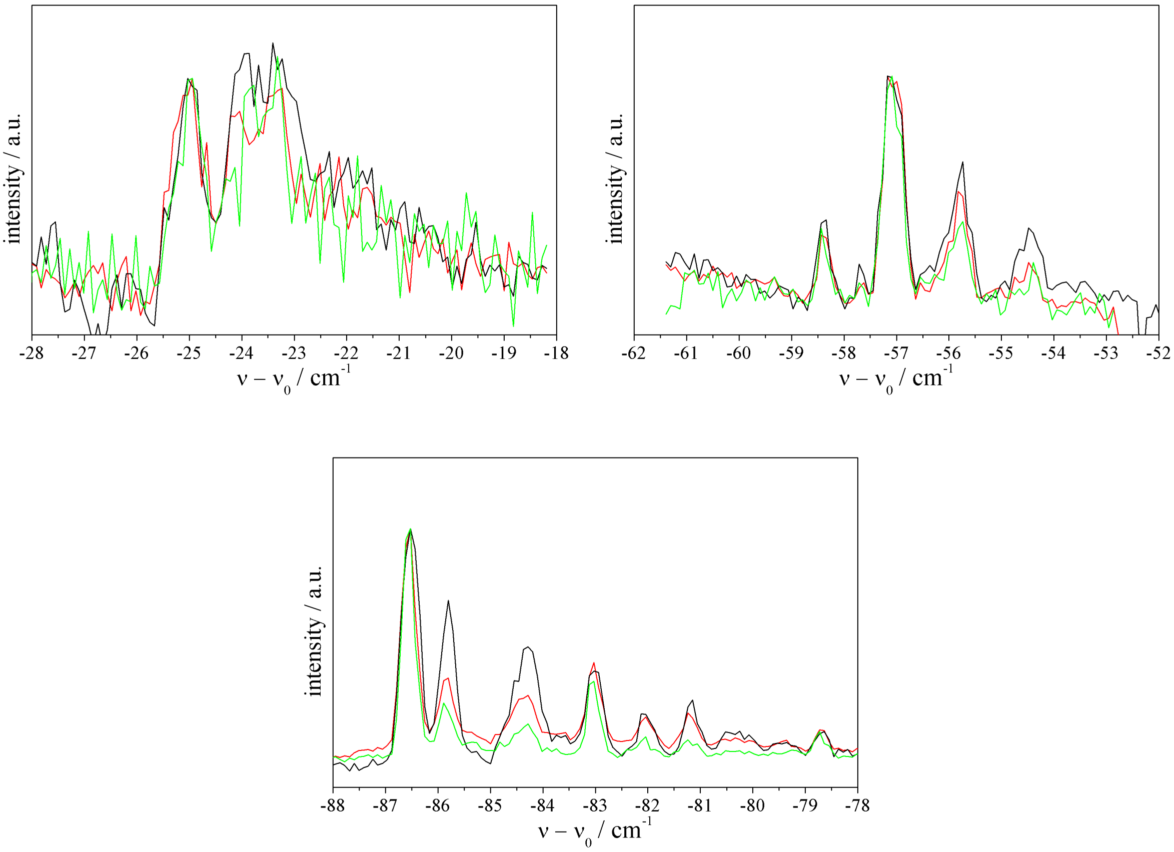

**Fig. 6.16:** Fluorescence excitation spectra of $\mathrm{An(Ar)_2}$ clusters in helium droplets measured with 13 datapoints per 1 $\mathrm{cm}^{-1}$. The clusters were formed in a post pick-up process and the graphs correspond to measurements with the laser intensity increasing by an order of magnitude from the green to the black spectrum. The wavenumber is given relative to $\nu_0 = 27622\ \mathrm{cm}^{-1}$. The graphs are normalized to the most intense peak in each panel.

The high resolution fluorescence excitation spectra of these $An(Ar)_2$ clusters are shown in fig. 6.16. Each spectrum was recorded three times with different laser intensities. From the green to the black spectra the intensity of the laser increases by about an order of magnitude. The wavenumber is given relative to the electronic origin of bare An in helium droplets at $\nu_0 = 27622$ cm$^{-1}$ and the graphs are normalized to the most intense peak in each panel. The figure demonstrates the different saturation behavior of the selected signals shifted -57 cm$^{-1}$, -79 cm$^{-1}$, -83 cm$^{-1}$ and -87 cm$^{-1}$ to $\nu_0$ in comparison with their neighboring lines. These lines accompany the selected signals with a shift of about 1 cm$^{-1}$ or 2.5 cm$^{-1}$ to the blue. As explained in detail in chap. 3.1, their blue shift and their saturation behavior might be indicative for PWs. A definite assignment is, however, unfeasible, as maxima of PWs can not be distinguished from signals belonging to molecular transitions of cluster isomers in helium droplets, which exhibit lower transition moments. The latter explanation could also apply for the signal at $\nu - \nu_0 =$ -59.5 cm$^{-1}$, which appears to the red of one of the selected peaks. The $An(Ar)_2$ signal with the smallest red shift to the electronic origin of bare An is the one at $\nu - \nu_0 =$ -25 cm$^{-1}$. It is very weak and therefore the S/N-ratio in the left upper panel of fig. 6.16 is poor. In addition to the sharp peak at $\nu - \nu_0 =$ -25 cm$^{-1}$ a broader line appears with a shift of about 1 cm$^{-1}$ to the blue. Due to the characteristic blue shift and the broad structure of this peak its assignment to a PW can be suggested. However, this thesis is countered by the fact that both lines show the same reaction to changes in the excitation laser's intensity. Unfortunately the low signal intensity did not allow for further spectroscopic investigations, which would help to assign the individual lines. For the vibronic transition of the clusters with $\nu_{vib} = 385.5$ cm$^{-1}$ a similar signal pattern as the one shown in fig. 6.16 was observed.

When discussing $An(Ar)_k$ clusters with $k > 1$, one has to distinguish between one-sided and two-sided isomers, i.e. between clusters with all Ar atoms on the same side of the An plane and clusters with Ar atoms on both sides of the molecular plane. For this distinction between structural isomers of a van der Waals cluster with a given total number of Ar atoms $k$ the classification $(k'|k - k')$ is used to denote the number of Ar atoms on each side of the An molecule, as in previous studies (e.g. in [SBHEJ91, UBD$^+$98, HLTV98]). In the case of An(Ar)$_2$ clusters the formation of (2|0) isomers and (1|1) isomers is possible, although research regarding An(Ar)$_2$ in the gas phase revealed that in supersonic jet experiments only signals belonging to a (2|0) isomer could be assigned [UBD$^+$98] in contrast to earlier statements [HYS$^+$85, SBHEJ91].

As discussed above, in helium droplet measurements the formation probability of one-sided and two-sided clusters depends on the pick-up order. In theory, for $k = 2$ this probability is 50 % for each the (1|1) and the (2|0) cluster formation in the case of a post pick-up process. For a prior pick-up procedure this ratio changes leading to a probability of 100 % for the formation of (2|0) clusters. Thus, the change in signal intensity when comparing the excitation spectra for post pick-up and prior pick-up measurements provides additional information, which is not accessible by supersonic jet spectroscopy. For the transitions of An(Ar)$_2$ clusters in helium droplets significant differences in the signal intensities are observed upon changing the pick-up order, as can be seen in fig. 6.6 and tab. 6.1. The signals at $\nu - \nu_0$ = -25 cm$^{-1}$ and $\nu - \nu_0$ = -57 cm$^{-1}$ are considerably reduced in the case of a prior pick-up cluster formation. The other three selected signals assigned to An(Ar)$_2$ clusters show an increased intensity upon prior pick-up. On this basis, an assignment of the signals with a shift of -25 cm$^{-1}$ and -57 cm$^{-1}$ to (1|1) isomers and the signals shifted -79 cm$^{-1}$, -83 cm$^{-1}$ and -87 cm$^{-1}$ to (2|0) isomers can be suggested. Then the ratio of the signal intensities of (1|1) clusters to (2|0) clusters amounts to 31 % to 69 % for post pick-up measurements and to 10 % to 90 % for prior pick-up measurements. This reflects the relation between post and prior pick-up measurements, but disaccords with the statistical values of 50:50 and 0:100. At least in the case of the prior pick-up values this discrepancy can not solely be explained with a different detectability of the (1|1) and (2|0) clusters due to e.g. different transition moments or fluorescence quantum yields. It indicates that either the Ar atoms do not form a stable dimer in the prior pick-up process or that a rearrangement of the Ar atoms is possible in helium droplets despite of the low temperature of 0.37 K. The Ar rearrangement together with the distinct detectability of the individual clusters may also play a role in the post pick-up case and provides an explanation for the discrepancy of the experimental values from the 50:50 statistic.

These observations can be compared with gas phase measurements and with calculations of free An(Ar)$_2$ cluster structures. In the gas phase excitation spectrum signals with shifts relative to the origin of bare An are observed at -49 cm$^{-1}$, -84 cm$^{-1}$ and -97 cm$^{-1}$ [UBD$^+$98] or at -87 cm$^{-1}$ and -98 cm$^{-1}$ [HYS$^+$85]. Of these signals only the one at $\nu - \nu_0$ = -97 cm$^{-1}$ [UBD$^+$98] or $\nu - \nu_0$ = -98 cm$^{-1}$ [HYS$^+$85] was assigned to the origin of an An(Ar)$_2$ cluster. Hole-burning spectra revealed that the low intensity band at $\nu - \nu_0$ = -49 cm$^{-1}$ belongs to the same cluster and can presumably be assigned to a van der Waals mode of this species [UBD$^+$98]. The signal at $\nu - \nu_0$ = -87 cm$^{-1}$ belongs to a cluster of An with water. This was shown by two-color resonant two-photon ionization studies [UBD$^+$98]. The broad band at $\nu - \nu_0$ = -84 cm$^{-1}$ could not be assigned to a distinct cluster structure. Thus, only one intensive An(Ar)$_2$ cluster signal remains in the gas phase excitation spectrum. It is assigned to a (2|0) isomer [UBD$^+$98].

These observations are in contrast to the theoretical studies. Calculations of the intermolecular potential energy for An(Ar)$_2$ clusters with Lennard-Jones type atom-atom potentials revealed four isomeric structures, which produce a minimum energy [HYS$^+$85]. In later publications, using Monte-Carlo simulations only two structures were found [UBD$^+$98]. Both publications agree that the global minimum of the potential energy surface for An(Ar)$_2$ corresponds to a cluster configuration with both Ar atoms located 3.43 Å above the An plane and about 3.80 Å apart from each other, so that they match the An symmetry. Fig. 6.17 shows the spacial probability density distribution of this (2|0) cluster obtained by Monte-Carlo simulations at 10 K [UBD$^+$98]. In addition, both calculations predict the existence of a stable (1|1) cluster with the Ar atoms located 3.43 Å above and below the central ring of the An molecule so that the cluster perfectly matches the An symmetry. The two additional minimum configurations denoted in [HYS$^+$85] both correspond to (2|0) structures with the Ar atoms not matching the An symmetry. According to [SBHEJ91] the $0_0^0$ signals of (1|1) clusters should exhibit larger red shifts to the electronic origin of bare An than the $0_0^0$ signals of (2|0) clusters.

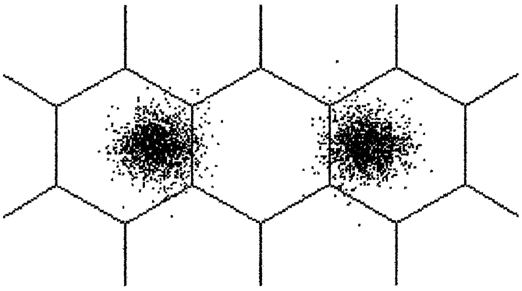

**Fig. 6.17:** Spatial probability density distribution of the one-sided An(Ar)$_2$ cluster obtained by Monte Carlo simulations at 10 K (from [UBD$^+$98]).

The comparison of these results with the helium droplet spectra of An(Ar)$_2$ clusters reveals considerable differences in the quantity and positions of the excitation signals. It is apparent that the helium droplet spectrum exhibits more signals of An(Ar)$_2$ clusters than the corresponding gas phase spectrum, including also transitions of (1|1) isomers. Moreover, the (1|1) cluster signals show smaller red shifts compared to the origin of bare An than the (2|0) cluster signals, which is in contrast to the predictions made for free clusters [SBHEJ91]. However, it can be assumed that the minimum configurations calculated for (2|0) and (1|1) isomers in the gas phase are also existent in helium droplets. Then the predominant An(Ar)$_2$ signal in the helium droplet spectrum at $\nu - \nu_0$ = -87 cm$^{-1}$ presumably belongs to the electronic origin of the An(Ar)$_2$ isomer with the global minimum configuration shown in fig. 6.17. The assignment of this signal to a (2|0) cluster could be demonstrated by its response to the change of pick-up order. Likewise the signal at $\nu - \nu_0$ = -57 cm$^{-1}$ in the helium droplet spectrum can tentatively be assigned to the (1|1) isomer with the Ar atoms located above and below the central ring of the An. However, it must not be forgotten that the droplet environment, which influences the potential energy surface of the An(Ar)$_2$ system, is not respected in the theoretical work. Therefore, a definite assignment of the An(Ar)$_2$ cluster configurations formed in helium droplets is not possible on the basis of these calculations.

When comparing these observations with the studies on clusters consisting of one tetracene molecule and two argon atoms similarities can be noticed. In the excitation spectra of tetracene-Ar$_2$ in helium droplets transitions of several different isomers could be recorded. These were identified as arising from one-sided and two-sided clusters, although only a transition of one (2|0) cluster was observed in gas phase measurements [HLTV98]. This effect observed for clusters of An(Ar)$_2$ as well as clusters of tetracene-Ar$_2$ suggests that the droplet environment either stabilizes the two-sided cluster structures or promotes their formation process e.g. by rearrangement of the Ar atoms around the chromophore molecule.

### 6.5.2 Dispersed Emission

Dispersed emission spectroscopy was applied in order to check whether the selected excitation signals discussed in the last preceding section belong to separate electronic origins of individual An(Ar)$_2$ clusters. Emission was measured upon excitation of the transitions at $\nu - \nu_0$ = -57 cm$^{-1}$ , $\nu - \nu_0$ = -83 cm$^{-1}$ and $\nu - \nu_0$ = -87 cm$^{-1}$, for these exhibit sufficient fluorescence to reach an acceptable S/N-ratio in the emission spectra. Unfortunately, the signals shifted $\nu - \nu_0$ = -25 cm$^{-1}$ and $\nu - \nu_0$ = -79 cm$^{-1}$ in the excitation spectrum of An(Ar)$_2$ in helium droplets could not be analyzed with dispersed emission spectroscopy, for the S/N-ratio in the spectra is to poor to obtain reasonable information.

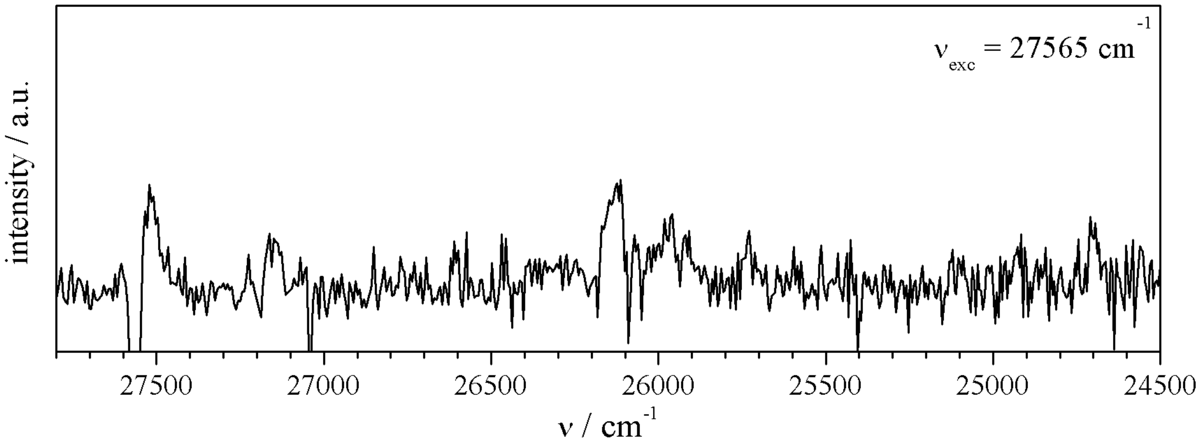

**Fig. 6.18:** Emission spectrum of An(Ar)$_2$ in helium droplets recorded upon excitation at $\nu_{exc}$ = 27565 cm$^{-1}$. The electronic origin is identified at about $\nu$ = 27553 cm$^{-1}$. Emission was dispersed with the 1200 lines/mm grating of the spectrograph. The distance between two pixel columns amounts to about 6.5 cm$^{-1}$ at the blue and 5.4 cm$^{-1}$ at the red end of the spectrum.

The spectrum of fig. 6.18 was recorded upon excitation at 27565 $\mathrm{cm}^{-1}$, which corresponds to the excitation of the transition shifted 57 $\mathrm{cm}^{-1}$ to the red of the electronic origin of bare An in helium droplets. The position of the electronic origin of the emission spectrum coincides with the excitation frequency. This provokes again the background correction problem discussed in chap. 6.4.2, but at the same time identifies the signal at $\nu = 27565$ $\mathrm{cm}^{-1}$ as the electronic origin of the cluster in helium droplets. Despite of the poor S/N-ratio the characteristic vibronic pattern of An in helium droplets can be observed in this emission spectrum. It shows that the formation of an (1|1) isomer of $\mathrm{An(Ar)_2}$ does not influence the vibrational energies in the ground state of An.

The emission spectra recorded upon excitation at 27539 $\mathrm{cm}^{-1}$ and 27535 $\mathrm{cm}^{-1}$ can be seen in fig. 6.19. This corresponds to an excitation of the transitions at $\nu - \nu_0$ = -83 $\mathrm{cm}^{-1}$ and $\nu - \nu_0$ = -87 $\mathrm{cm}^{-1}$ in the excitation spectrum in helium droplets.

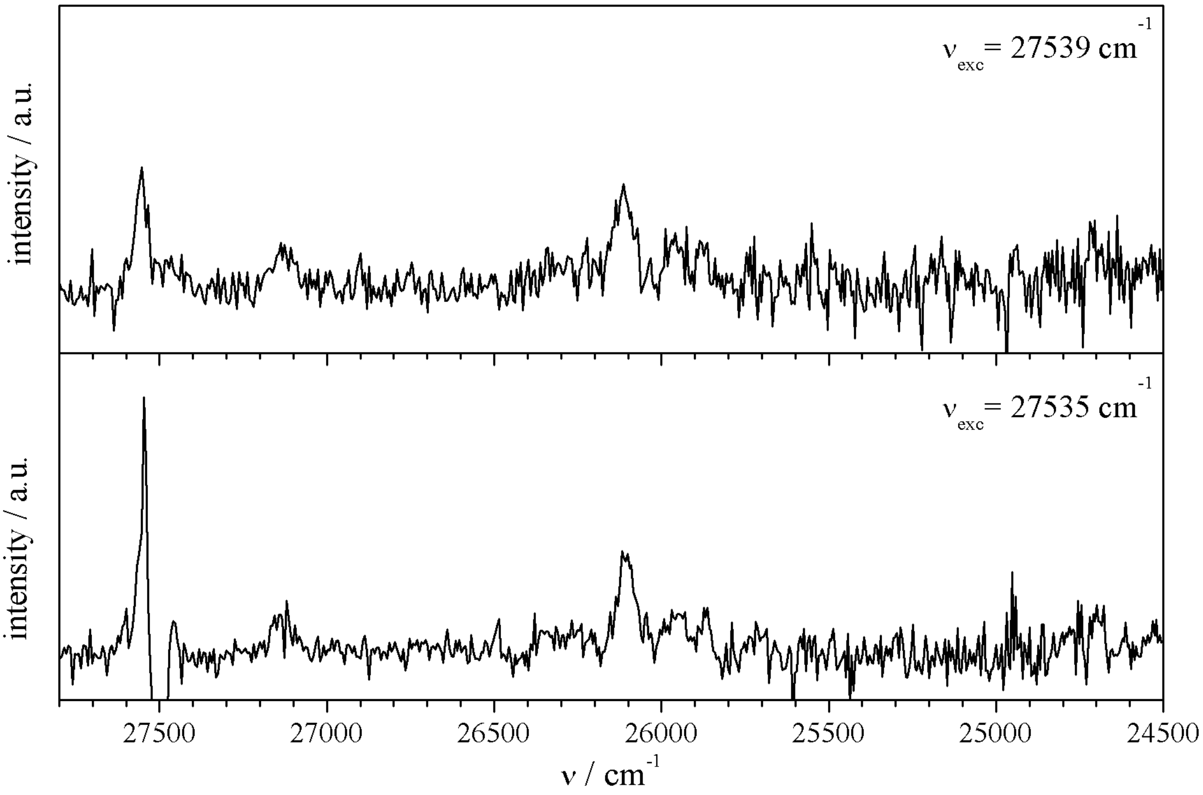

**Fig. 6.19:** Emission spectra of $\mathrm{An(Ar)_2}$ in helium droplets recorded upon excitation at $\nu_{exc} = 27539$ $\mathrm{cm}^{-1}$ and at $\nu_{exc} = 27535$ $\mathrm{cm}^{-1}$. Emission was dispersed with the 1200 lines/mm grating of the spectrograph. The distance between two pixel columns amounts to about 6.5 $\mathrm{cm}^{-1}$ at the blue and 5.4 $\mathrm{cm}^{-1}$ at the red end of the spectrum.

Both spectra exhibit the characteristic vibronic pattern observed for the emission of An in helium droplets. Unfortunately, it is not possible to gauge the exact position of the maximum intensity of the origins in the spectra of fig. 6.19. This is due to the poor spectral resolution and the background correction problem, which provokes a distortion of the signals at the origins of the emission. Therefore, no reliance can be placed on the intensity of these signals in the emission spectra and it becomes impossible to determine, whether the emission stems from the same cluster or from two separate systems.

To answer this question, the experiment was repeated using the 3600 lines/mm grating of the spectrograph, which offers a much better spectral resolution. The spectra are shown in fig. 6.20.

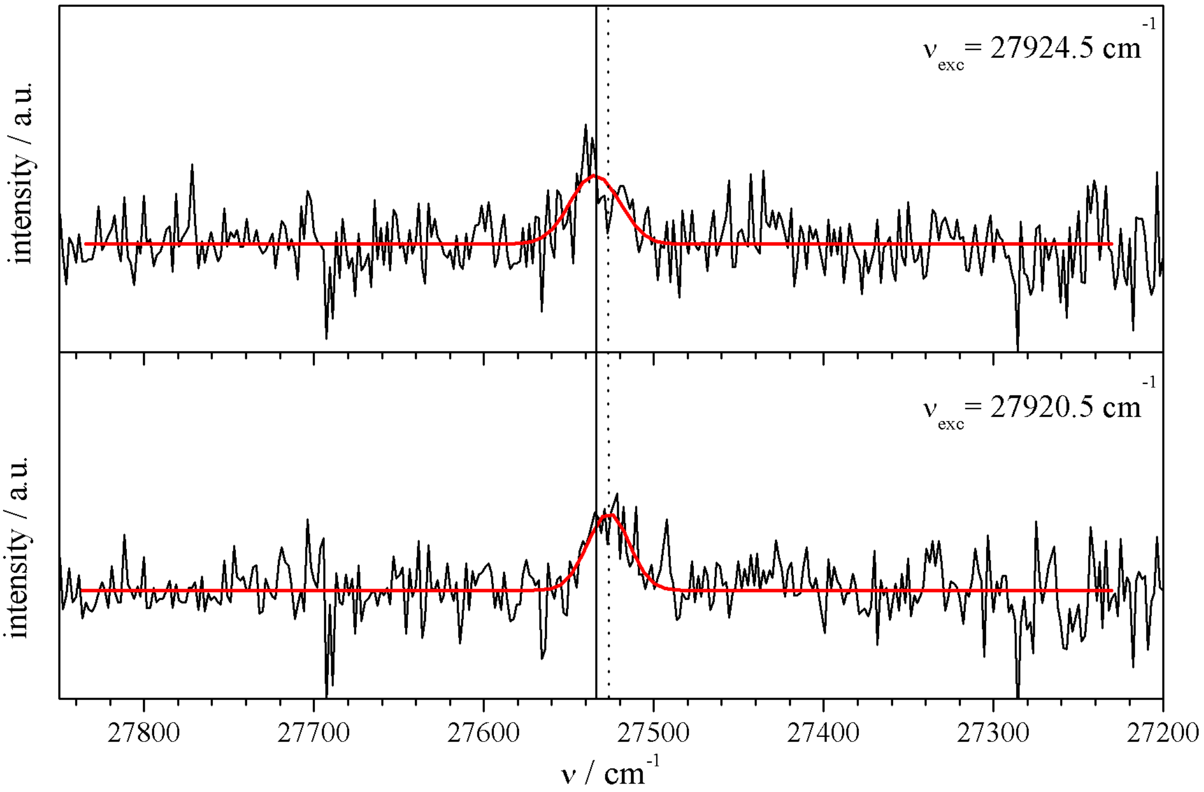

**Fig. 6.20:** Emission spectra of An(Ar)$_2$ in helium droplets recorded with the 3600 lines/mm grating of the spectrograph. The excitation frequency was $\nu_{exc}$ = 27924.5 cm$^{-1}$ and $\nu_{exc}$ = 27920.5 cm$^{-1}$, respectively. The solid line marks the position of the electronic origin in the upper panel at about $\nu$ = 27538 cm$^{-1}$. The dotted line marks the position of the electronic origin in the lower panel at about $\nu$ = 27529 cm$^{-1}$. The distance between two pixel columns amounts to about 1.9 cm$^{-1}$ at the blue and 1.7 cm$^{-1}$ at the red end of the spectrum.

To avoid the background correction problem discussed above emission was recorded upon excitation at $\nu_{exc} = 27924.5$ cm$^{-1}$ and $\nu_{exc} = 27920.5$ cm$^{-1}$, which corresponds to the excitation of the 385.5 cm$^{-1}$ mode in the $S_1$ state. However, this leads to a loss in the S/N-ratio of the spectra due to smaller transition moments at the excitation. Gaussian functions were fitted to the low intensity signals using the data analysis procedure of OriginPro 8. The solid line in fig. 6.20 marks the position of the maximum of the fitted graph in the upper panel at 27534 cm$^{-1}$. The dotted line marks the maximum of the Gaussian function in the lower panel at 27527 cm$^{-1}$. These different frequencies indicate that the two emission spectra of fig. 6.20 show separate origins. If this is the case, the emission would originate from two different excited states, presumably belonging to two different isomers of An(Ar)$_2$ clusters. However, the S/N-ratio of the spectra is rather poor and the Gaussian fits do not exhibit the same width. This puts into question the validity of the analysis. These measurements show that the experimental setup using a L.O.T.-Oriel MS257 spectrograph with a grating $\leq$ 3600 lines/mm does not suffice to distinguish between cluster signals, which are only 4 cm$^{-1}$ apart.

## 6.6 Anthracene-Ar$_3$

This section regards An(Ar)$_3$ clusters in helium droplets. Therefore, all spectra shown in the following were recorded after optimizing the Ar particle density in the gas pick-up cell for maximum intensities of the An(Ar)$_3$ transitions. The excitation spectra were measured with 13 datapoints per 1 cm$^{-1}$. The emission was dispersed with the 1200 lines/mm grating of the spectrograph leading to a distance between two pixel columns of about 6.5 cm$^{-1}$ at the blue and 5.4 cm$^{-1}$ at the red end of the spectrum.

### 6.6.1 Fluorescence Excitation

Two of the selected signals in the fluorescence excitation spectrum of An(Ar)$_k$ in helium droplets are assigned to clusters consisting of one An molecule and three Ar atoms. They differ considerably in signal intensity and are shifted 96 cm$^{-1}$ and 119 cm$^{-1}$ to the red of the electronic origin of bare An in helium droplets at $\nu_0$ = 27622 cm$^{-1}$. As can be seen in fig. 6.6 the peak with a larger red shift shows a high signal intensity for post pick-up as well as prior pick-up measurements. Compared with this peak the signal at $\nu - \nu_0$ = -96 cm$^{-1}$ exhibits a relative intensity of about 15%. This is only the case for a post pick-up cluster formation, as the peak misses completely if the clusters are formed in a prior pick-up process. Thus, the assignment of the signal at $\nu - \nu_0$ = -119 cm$^{-1}$ via Poisson distribution fitting was undertaken for both pick-up conditions, but the assignment of the signal at $\nu - \nu_0$ = -96 cm$^{-1}$ could only be conducted with post pick-up data. The fitted graphs accordance with the data sets can be seen in fig. 6.8 and fig. 6.9.

The high resolution excitation spectra of the two signals are shown in fig. 6.21 normalized to the most intense peak in each panel. The laser intensities increase by an order of magnitude from the green to the black spectra. The wavenumber is given relative to the electronic origin of bare An in helium droplets at $\nu_0$ = 27622 cm$^{-1}$.

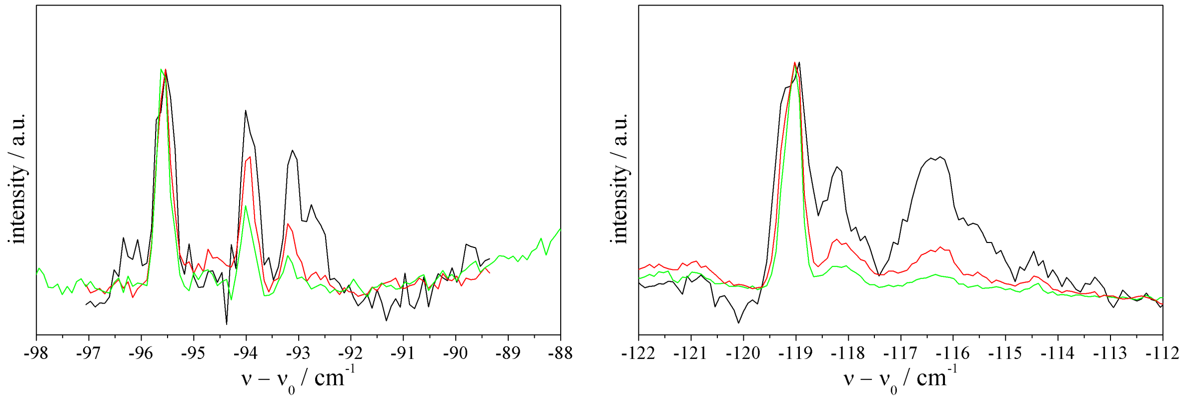

**Fig. 6.21:** Fluorescence excitation spectra of An(Ar)$_3$ clusters in helium droplets measured with 13 datapoints per 1 cm$^{-1}$. The clusters were formed in a post pick-up process and the graphs correspond to measurements with the laser intensity increasing by an order of magnitude from the green to the black spectrum. The wavenumber is given relative to $\nu_0$ = 27622 cm$^{-1}$. The graphs are normalized to the most intense peak in each panel.

As can be seen in the two panels each of the main peaks at $\nu - \nu_0$ = -96 cm$^{-1}$ and $\nu - \nu_0$ = -119 cm$^{-1}$ is accompanied by two lines shifted to the blue, which show a saturation behavior differing from the one of the main peaks. They are tentatively assigned to PWs accompanying the cluster transitions, but other explanations for these signals can not be excluded with certainty as discussed above (cf. chap. 3.1).

To distinguish between one-sided and two-sided isomers of An(Ar)$_3$ clusters the response of the fluorescence signals to the pick-up order is analyzed. For $k = 3$ the formation of one-sided (3|0) clusters and of two-sided (2|1) is possible. In theory, the probability for a two-sided cluster formation is 75 % in the post pick-up case and 0 % in the prior pick-up case. For the one-sided isomers the formation probability changes from 25 % for a post pick-up process to 100 % for a prior pick-up process. These values are based on the assumption that in the prior pick-up case a stable Ar$_3$ cluster is formed before the An doping and that the chromophore coagulates with this Ar$_3$ structure. For the post pick-up case equal probabilities are assumed for each Ar atom to attach itself to one side of the An plane or the other. In fact, a significant difference when changing from a post to a prior pick-up measurement can be observed for the signal at $\nu - \nu_0 =$ -96 cm$^{-1}$. The comparison of the spectra in fig. 6.6 reveals that this signal appears only for a post pick-up formation of the clusters. On this basis, the signal at $\nu - \nu_0 =$ -96 cm$^{-1}$ is assigned to a two-sided (2|1) isomer of An(Ar)$_3$. In contrast, the signal at $\nu - \nu_0 =$ -119 cm$^{-1}$ shows an increase in signal intensity, when changing from a post to a prior pick-up order. Therefore, its assignment to a (3|0) cluster can be suggested. Consequently, the ratio of the intensities of the (2|1) cluster signal to the (3|0) cluster signal amounts to 13 % to 87 % in the post pick-up case and to 0 % to 100 % in the prior pick-up case. For a prior pick-up cluster formation these values are in agreement with the statistic, which supports the validity of the suggested assignment. However, an explicit discrepancy between the theoretical and the experimental values is observed for the post pick-up case. One reason for this discrepancy may be the different excitation probability of the individual clusters. In addition, their distinct fluorescence quantum yields also influence the signal intensity. Both parameters are specific for each cluster and determine its detectability by fluorescence excitation spectroscopy. Thus, they may influence the intensity ratio of the (3|0) and (2|1) cluster signals. Another process, which may play a role in the explanation of the intensity ratio observed for the post pick-up measurement, is the possible rearrangement of Ar atoms in helium droplets, which was already discussed for An(Ar)$_2$ clusters. Such a rearrangement would directly influence the formation probability of distinct cluster structures. As the deviation of the experimental values from the 75:25 statistic is large, presumably all the discussed aspects are involved in the experiment on An(Ar)$_3$ clusters formed in a post pick-up process, though it is not known to what extent.

In calculations of the molecular potential energy for An(Ar)$_3$ clusters with Lennard-Jones type atom-atom potentials as well as in Monte Carlo simulations only one minimum energy structure is found for a (2|1) isomer [HYS$^+$85, UBD$^+$98]. In this configuration on one side of the An molecule a single Ar atom occupies the center position 3.43 Å above the middle ring. On the other side of the An molecule the positions of the two Ar atoms correspond to the global minimum structure for (2|0) clusters of An(Ar)$_2$ with the Ar atoms 3.80 Å apart from each other while matching the An symmetry (cf. fig. 6.17). The main signal of An(Ar)$_3$ observed in gas phase measurements is assigned to this (2|1) cluster [HYS$^+$85]. It appears with a red shift of 137 cm$^{-1}$ to the electronic origin of bare An. Also in later publications this signal is reported and assigned to a (2|1) cluster, while no evidence is found for the formation of a one-sided An(Ar)$_3$ cluster in the gas phase [SBHEJ91, UBD$^+$98].

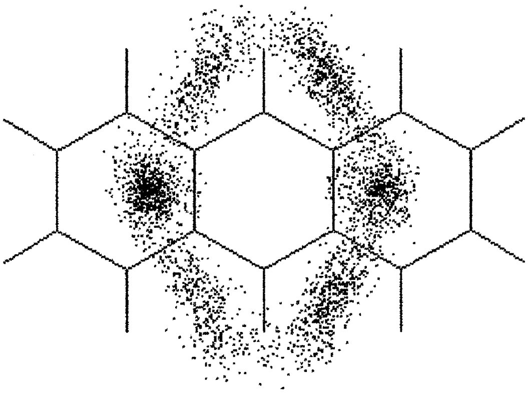

**Fig. 6.22:** Spatial probability density distribution of the one-sided An(Ar)$_3$ cluster obtained by Monte Carlo simulations at 10 K (from [UBD$^+$98]).

This is in contrast to calculations of the molecular potential energy for An(Ar)$_3$ clusters with Lennard-Jones type atom-atom potentials, since they reveal two (3|0) structures, which produce a minimum energy [HYS$^+$85]. When using Monte Carlo simulations only one minimum structure is found for a (3|0) isomer [UBD$^+$98]. It is reported that enantiomeric forms of this cluster exist and that isomerization is observed between these forms for simulations at 10 K. Fig. 6.22 shows the spacial probability density distribution of the (3|0) cluster obtained by Monte Carlo simulations at 10 K. However, as no excitation signals of one-sided An(Ar)$_3$ clusters are observed in the supersonic jet measurements, these structures seem to be unstable in the gas phase. Apparently the An(Ar)$_3$ cluster formation in helium droplets differs greatly from the one in the gas phase. This is most obvious for the (3|0) isomer, which exhibits one of the most intense lines in the helium droplet excitation spectrum, while it is not observed at all in the gas phase measurements. Conversely, the (2|1) cluster signal is the predominant line observed in the gas phase spectrum for An(Ar)$_3$, while even for a post pick-up cluster formation it exhibits only a very small intensity in the helium droplet spectrum. On the basis of these results an assignment of the cluster structures formed in helium droplets to the minimum energy configurations calculated for the free clusters seems rather ambitious. Thus, no suggestions can be made regarding the configurations the An(Ar)$_3$ isomers adopt in a droplet environment.

Comparing these observations with the results for tetracene-Ar$_3$ clusters in helium droplets a significant difference in the number of excitation signals stands out [HLTV98]. For the tetracene clusters two excitation signals are assigned to discrete (3|0) isomers in addition to the predominant (2|1) cluster peak and several undefined signals. In the case of An(Ar)$_3$ evidence is found only for one (3|0) isomer and one (2|1) isomer. The reason for this difference is probably the size of the organic chromophore. With an aromatic structure consisting of four six-membered rings the tetracene plane offers more possibilities for the arrangement of the Ar atoms. In the case of three Ar atoms located on the same side of the chromophore the formation of stable isomeric structures in helium droplets is apparently still possible for tetracene, but not for anthracene.

### 6.6.2 Dispersed Emission

In addition to the fluorescence excitation measurements the one-sided An(Ar)$_3$ cluster was also examined using emission spectroscopy. This was not possible for the two-sided isomer of An(Ar)$_3$ due to the low fluorescence intensity of its transitions. The dispersed emission spectrum shown in fig. 6.23 was recorded upon excitation at 27503 cm$^{-1}$, which corresponds to the excitation of the transition with a shift of -119 cm$^{-1}$ to the $0_0^0$ transition of bare An in helium droplets. The origin of this spectrum is identified at $\nu$ = 27493 cm$^{-1}$. Thus, within experimental accuracy it is in agreement with the excitation frequency and is therefore identified as the electronic origin of the (3|0) cluster.

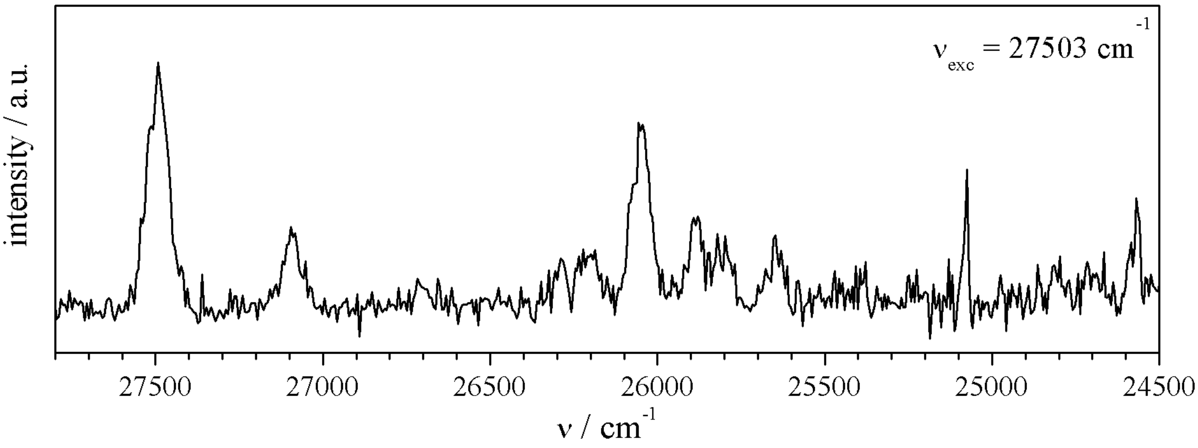

**Fig. 6.23:** Emission spectrum of An(Ar)$_2$ in helium droplets recorded upon excitation at $\nu_{exc}$ = 27503 cm$^{-1}$. The electronic origin is identified at about $\nu$ = 27493 cm$^{-1}$. Emission was dispersed with the 1200 lines/mm grating of the spectrograph. The distance between two pixel columns amounts to about 6.5 cm$^{-1}$ at the blue and 5.4 cm$^{-1}$ at the red end of the spectrum.

However, as excitation and emission occur in the same frequency range, the background correction influences the signal intensity in this region and the exact position of the origin of the emission is therefore difficult to determine (cf. chap. 6.4.2). The characteristic vibronic pattern observed in the emission spectra of bare An and all small An(Ar)$_k$ clusters in helium droplets so far can also be identified in fig. 6.23. It demonstrates that the formation of small An(Ar)$_k$ clusters does not change the vibrational energies in the ground state in comparison with bare An in helium droplets.

# 6.7 Anthracene-Ar$_k$ with k $\geq$ 4

The following section discusses the fluorescence excitation and dispersed emission spectroscopy of clusters consisting of one An molecule and a large number of Ar atoms. The adjustment of the Ar particle density in the gas pick-up cell is given for each spectrum.

## 6.7.1 Fluorescence Excitation

When considering large An(Ar)$_k$ clusters in helium droplets, the difference between those clusters still producing sharp peaks in the excitation spectrum and those producing broad signals has to be taken into account.

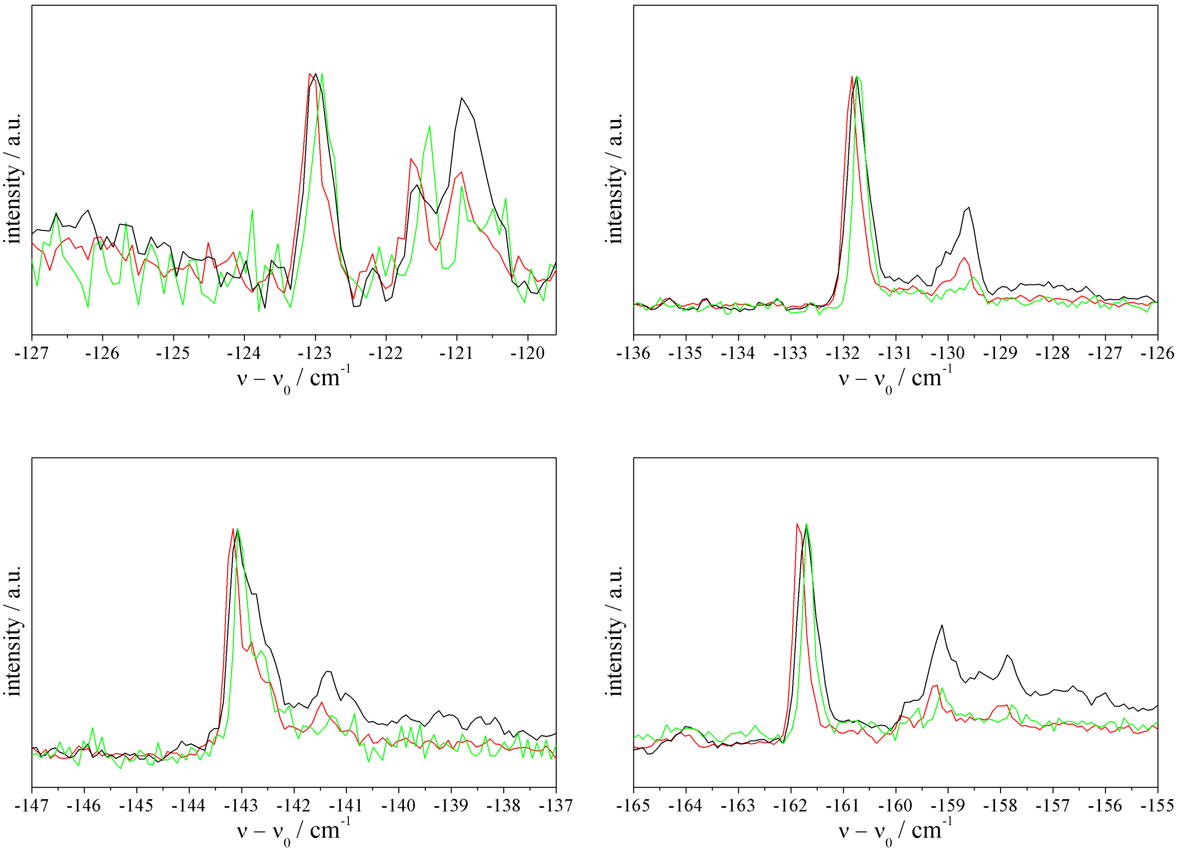

**Fig. 6.24:** Fluorescence excitation spectra of An(Ar)$_4$ clusters in helium droplets measured with 13 datapoints per 1 cm$^{-1}$. The clusters were formed in a post pick-up process and the graphs correspond to measurements with the laser intensity increasing by an order of magnitude from the green to the black spectrum. The wavenumber is given relative to $\nu_0 = 27622$ cm$^{-1}$. The graphs are normalized to the most intense peak in each panel.

In the frequency range from 27452 cm$^{-1}$ to 27502 cm$^{-1}$ four sharp signals with a line width of about 0.5 cm$^{-1}$ appear. According to the analysis presented in chap. 6.3 these signals are assigned to An(Ar)$_4$ clusters. The signal intensities of these transitions are clearly influenced by the pick-up order, as can be seen in fig. 6.6. For An(Ar)$_4$ clusters formed in a post pick-up the signal at $\nu - \nu_0 =$ -162 cm$^{-1}$ is the predominant line, while for a prior pick-up process the predominant signal is observed at $\nu - \nu_0 =$ -123 cm$^{-1}$. Fig. 6.24 shows the high resolution excitation spectra of the four transitions recorded with different laser intensities. The wavenumber is given relative to the $0_0^0$ transition of bare An in helium droplets at $\nu_0 = 27622$ cm$^{-1}$ and the laser intensities increase by an order of magnitude from the green to the black spectra. The graphs are normalized to the most intense peak in each panel. The four main lines with a red shift of 123 cm$^{-1}$, 132 cm$^{-1}$, 143 cm$^{-1}$ and 162 cm$^{-1}$ to $\nu_0$ are all accompanied by signals shifted between 2 cm$^{-1}$ and 3 cm$^{-1}$ to the blue. These features are broader than the main signals, but show a substructure with distinct maxima. Due to their saturation behavior and characteristic blue shift an assignment of these lines to PWs can be suggested. However, this assignment is not definite as Pws can not be distinguished with certainty from molecular transitions of clusters in helium droplets (cf. chap. 3.1).

As for the other An(Ar)$_k$ clusters with $k > 1$ the influence of the pick-up order on the signal intensities helps to distinguish between transitions of one-sided and two-sided isomers. In the case of An(Ar)$_4$ the formation of one-sided (4|0) isomers and of two-sided (3|1) and (2|2) isomers has to be considered. The only one of the selected An(Ar)$_4$ cluster signals showing a clear intensity increase upon changing from a post to a prior pick-up process is the one at $\nu - \nu_0 =$ -123 cm$^{-1}$. On this basis it can certainly be assigned to a one-sided An(Ar)$_4$ cluster. A significant difference when changing the pick-up order is also observed for the signals at $\nu - \nu_0 =$ -143 cm$^{-1}$ and $\nu - \nu_0 =$ -162 cm$^{-1}$. These are considerably reduced in their intensity for a prior pick-up cluster formation and thus they are identified as belonging to two-sided An(Ar)$_4$ clusters. For such a case, the formation of (3|1) structures and of (2|2) structures is possible. In theory, their formation probability in a post pick-up procedure is similar with values of 50 % and

37.5 %, respectively, which makes a differentiation on this basis difficult. The signal at $\nu - \nu_0$ = -132 cm$^{-1}$ in the excitation spectrum of An(Ar)$_4$ clusters in helium droplets shows the smallest reaction to a change in the pick-up order. As can be seen in fig. 6.6 and tab. 6.1 it exhibits almost identical intensities for the post and prior pick-up case. This observation deviates considerably from the theory of changing formation probabilities for post and prior pick-up processes and no suggestions can be made for the signal's assignment to a one-sided or two-sided An(Ar)$_4$ cluster. A possible explanation for the discrepancy between the experimental observations and the theory would be a certain degree of rearrangement of the Ar atoms, which was also discussed for the smaller An(Ar)$_k$ clusters.

In gas phase measurements the only signals denoted as belonging to a distinct An(Ar)$_4$ cluster are assigned to a (2|2) isomer by an analysis of the spectral shifts [HYS$^+$85, UBD$^+$98]. However, Monte Carlo simulations on An(Ar)$_4$ revealed several stable minimum energy configurations including one (2|2), one (3|1) and two (4|0) structures [UBD$^+$98]. But it is questionable whether these structures help to make suggestions on the cluster configurations formed in helium droplets. In the case of a prior pick-up process the four Ar atoms coagulate inside the droplet forming an Ar$_4$ cluster before the An molecule is added. Assuming this Ar$_4$ structure is maintained when coagulating with An, a pyramidal configuration of the Ar atoms is more likely than the plane (4|0) minimum energy configurations discussed in [UBD$^+$98]. The (4|0) cluster observed in the helium droplet spectrum is apparently not stable in the gas phase. This reflects again the influence of the helium environment on the cluster formation and stabilization.

For An(Ar)$_k$ clusters with $k > 4$ sharp signals are still observed at $\nu - \nu_0$ = -147 cm$^{-1}$, $\nu - \nu_0$ = -175 cm$^{-1}$ and $\nu - \nu_0$ = -184 cm$^{-1}$. They exhibit a low intensity and presumably belong to clusters consisting of one An molecule and five Ar atoms. For bigger clusters, however, the excitation signals are shifted more than 190 cm$^{-1}$ to the red of the electronic origin of bare An in helium droplets. A differentiation of individual peaks is no longer possible for these transitions as they appear as broad, overlapping features in the excitation spectrum. This can be seen in fig. 6.25.

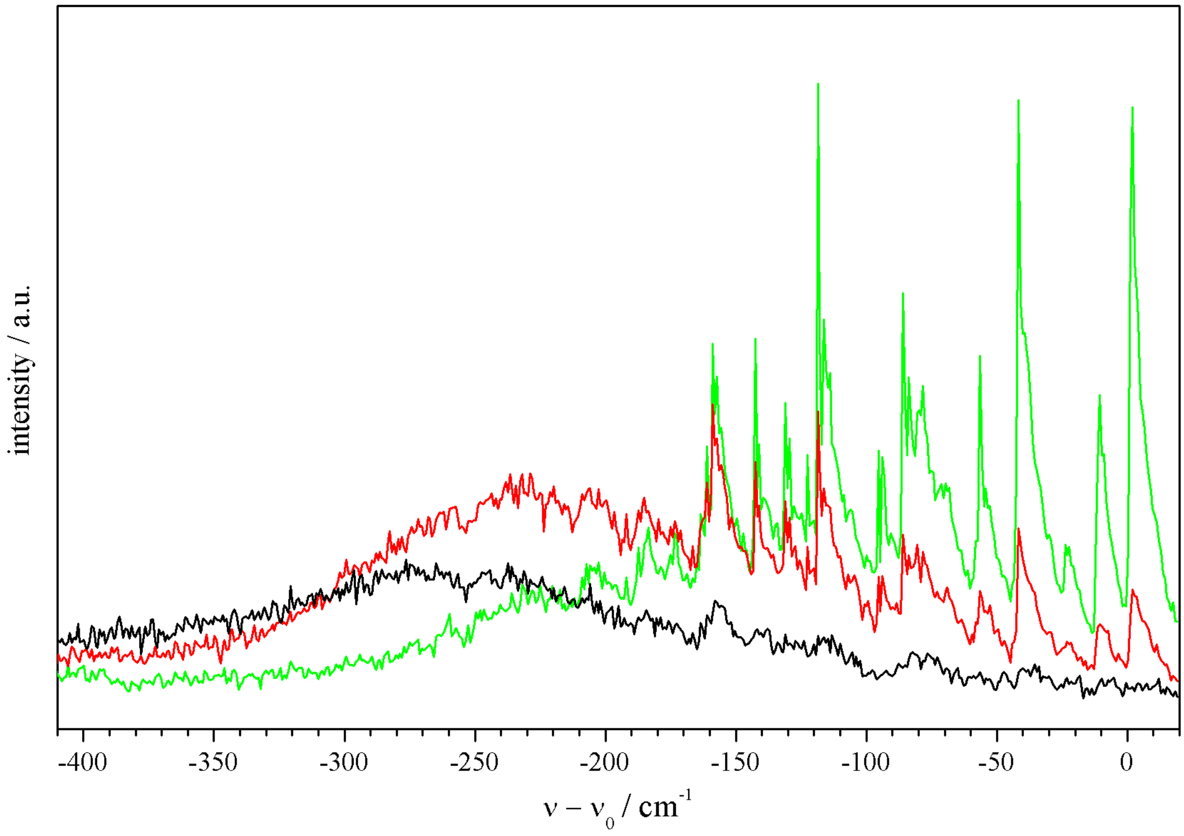

**Fig. 6.25:** Fluorescence excitation spectra of An(Ar)$_k$ clusters in helium droplets recorded for three different adjustments of the Ar particle densities resulting in an average cluster size of $k = 3$ (green), $k = 6$ (red) or $k = 8$ (black). The droplet doping was performed in a post pick-up process. The wavenumber is given relative to the $0^0_0$ transition of bare An in helium droplets at $\nu_0 = 27622$ cm$^{-1}$. The spectra were measured with 1.3 datapoints per 1 cm$^{-1}$.

It shows the fluorescence excitation spectrum of An(Ar)$_k$ clusters in helium droplets in a frequency range from 27212 cm$^{-1}$ to 27642 cm$^{-1}$. The wavenumber is given relative to the $0^0_0$ transition of bare An in helium droplets at $\nu_0 = 27622$ cm$^{-1}$. The helium droplets were doped in a post pick-up process and the spectra were recorded for three different adjustments of the Ar particle densities in the gas pick-up cell. For the green spectrum the Ar pressure was optimized for maximum intensities of the An(Ar)$_3$ cluster transitions. For the red spectrum the adjustment resulted in a maximum of the An(Ar)$_6$ cluster transitions and for the black spectrum it resulted in a maximum of the An(Ar)$_8$ signals. These average values for $k$ were determined using equ. 4.4. The initial droplet size was approximated as $N_0 \approx 10^5$ and the number of helium atoms evaporating upon a single pick-up of an Ar atom as $c \approx 200$ (for details cf. chap. 2). The parameter

$(\alpha\sigma L)$ is known to be $1.9 \cdot 10^9$ A$^{-1}$ $\pm$ $0.4 \cdot 10^9$ A$^{-1}$ from the Poisson fits regarded in chap. 6.3. As to be expected [SBHEJ91], the Ar induced red shift increases with the number of Ar atoms $k$ and is supposed to finally reach the bulk value found in an Ar matrix [FSHD93]. Furthermore, with an increasing An(Ar)$_k$ cluster size congested signals of isomeric clusters and clusters with different $k$ numbers are observed instead of individual sharp peaks. The increase of the width of the cluster size distribution can be estimated for the three Ar adjustments regarded in fig. 6.25. The corresponding Poisson distributions, which can be seen in fig. 6.26, show that the full width at half maximum grows from 3.6 (green) to 5.6 (black).

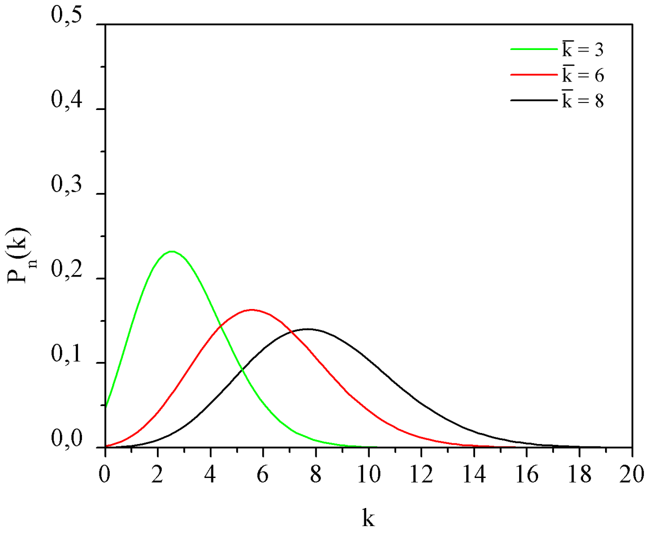

**Fig. 6.26:** Fraction of helium droplets doped with $k$ Ar atoms for three different adjustments of the Ar particle density in the pick-up cell, resulting in an average $k$ number of three (green), six (red) or eight (black).

The excitation signal of An(Ar)$_k$ clusters in helium droplets with the largest red shift could be observed around 27100 cm$^{-1}$, which corresponds to a red shift of 522 cm$^{-1}$ relative to the electronic origin of bare An in helium droplets. The corresponding cluster size is estimated with equ. 4.4 yielding an average $k$ number of 70. However, the full width at half maximum of the size distribution for these Ar doping conditions is about 16. Therefore, the signal is denoted as belonging mainly to clusters with more than 50, but less than 90 Ar atoms. In fig. 6.27 this signal (c) is compared with similar measurements in the gas phase (a) [AEJ82] and the absorption spectrum of An in an

Ar matrix (b) [FSHD93]. Panel (b) and (c) both show a frequency range of 600 cm$^{-1}$, while panel (a) extends over about 2100 cm$^{-1}$. In the gas phase the signal appears at a similar frequency as in helium droplets (3690 Å = 27100 cm$^{-1}$), but the absorption signal observed in the Ar matrix spectrum is shifted approximately by additional 100 cm$^{-1}$ to the red. Unfortunately, a better S/N-ratio was not achievable for the excitation spectrum in helium droplets, which was recorded for clusters formed in a post pick-up process. The best resolution is offered by the Ar matrix spectrum, where three sharp peaks are observed. It could be shown that they belong to three different sites [FSHD93].

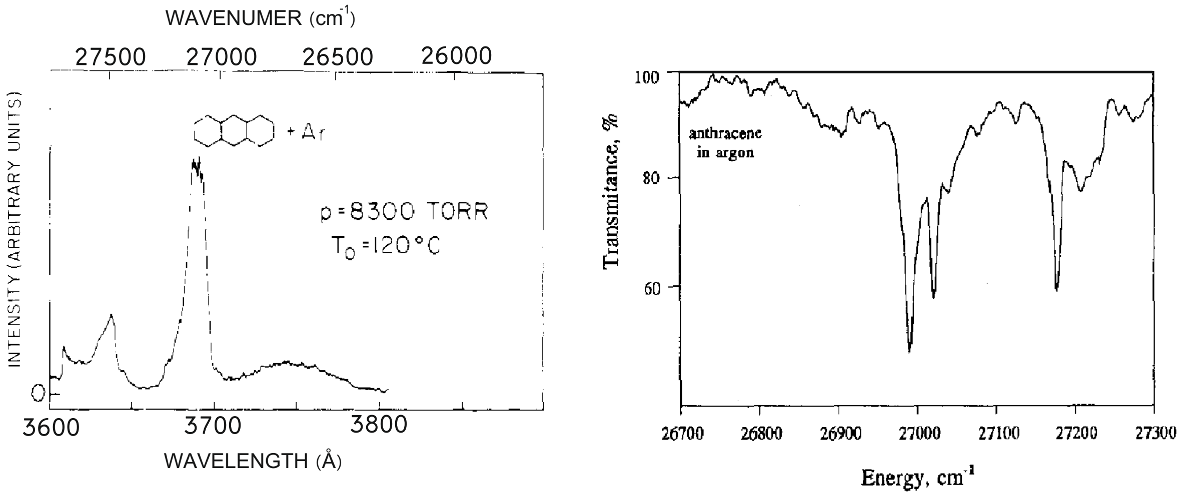

(a) Amirav et al.: J. Phys. Chem. 1982 ([AEJ82])

(b) Fraenkel et al.: Chem. Phys. Lett. 1993 ([FSHD93])

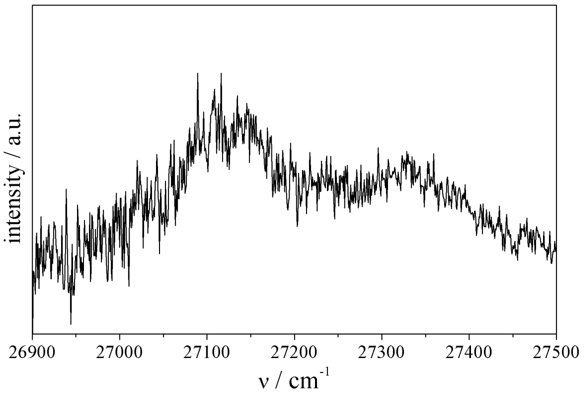

(c) Helium droplet spectrum of An(Ar)$_k$ clusters with ($50 \leq k \leq 90$) formed in a post pick-up process and measured with 1.3 datapoints per 1 cm$^{-1}$.

**Fig. 6.27:** Fluorescence excitation spectrum of large An(Ar)$_k$ clusters in helium droplets (c) compared with similar measurements in the gas phase (a) and the absorption spectrum of An in an Ar matrix (b).

Taking into account the different scale of the panels the signal in the gas phase spectrum exhibits a similar width as the one in helium droplets. An additional week broad signal, which appears to the red of the main signal at 3690 Å in the gas phase is assigned to clusters with An dimers. The An dimer clusters, whose signal shows a spectral separation from the An monomer cluster signal, are not regarded in the matrix and helium droplet spectra. On the basis of this comparison and because it shows the largest red shift to the origin of bare An in helium droplets, the broad signal at 27100 $\mathrm{cm}^{-1}$ in the excitation spectrum in helium droplets is assigned to a cluster where the An molecule is fully embedded in Ar. However, the width of the signal indicates that the cluster size distribution still has an effect on the transitions. Moreover, the discrepancy of about 100 $\mathrm{cm}^{-1}$ between the signal positions in the Ar matrix spectrum and the helium droplet spectrum shows that the two situations differ in more aspects than merely the temperature and the appearance of sites. It might be expected that the cluster signal in the helium droplet spectrum can still be shifted towards lower frequencies by a further increase of the Ar particle density in the gas pick-up cell. However, this could not be observed. Instead, the signal vanished completely for an excessively large Ar doping pressure, which can only be explained with experimental problems.

When comparing these results with the publications on large tetracene-$\mathrm{Ar}_k$ clusters in helium droplets similarities are noticeable [HLTV98, KNT$^+$11]. For clusters with four Ar atoms signals of (4|0), (3|1) and (2|2) isomers are observed. Of clusters with more Ar atoms attached to the tetracene molecule only those with $k = 5$ and $k = 6$ show sharp signals. Beyond that size only broad features are observed in the fluorescence excitation spectrum in helium droplets. The signal of fully in Ar embedded tetracene is also similar to that of fully embedded An. It extends over about 200 $\mathrm{cm}^{-1}$ for clusters formed in a post pick-up process and shows a red shift of about 650 $\mathrm{cm}^{-1}$ relative to the electronic origin of bare tetracene [KNT$^+$11]. For tetracene, however, clusters containing of up to 285 Ar atoms could be measured and analysed, which would explain the larger red shift compared with the $\mathrm{An(Ar)}_k$ clusters discussed above.

### 6.7.2 Dispersed Emission

Large An(Ar)$_k$ clusters formed under pick-up conditions, which result in an average $k$ number $> 5$ show only broad signals in the excitation spectrum in helium droplets. As discussed in the preceding section the cluster size distribution and the existence of a multitude of isomers are assumed to be the main factors for the increased signal width. Despite of the congestion of these cluster signals it is possible to record the dispersed emission of individual An(Ar)$_k$ clusters even in the case of $k > 5$.

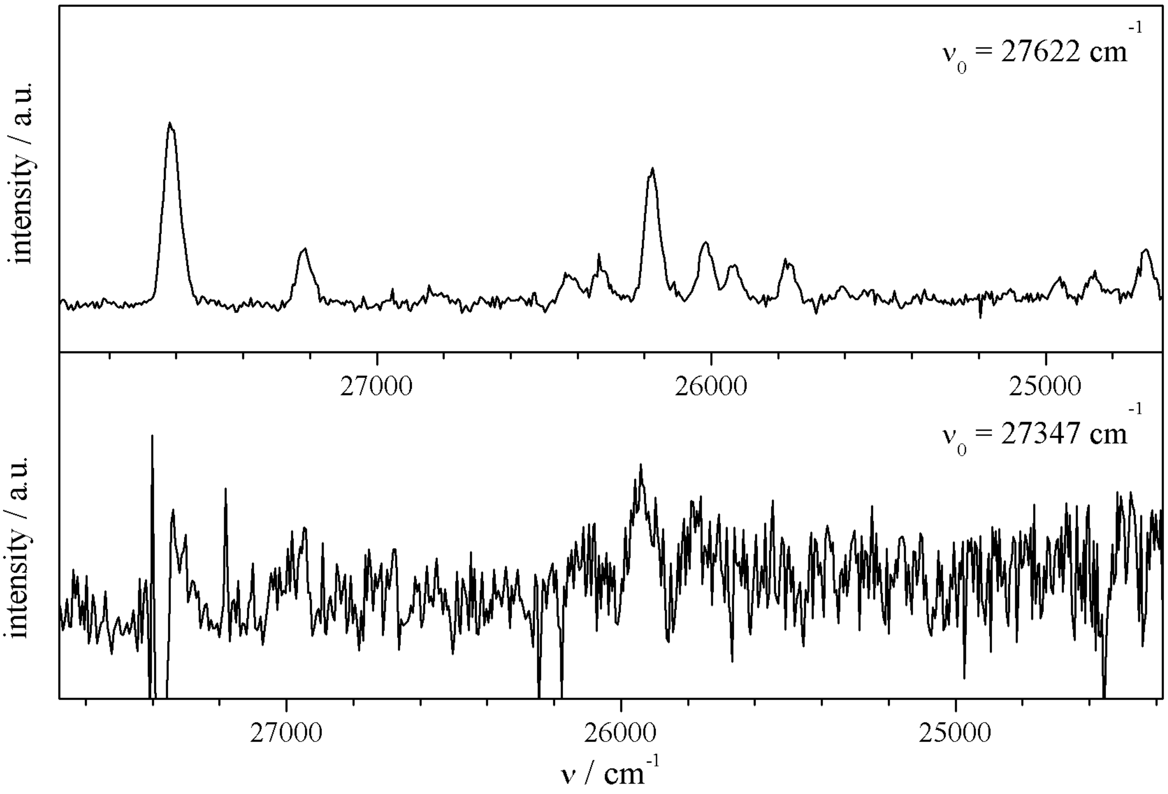

**Fig. 6.28:** Comparison of the emission spectra of bare An (upper panel) and of a large An(Ar)$_k$ cluster (lower panel) in helium droplets. $\nu_0$ denotes the origin of the respective emission. Both panels extend over a frequency range of 3300 cm$^{-1}$. Emission was dispersed with the 1200 lines/mm grating of the spectrograph. The distance between two pixel columns amounts to about 6.5 cm$^{-1}$ at the blue and 5.4 cm$^{-1}$ at the red end of the spectra.

This can be seen in the lower panel of fig. 6.28, which shows the emission spectrum measured upon excitation at 27347 cm$^{-1}$. It corresponds to an excitation with a shift of -262 cm$^{-1}$ to the electronic origin of bare An in helium droplets. At this frequency the maximum of a broad fluorescence excitation signal is observed for an Ar adjustment corresponding to an average $k$ number of about 9. The spectrum is compared with the emission spectrum of bare An in helium droplets shown in the upper panel of fig. 6.28. The panels extend over a frequency range of 3300 $\mathrm{cm}^{-1}$ and the spectra are shifted so as to enable a comparison of the peak positions. Within experimental accuracy the origin of the cluster's emission coincides with the excitation frequency, which provokes the background correction problem explained in chap. 6.4.2. Despite of this problem and the poor S/N-ratio the characteristic vibronic pattern observed for the emission of bare An in helium droplets can be recognized, when comparing the spectra as in fig. 6.28

## 6.8 Summary

In this chapter the electronic spectra of $\mathrm{An(Ar)}_k$ clusters in helium droplets were presented and discussed. The fluorescence excitation of the clusters was investigated for post and prior pick-up cluster formations. The small clusters ($k \leq 4$) show sharp spectral lines, which could be assigned to different cluster stoichiometries via Poisson distribution fits. In addition, by analyzing the signals' response to the pick-up order it was possible to distinguish between transitions of one-sided and two-sided clusters. Dispersed emission spectroscopy was used to identify the electronic origins of the individual clusters. This analysis was limited, however, by the resolution and the S/N-ratio of the emission spectra.

As in the excitation spectra of $\mathrm{An(Ar)}_k$ in the gas phase the signals' red shift relative to the electronic origin of bare An increases with a growing cluster size. For all small $\mathrm{An(Ar)}_k$ clusters in helium droplets with $1 < k < 5$ signals of one-sided and two-sided structures could be identified, which shows that the droplet environment enables the formation and stabilization of cluster configurations, which are not observed in the gas phase. Moreover, in the helium droplet spectrum the signals of the one-sided isomers do not always exhibit smaller red shifts than the ones of the two-sided isomers with the same stoichiometry. As this is in contrast to calculations for the free clusters, it may reflect the influence of the helium environment on the cluster signals spectral shift.

Also the cluster signals' fine structure was analyzed as it yields information on the role of the helium solvation layer on the cluster formation process. The characteristic quartet fine structure, which appears for all signals of bare An in helium droplets, was only observed for one An(Ar) cluster. The corresponding cluster signal does not appear in the gas phase spectrum and is interpreted as belonging to a structure with the Ar atom located on the An-helium solvation complex. All other An(Ar)$_k$ clusters exhibit excitation signals with different fine structures. For these clusters the Ar atoms are expected to be directly located on the An surface with a helium solvation layer around the whole cluster structure.

When regarding large An(Ar)$_k$ clusters with an average cluster size of $k \geq 5$ congested signals of isomeric clusters and clusters with different $k$ numbers are observed instead of individual sharp peaks. Due to the increased width of the cluster size distribution for large $k$ it is not possible to overcome this problem by readjusting the Ar doping pressure. However, despite of the congestion of the large cluster signals the dispersed emission of individual An(Ar)$_k$ clusters even in the case of $k > 5$ is possible, as was shown for an Ar adjustment resulting in an average $k$ number of 9. The excitation signals of these large An(Ar)$_k$ clusters show red shifts of up to $\nu - \nu_0 \approx$ -520 cm$^{-1}$. However, it was not possible with the current setup to reach the bulk value found in an Ar matrix, which shows an additional shift of about 100 cm$^{-1}$ [FSHD93].

# 7 Conclusion

Within this work two different cluster systems formed in superfluid helium droplets were discussed, $\mathrm{Pc(H_2O)}_k$ clusters and $\mathrm{An(Ar)}_k$ clusters. Electronic spectroscopy on these species revealed new details about cluster formation in helium droplets and on methods for their investigation. This conclusion aims to sum up and interpret the gained results and it outlines some suggestions for further research.

For both species a manifold of sharp signals with line widths comparable with those of the bare chromophores' signals could be observed in the fluorescence excitation spectra of small clusters ($k \leq 4$) in helium droplets. They could be assigned to clusters with distinct stoichiometries via Poisson distribution fits. However, as discussed in a recent publication a differentiation between ZPLs and PWs is not accessible at the moment [PWP$^+$14]. Nevertheless only selected transitions were regarded in the detailed investigation of the clusters, always taking into account that the transitions, which are tentatively assigned to PWs may possibly belong to ZPLs of additional clusters instead.

Information on the stability of the clusters was provided by the Stark spectra recorded for $\mathrm{Pc(H_2O)}_k$ in helium droplets. Apparently, the van der Waals interaction between the Pc and the water molecules suffices to form clusters with a certain rigidity, whose free rotation becomes hindered in an external electric field. However, a field strength of 17 kV/cm did not suffice to accomplish an alignment of the cluster ensemble in the homogeneous electric field and transfer the clusters into pendular states. Instead a line broadening was observed for all Stark spectra of the clusters, which is interpreted as a result of the splitting and shifting of the clusters' rotational states. As the clusters did not reach pendular states the spectra could not be applied to draw conclusions on the configurations of the individual cluster isomers as originally planned at the beginning of the study.

More information on $Pc(H_2O)_k$ clusters using Stark spectroscopy can possibly be gained by working with a stronger electric field. If the field strength would suffice to transfer the clusters into pendular states, then an analysis of the spectra as discussed in chap. 3.3 would be possible. However, the question remains whether the clusters are stable enough to ensure that the heavy Pc chromophore follows the orientation of the water molecules in the electric field. This should first be investigated for $Pc(H_2O)$ before turning to larger clusters, which presumably exhibit more isomeric structures to be distinguished from one another.

Also in the case of $An(Ar)_k$ the assignment of different isomeric structures was one of the most challenging problems. For this purpose the excitation spectrum of small $An(Ar)_k$ clusters in helium droplets was measured for a post and a prior pick-up procedure. The comparison of the spectra enabled the distinction between one-sided and two-sided cluster structures. For all small $An(Ar)_k$ clusters ($k < 5$) in helium droplets signals of one-sided and two-sided structures could be identified in the excitation spectrum. This shows that the droplet environment enables the formation and stabilization of cluster configurations, which are not observed in the gas phase. Similar observations have been reported e.g. for tetracene-Ar clusters [HLTV98]. A further characteristic of high resolution helium droplet spectra is the fine structure of the excitation signals, which reveals interactions between the dopant species and its helium environment. For most $An(Ar)_k$ clusters a modification of the fine structure was observed compared with the multiplet, which is characteristic for the transitions of bare An in helium droplets. This shows that the An-helium interaction is altered by the Ar atoms, which coagulate with the An molecule. It can be interpreted by assuming that the clusters form within the droplet environment by replacing helium atoms at the An surface by Ar atoms. Thus, a new helium solvation complex forms around the $An(Ar)_k$ cluster, which manifests itself in the cluster signals' fine structure. However, one $An(Ar)$ cluster shows excitation signals, which have an almost identical fine structure as the one observed for the bare chromophore. The signals exhibit no counterparts in the gas phase spectra and are interpreted as belonging to a cluster with the Ar atom located on the An-helium solvation complex instead of being directly attached to the An surface. These considerations show that isomeric structures have to be considered not only for the An(Ar)$_k$ clusters, but also for the surrounding helium complexes. All of these complexes exhibit distinct transitions, which may additionally be accompanied by phonon excitations of the helium droplet matrix.

The most prominent influence on the spectral signature of the chromophores upon the addition of a small number of Ar atoms or $H_2O$ molecules is a red shift of the transitions. This red shift of the cluster signals relative to the transitions of the bare chromophores increases with the size of the clusters. In the case of small An(Ar)$_k$ clusters this increase is basically monotonic, which is a characteristic of this species. For Pc($H_2O$)$_k$ as well as for e.g. Pc(Ar)$_k$ [LSS07] and tetracene-Ar$_k$ [HLTV98] the frequency regions of the signals belonging to equal-sized clusters overlap. The red shift of the cluster signals is additionally influenced by the helium droplet environment, as could be shown by comparing the helium droplet spectra of An(Ar)$_k$ with calculations of the spectral shifts for free clusters [SBHEJ91]. Not only the An(Ar)$_k$ cluster configurations may differ from those in the gas phase, but also the helium solvation complexes can influence the transition frequencies. Therefore, a direct comparison of the cluster signals' red shifts in gas phase and helium droplet spectra is not practical. In this respect it is noteworthy that the red shifts observed for the vibronic transitions of An(Ar)$_k$ clusters in helium droplets are similar to the red shifts observed for the electronic origins. Also in the case of emission spectroscopy an equal vibrational pattern was observed for bare An and its Ar clusters. This shows that for the regarded vibrations and within the experimental accuracy the addition of a small number of Ar atoms has no material impact on the vibrational frequencies of the chromophore's ground state and excited state.

Further experiments on small An(Ar)$_k$ clusters would be reasonable to gain a better understanding of the structure and microsolvation of these clusters in helium droplets.

The emission spectra upon selective excitation should be repeated using a cw laser and a continuous helium droplet beam. This would cause a significant improvement of the spectra's S/N-ratio and therefore of the informative value for the identification of the electronic origins of different clusters. In addition, pump-probe experiments could be applied to achieve additional information for the assignment of the cluster signals.

Also in the case of large $\mathrm{An(Ar)}_k$ clusters in helium droplets additional experimental investigations should be conducted. The signal with the largest red shift to the electronic origin of bare An in helium droplets was recorded around 27100 $\mathrm{cm}^{-1}$. Although this signal presumably belongs to a species, where An is totally embedded in the Ar cluster, the broad structure of the signal and the comparison with solid Ar matrix spectra indicate that the cluster size distribution still has an influence on the transitions. To enable the formation of even larger clusters a modification of the experimental setup may be necessary, as such clusters could not be observed with the setup presented in this work. Instead of a gas pick-up cell inside the detection chamber, an additional vacuum chamber, which is used only for the particle pick-up procedures, could be applied. It would prevent excessive leakage of dopant particles from the gas pick-up cell into the detection chamber, as the two chambers could be separated by a wall with a skimmer. Thus, higher particle densities of the dopant species could be applied for the formation of larger clusters inside the helium droplets.

To conclude, the electronic spectroscopy reported in this thesis tries to contribute to the understanding of cluster formation in superfluid helium droplets. Further experiments, which are needed to obtain more information on these complex systems, would necessitate the modification of the experimental setup and the application of pump-probe spectroscopy.

# References

[ABPW91] A. Terry Amos, Brian L. Burrows, T. Frank Palmer, and Alan Walters. Dispersion Energy of a van der Waals Complex of an Aromatic Molecule and a Rare-gas Atom. *J. Chem. Soc. Faraday Trans.*, 87(15):2391 – 2398, 1991.

[AEJ82] Aviv Amirav, Uzi Even, and Jortner Jortner. Electronic-Vibrational Excitations of Aromatic Molecules in Large Argon Clusters. *J. Phys. Chem.*, 86(17):3345 – 3358, 1982.

[AEJD83] Aviv Amirav, Uzi Even, Joshua Jortner, and B. Dick. Excited state energetivs of aniline-rare-gas van der Waals complexes. *Mol. Phys.*, 49:899 – 912, 1983.

[AHJ88] Aviv Amirav, Chanan Horwitz, and Joshua Jortner. Optical selection studies of electronic relaxation from the $S_1$ state of jet-cooled anthracene derivatives. *J. Chem. Phys.*, 88:3092 – 3110, 1988.

[Ami87] Aviv Amirav. Rotational effects on energy resolved emission of anthracene. *J. Chem. Phys.*, 86:4706 – 4707, 1987.

[Ami88] Aviv Amirav. Rotational and vibrational energy effect on energy-resolved emission of anthracene and 9-cyanoanthracene. *Chem. Phys.*, 124(2):163 – 175, 1988.

[ASJ84] Aviv Amirav, Mark Sonnenschein, and Joshua Jortner. Spectroscopy and Dynamics of 9,10-Dichloroanthracene·$Ar_n$ van der Waals complexes. *Chem. Phys.*, 88:199 – 207, 1984.

[Atk01] Peter W. Atkins. *Physikalische Chemie.* Wiley-VCH, 2001.

[BE79] V. E. Bondybey and J. H. English. Spectra of the H2 Phthalocyanine in Low-Temperature Matrices. *J. Am. Chem. Soc.*, 101(13):3446 – 3450, 1979.

[BHEJL92] N. Ben-Horin, U. Even, J. Jortner, and S. Leutwyler. Spectroscopy and Nuclear Dynamics of Tetracene-Rare-Gas Heteroclusters. *J. Chem. Phys.*, 97:5296, 1992.

[BKN$^+$90] H. Buchenau, E. L. Knuth, J. Northby, J. P. Toennies, and C. Winkler. Mass spectra and time-of-flight distributions of helium cluster beams. *J. Chem. Phys.*, 92:6875 – 6889, 1990.

[BMLS07] Özgür Birer, Paolo Moreschini, Kevin K. Lehmann, and Giacinto Scoles. Electronic Spectroscopy of Nonalternant Hydrocarbons Inside Helium Nanodroplets. *J. Phys. Chem. A*, 111:12200 – 12209, 2007.

[BS90] D. M. Brink and S. Stringari. Density of states and evaporation rate of helium clusters. *Z. Phys. D.*, 15:257 – 263, 1990.

[BT07] A. Braun and J. Tcherniac. Über die Produkte der Einwirkung von Acetanhydrid auf Phthalamid. *Ber. Dtsch. Chem. Ges.*, 40(2):2709 – 2714, 1907.

[BZB$^+$07] C. A. Barker, X. Zeng, S. Bettington, A. S. Batsanov, M. R. Bryce, and A. Beeby. Porphyrin, Phthalocyanine and Porphyrazine Derivatives with Multifluorenyl Substituents as Efficient Deep-Red Emitters. *Chem. Eur. J.*, 13:6710 – 6717, 2007.

[CDF$^+$06] M. Y. Choi, G. E. Douberly, T. M. Falconer, W. K. Lewis, C. M. Lindsay, J. M. Merritt, P. L. Stiles, and R. E. Miller. Infrared spectroscopy of helium nanodroplets: novel methods for physics and chemistry. *Int. Rev. Phys. Chem.*, 25:15 – 75, 2006.

[CDM05] M. Y. Choi, F. Dong, and R. E. Miller. Multiple tautomers of cytosine identified and characterized by infrared laser spectroscopy in helium nanodroplets: probing structure using vibrational transition moment angles. *Phil. Trans. R. Soc. A*, 363:393 – 413, 2005.

[CG82] Thomas P. Carter and G. D. Gillispie. Site-Selected Fluorescence Study of Anthracene and Its Halogenated Derivatives in Shpol'skii Matrices. *J. Phys. Chem.*, 86:2691 – 2695, 1982.

[CH00] Gerd Collin and Hartmut Höke. *Ullmann's Encyclopedia of Industrial Chemistry*, chapter Anthracene. Wiley-VCH Verlag GmbH & Co. KGaA, 2000.

[Chr13] Lars Christiansen. Spectroscopy of Phthalocyanines in Superfluid Helium Droplets. Master's thesis, Aarhus Universitet, Institut for Fysik og Astronomi, 2013.

[ChYK00] Sung Haeng Cho, Myung han Yoon, and Seong Keun Kim. Spectroscopy and energy disposal dynamics of phthalocyanine-Ar$_n$ (n=1,2) complexes generated by hyperthermal pulsed nozzle source. *Chem. Phys. Lett.*, 326(1-2):65 – 72, 2000.

[CK94] Martin C. R. Cockett and Katsumi Kimura. A study of anthracene-Ar$_n$ (n=0-5) in the ground cationic state by laser threshold photoelectron spectroscopy: Selective ionization of complex isomers formed in the free jet expansion. *J. Chem. Phys.*, 100(5):3429 – 3441, 1994.

[CL93] Tapas Chakraborty and E. C. Lim. Study of van der Waals Clusters of Anthracene by Laser Induced Fluorescence in a Supersonic Jet: Evidence for Two Structurally Different Dimers. *J. Phys. Chem.*, 97:11151 – 11153, 1993.

[CLSS01] Carlo Callegari, Kevin K. Lehmann, Roman Schmied, and Giacinto Scoles. Helium nanodroplet isolation rovibrational spectroscopy: Methods and recent results. *J. Chem. Phys.*, 115:10090 – 10110, 2001.

[Con26] Edward Condon. A Theory of Intensity Distribution in Band Systems. *Phys. Rev.*, 28:1182 –1201, 1926.

[CPG$^+$09] G. Chaidogiannos, F. Petraki, N. Glezos, S. Kennou, and S. Nespurek. Low voltage operating OFETs based on solution-processed metal phthalocyanines. *Appl. Phys. A Mater. Sci. Process.*, 96:763 – 767, 2009.

[DH81] Bernhard Dick and Georg Hohlneicher. Two-Photon Spectroscopy of Dipole-Forbidden Transitions. The low-lying Singlet States of Anthracene. *Chem. Phys. Lett.*, 83:615 – 621, 1981.

[DMBS14] Matthieu Dvorak, Markus Müller, Oliver Bünermann, and Frank Stienkemeier. Size dependent transition to solid hydrogen and argon clusters probed via spectroscopy of PTCDA embedded in helium nanodroplets. *J. Chem. Phys.*, 140:144301 – 1 – 8, 2014.

[DMK$^+$12a] Matthieu Dvorak, Markus Müller, Tobias Knoblauch, Oliver Bünermann, Alexandre Rydlo, Stefan Minniberger, Wolfgang Harbich, and Frank Stienkemeier. Spectroscopy of 3, 4, 9, 10-perylenetetracarboxylic dianhydride (PTCDA) attached to rare gas samples: Clusters vs. bulk matrices. I. Absorption spectroscopy. *J. Chem. Phys.*, 137:164301 – 1 – 9, 2012.

[DMK$^+$12b] Matthieu Dvorak, Markus Müller, Tobias Knoblauch, Oliver Bünermann, Alexandre Rydlo, Stefan Minniberger, Wolfgang Harbich, and Frank Stienkemeier. Spectroscopy of 3, 4, 9, 10-perylenetetracarboxylic dianhydride (PTCDA) attached to rare gas samples: Clusters vs. bulk matrices. II. Fluorescence emission spectroscopy. *J. Chem. Phys.*, 137:164302 – 1 – 6, 2012.

[DS01] Bernhard Dick and Alkwin Slenczka. Inhomogeneous line shape theory of electronic transitions for molecules embedded in superfluid helium droplets. *J. Chem. Phys.*, 115:10206 – 10213, 2001.

[FAMvH12] Frank Filsinger, Doo-Sik Ahn, Gerard Meijer, and Gert von Helden. Photoexcitation of mass/charge selected hemin$^+$, caught in helium nanodroplets. *Phys. Chem. Chem. Phys.*, 14:13370 – 13377, 2012.

[FHL80] P. S. H. Fitch, Ch. A. Haynam, and D. H. Levy. The fluorescence excitation spectrum of free base phthalocyanine cooled in a supersonic free jet. *J. Chem. Phys.*, 73:1064 – 1072, 1980.

[FHL81] P. S. H. Fitch, C. A. Haynam, and D. H. Levy. Intramolecular vibrational relaxation in jet-cooled phthalocyanine. *J. Chem. Phys.*, 74:6612 – 6620, 1981.

[Fra26] J. Franck. Elementary processes of photochemical reactions. *Trans. Faraday Soc.*, 21:536 – 542, 1926.

[FSHD93] R. Fraenkel, U. Samuni, Y. Haas, and B. Dick. A matrix isolation study of the fluorescence of anthracene and anthracene-ammonia adducts in solid argon. *Chem. Phys. Lett.*, 203:523, 1993.

[FWL78] P. S. H. Fitch, L. Wharton, and D. H. Levy. The fluorescence excitation spectrum of free base phthalocyanine cooled in a supersonic expansion. *J. Chem. Phys.*, 69(7):3424, 1978.

[GEA02] V. Ghazarian, J. Eloranta, and V. A. Apkarian. Universal molecule injector in liquid helium: Pulsed cryogenic doped helium droplet source. *Rev. Sci. Instrum.*, 73:3606 – 3613, 2002.

[GHH$^+$82] K. Godzik, T. R. Hays, W. E. Henke, H. L. Selzle, E. W. Schlag, and S. H. Lin. Effect of Formation of van der Waals Complexes on Molecular Physical Properties. *Laser Chem.*, 1(1):59 – 75, 1982.

[GHH$^+$00] S. Grebenev, M. Hartmann, M. Havenith, B. Sartakov, J. P. Toennies, and A. F. Vilesov. The rotational spectrum of single OCS molecules in liquid $^4$He droplets. *J. Chem. Phys.*, 112(10):4485 – 4495, März 2000.

[GNB94] Daniel Gruner, An Nguyen, and Paul Brumer. Theoretical study of the $S_1 \leftrightarrow S_0$ spectroscopy of anthracene. *J. Chem. Phys.*, 101:10366 – 10381, 1994.

[GSS92] S. Goyal, D. L. Schutt, and G. Scoles. Vibratrional Spectroscopy of Sulfur Hexafluoride Attached to Helium Clusters. *Phys. Rev. Lett.*, 69:933 – 936, 1992.

[GT03] Robert E. Grisenti and J. Peter Toennies. Cryogenic Microjet Source for Orthotropic Beams of Ultralarge Superfluid Helium Droplets. *Phys. Rev. Lett.*, 90(23):234501 – 1 – 4, 2003.

[GTV98] Slava Grebenev, J. Peter Toennies, and Andrei F. Vilesov. Superfluidity Within a Small Helium-4 Cluster: The Microscopic Andronikashvili Experiment. *Science*, 279:2083 – 2086, 1998.

[HBSZ91] Ahmed Heikal, Luis Bañares, David H. Semmes, and Ahmed H. Zewail. Real-time dynamics of vibrational predissociation in anthracene-Ar$_n$ (n = 1,2,3). *Chem. Phys.*, 157:231 – 250, 1991.

[HEJ01] Andreas Heidenreich, Uzi Even, and Joshua Jortner. Nonrigidity, delocalization, spatial confinement and electronic-vibrational spectroscopy of anthracene-helium clusters. *J. Chem. Phys.*, 115:10175 – 10185, 2001.

[HHSS81] T. R. Hays, W. Henke, H. L. Selzle, and E. W. Schlag. Anthracene-Argon Complexes in a Supersonic Jet; Spectra and Lifetimes. *Chem. Phys. Lett.*, 77:19 – 24, 1981.

[HJ03] Andreas Heidenreich and Joshua Jortner. Permutational symmetry, isotope effects, side crossing, and singlet-triplet splitting in anthracene·He$_N$ (N = 1, 2) clusters. *J. Chem. Phys.*, 118:10101 – 10119, 2003.

[HLTV98] Matthias Hartmann, Albrecht Lindinger, J. Peter Toennies, and Andrei F.

Vilesov. Laser-induced fluorescence spectroscopy of van der Waals complexes of tetracene-Ar$_N$ (N $\leq$ 5) and pentacene-Ar within ultracold liquid He droplets. *Chem. Phys.*, 239:139 – 149, 1998.

[HLTV01] Matthias Hartmann, Albrecht Lindinger, J. Peter Toennies, and Andrej F. Vilesov. Hole-Burning Studies of the Splitting in the Ground and Excited Vibronic States of Tetracene in Helium Droplets. *J. Phys. Chem. A*, 105:6369, 2001.

[HLTV02] Matthias Hartmann, Albrecht Lindinger, J. Peter Toennies, and Andrej F. Vilesov. The phonon wings in the (S$_1$ $\leftarrow$ S$_0$) spectra of tetracene, pentacene, porphin and phthalocyanine in liquid helium droplets. *Phys. Chem. Chem. Phys.*, 4:4839 – 4844, 2002.

[HMTV95] M. Hartmann, R. E. Miller, J. P. Toennies, and A. Vilesov. Rotationally Resolved Spectroscopy of SF$_6$ in Liquid Helium Clusters: A Molecular Probe of Cluster Temperature. *Phys. Rev. Lett.*, 75(8):1566 – 1569, Aug 1995.

[HMTV96] M. Hartmann, F. Mielke, J. P. Toennies, and A. F. Vilesov. Direct Spectroscopic Observation of Elementary Excitations in Superfluid He Droplets. *Phys. Rev. Lett.*, 76:4560 – 4563, 1996.

[HNH$^+$84] Okikazu Hirabaru, Tomohiro Nakase, Kenji Hanabusa, Hirofusa Shirai, Kiichi Takemoto, and Nobumasa Hojo. Functional metal-porphyrazine derivatives and their polymers. Part 11. Secondary fuel cells based on oxygen reduction at a platinum electrode modified by metal-2,9,16,23-tetracarboxyphthalocyanine covalently bound to poly(2-vinylpyridine-styrene). *J. Chem. Soc., Dalton. Trans.*, pages 1485 – 1489, 1984.

[HRV82] T. H. Huang, K. E. Rieckhoff, and E. M. Voigt. Shpol'skii effect and vibronic spectra of the phthalocyanines. *J. Chem. Phys.*, 77(7):3424 – 3441, 1982.

[HTD98] Jan Harms, J. Peter Toennies, and Franco Dalfovo. Density of superfluid helium droplets. *Phys. Rev. B*, 58(6):3341 – 3350, Aug 1998.

[HTK97] J. Harms, J. P. Toennies, and E. L. Knuth. Droplets formed in helium free-jet expansion from states near the critical point. *J. Chem. Phys.*, 106:3348 – 3357, 1997.

[HYS$^+$85] W. E. Henke, Weijun Yu, H. L. Selzle, E. W. Schlag, D. Wutz, and S. H. Lin. Shifts in Fluorescence Excitation Spectra of Anthracene-Argon van der Waals Complexes. *Chem. Phys.*, 92:187 – 197, 1985.

[Jan68] P. J. C. Janssen. Indication de quelques-uns des résultats obtenus à Cocanada, pendant l'éclipse du mois d'août dernier, et à la suite de cette éclipse. *CRAS*, 67:838 – 839, 1868.

[JK97] Gouri S. Jas and Krysztof Kuczera. Ab initio calculations of $S_1$ excited state vibrational spectra of benzene, naphthalene and anthracene. *Chem. Phys.*, 214:229 – 241, 1997.

[JN92] T. Jiang and J. A. Northby. Fragmentation clusters formed in supercritical expansions of $He4$. *Phys. Rev. Lett.*, 68(17):2620 – 2623, Apr 1992.

[JWKJ96] Gouri S. Jas, Chaozhi Wan, Krysztof Kuczera, and Carey K. Johnson. Picosecond Time-Resolved Fourier-Transform Raman Spectroscopy and Normal-Mode Analysis of the Ground State and Singlet Excited State of Anthracene. *J. Phys. Chem.*, 100:11857 – 11862, 1996.

[Kap38] P. Kapitza. Viscosity of liquid helium below the $\lambda$-point. *Nature*, 141:74, 1938.

[KGMNS$^+$07] Susumu Kuma, Haruka Goto, Mikhail N. Mikhail N. Slipchenko, Andrey F. Vilesov, Alexander Khramov, and Takamasa Momose. Laser induced fluorescence of Mg-phthalocyanine in He droplets: Evidence for fluxionality of large $H_2$ clusters at 0.38 K. *J. Chem. Phys.*, 127:214301, 2007.

[KH99] E. L. Knuth and U. Henne. Average size and size distribution of large droplets produced in a free-jet expansion of a liquid. *J. Chem. Phys.*, 110:2664 – 2668, 1999.

[KM95] Martin Klessinger and Josef Michl. *Excited States and Photochemistry of Organic Molecules.* VCH, 1995.

[KNT$^+$11] Susumu Kuma, Hiroko Nakahara, Masaaki Tsubouchi, Akira Takahashi, Majd Mustafa, Goeun Sim, Takamasa Momose, and Andrey F. Vilesov. Laser Induced Fluorescence Spectroscopy of Tetracene with Large Ar, Ne, and $H_2$ Clusters in Superfluid He Nanodroplets. *J. Phys. Chem. A*, 115:7392 – 7399, 2011.

[Knu97] E. L. Knuth. Size correlations for condensation clusters produced in free-jet expansions. *J. Chem. Phys.*, 107:9125 – 9132, 1997.

[KRH05] Serge Krasnokutski, Gael Rouillé, and Friedrich Huisken. Electronic spectroscopy of anthracene molecules trapped in helium nanodroplets. *Chem. Phys. Lett.*, 406:386 – 392, 2005.

[Kro72] Heinz Kropf. Katalyse durch Phthalocyanin-Komplexe. *Angew. Chem.*, 84:219 – 220, 1972.

[KSK04] K. Kameyama, A. Satake, and Y. Kobuke. Light-harvesting composites of directly connected porphyrin-phthalocyanine dyads and their coordination dimers. *Tetrahedron Lett.*, 45(41):7617 – 7620, 2004.

[KTL00] K. S. Kim, P. Tarakeshwar, and J. Y. Lee. Molecular Clusters of $\pi$-Systems: Theoretical Studies of Structures, Spectra, and Origin of Interaction Energies. *Chem. Rev.*, 100:4145 – 4185, 2000.

[KZ85] Brian W. Keelan and Ahmed H. Zewail. Rotational band contour analysis of symmetries and interactions of vibrational levels in anthracene $S_1$. *J. Chem. Phys.*, 82:3011 – 3019, 1985.

[LÖ0] G. Löbbert. *Ullmann's Encyclopedia of Industrial Chemistry*, volume 27, chapter Phthalocyanines, pages 181 – 213. Wiley-VCH Verlag GmbH & Co. KGaA, 2000.

[Lan41] L. Landau. Theory of Superfluidity of Helium II. *Phys. Rev.*, 60:356 – 358, 1941.

[LB90] S. Leutwyler and J. Bösinger. Rare-Gas Solvent Clusters: Spectra, Structures, and Order-Disorder Transitions. *Chem. Rev.*, 90:489 – 507, 1990.

[LBD08] Evgeniy Loginov, Andreas Braun, and Marcel Drabbels. A new sensitive detection scheme for helium nanodroplet isolation spectroscopy: application to benzene. *Phys. Chem. Chem. Phys.*, 10:6107 – 6114, 2008.

[LBH+98] Stephen R. Langhoff, Charles W. Bauschlicher, Douglas M. Hudgins, Scott A. Sandford, and Louis J. Allamandola. Infrared Spectra of Substituted Polycyclic Aromatic Hydrocarbons. *J. Phys. Chem. A*, 102:1632 – 1646, 1998.

[Leh04] Rudolf Lehnig. *Anregungs- und Emissionsspektroskopie von organischen Molekülen in $^4$He-Tröpfchen*. PhD thesis, Universität Regensburg, 2004.

[LFSZ84] W. R. Lambert, P. M. Felker, J. A. Syage, and A. H. Zewail. Jet spectroscopy of anthracene and deuterated anthracenes. *J. Chem. Phys.*, 81:2195 – 2208, 1984.

[Lin99] Albrecht Lindinger. *Vibronische Spektroskopie von organischen und biologischen Molekülen in $^4$He-Clustern*. PhD thesis, Georg-August-Universität Göttingen, 1999.

[LJ87] Samuel Leutwyler and Joshua Jortner. Adsorption of Rare-Gas Atoms on Microsurfaces of Large Aromatlc Molecules. *J. Phys. Chem.*, 91:5558 – 5568, 1987.

[LLTV01] Albrecht Lindinger, Eugene Lugovoj, J. Peter Toennies, and Andrei F. Vilesov. Splitting of the Zero Phonon Lines of Indole, 3 Methyl Indole, Tryptamine and N-Acetyl Tryptophan Amide in Helium Droplets. *Z. Phys. Chem.*, 215:401 – 416, 2001.

[LN90] Michael Lindrum and Bernhard Nickel. Transient spectral hole-burning in the $S_0 \rightarrow S_1$ absorption band of anthracene in a polymethylmethacrylate matrix. *Chem. Phys.*, 144(1):129 – 145, 1990.

[Log08] Evgeniy Loginov. *Photoexcitation and Photoionization Dynamics of Doped Liquid Helium-4 Nanodroplets.* PhD thesis, EPFL Lausanne, 2008.

[LPV$^+$09] R. Lehnig, D. Pentlehner, A. Vdovin, B. Dick, and A. Slenczka. Photochemistry of 3-hydroxyflavone inside superfluid helium nanodroplets. *J. Chem. Phys.*, 131:194307 – 1 – 8, 2009.

[LRD05] Evgeniy Loginov, Dominic Rossi, and Marcel Drabbels. Photoelectron Spectroscopy of Doped Helium Nanodroplets. *Phys. Rev. Lett.*, 95:163401 – 1 – 4, 2005.

[LS03] R. Lehnig and A. Slenczka. Emission spectra of free base phthalocyanine in superfluid helium droplets. *J. Chem. Phys.*, 118:8256 – 8262, 2003.

[LS04a] R. Lehnig and A. Slenczka. Quantum solvation of phthalocyanine in superfluid helium droplets. *J. Chem. Phys.*, 120:5064 – 5066, 2004.

[LS04b] Rudolf Lehnig and Alkwin Slenczka. Microsolvation of Phthalocyanines in Superfluid Helium Droplets. *ChemPhysChem*, 5:1014 – 1019, 2004.

[LS05] R. Lehnig and A. Slenczka. Spectroscopic investigation of the solvation of organic molecules in superfluid helium droplets. *J. Chem. Phys.*, 122:244317 – 1 – 9, 2005.

[LSK$^+$04] Rudolf Lehnig, Mikhail Slipchenko, Susumu Kuma, Takamasa Momose, Boris Sartakov, and Andrey Vilesov. Fine structure of the ($S_1 \leftarrow S_0$) band origins of phthalocyanine molecules in helium droplets. *J. Chem. Phys.*, 121:9396 – 9405, 2004.

[LSS07] Rudolf Lehnig, Joshua A. Sebree, and Alkwin Slenczka. Structure and Dynamics of Phthtalocyanine-Argon$_n$ (n = 1-4) Complexes Studied in Helium Nanodroplets. *J. Phys. Chem. A*, 111:7576 – 7584, 2007.

[LST93] M. Lewerenz, B. Schilling, and J. P. Toennies. A new scattering deflection method for determining and selecting the sizes of large liquid clusters of $^4$He. *Chem. Phys. Lett.*, 206:381 – 387, 1993.

[LST95] M. Lewerenz, B. Schilling, and J. P. Toennies. Successive capture and coagulation of atoms and molecules to small clusters in large liquid helium clusters. *J. Chem. Phys.*, 102:8191 – 8207, 1995.

[LTV04] Albrecht Lindinger, J. Peter Toennies, and Andrej F. Vilesov. The effects of isotope substitution and nuclear spin modifications on the spectra of complexes of tetracene with hydrogen molecules in ultracold 0.37 K He droplets. *J. Chem. Phys.*, 121:12282 – 12292, 2004.

[LTV06] Albrecht Lindinger, J. Peter Toennies, and Andrey F. Vilesov. Laser-induced fluorescence spectra of tetracene complexes with Ne, $H_2O$, $D_2O$ He droplets. *Chem. Phys. Lett.*, 429:1 – 7, 2006.

[MB87] J. A. Menapace and E. R. Bernstein. Spectroscopic studies of phthalocyanines and their clusters with small molecules. *J. Chem. Phys.*, 87(12):6877 – 6889, 1987.

[MDM$^+$11] Ciaran Murray, Nadia Dozova, John G. McCaffrey, Niloufar Shafizadeh, Wuthurath Chin, Michel Broquier, and Claudine Crépin. Visible luminescence spectroscopy of free-base and zinc phthalocyanines isolated in cryogenic matrices. *Phys. Chem. Chem. Phys.*, 13(39):17543 – 17554, 2011.

[MKH$^+$98] Tomohiro Matsuoka, Kentaro Kosugi, Kazuyuki Hino, Masaharu Nishiguchi, Kazuhiko Ohashi, Nobuyuki Nishi, and Hiroshi Sekiya. Electronic Spectra of Jet-Cooled Anthracene-Dimer: Evidence of Two Isomers in the Electronic Ground State. *J. Phys. Chem. A*, 102:7598 – 7602, 1998.

[MT63] F. H. Moser and A. L. Thomas. *Phthalocyanine Compounds.* Reinhold Publ. Co., New York, 1963.

[MT83] F. H. Moser and A. L. Thomas. *The Phthalocyanines, vol. I and II.* CRC Press, Inc. Boca Raton, Florida, 1983.

[NGH97] Hiromichi Niikura, Urs Graf, and Satoshi Hirayama. Intramolecular nonradiative relaxation from the first excited singlet background manifolds of anthracene and 9,10-dichloroanthracene in partially jet-cooled states. *Chem. Phys. Lett.*, 266:217 – 222, 1997.

[noz] *The Even-Lavie Valve, Cryogenic Pulsed Valve for Supersonic Expansion, Type E.L.-5-C-2005, 1kHz, High Repetition Rate, Operating Manual.*

[Ohn79] Koichi Ohno. Normal Coordinate calculations of Benzoid Hydracarbons. *J. of Molecular Spectroscopy*, 77:329 – 348, 1979.

[ORF95] Shane M. Ohline, Joann Romascan, and Peter M. Felker. Rotational Coherence Spectroscopy of Aromatic-$(\mathrm{Ar})_n$ Clusters: Geometries of Anthracene-$(\mathrm{Ar})_n$, 9,10-Dirchloroanthracene-Ar, and Tetracene-Ar. *J. Phys. Chem.*, 99:7311 – 7319, 1995.

[OS98] Vahur Oja and Eric M. Suuberg. Vapor Pressures and Enthalpies of Sublimation of Polycyclic Aromatic Hydrocarbons and Their Derivatives. *J. Chem. Eng. Data*, 43:486 – 492, 1998.

[PDM$^+$02] F. Piuzzi, I. Dimicoli, M. Mons, P. Millié, V. Brenner, Q. Zhao, B. Soep, and A. Tramer. Spectroscopy, dynamics and structures of jet formed anthracene clusters. *Chem. Phys.*, 275:123 – 147, 2002.

[Pen10] Dominik Pentlehner. *Perturbations of Electronic Transitions of Orga-*

*nic Molecules in Helium Droplets Generated with a New Pulsed Droplet Source*. PhD thesis, Universität Regensburg, 2010.

[PGDS10] D. Pentlehner, Ch. Greil, B. Dick, and A. Slenczka. Line broadening in electronic spectra of anthracene derivatives inside superfluid helium nanodroplets. *J. Chem. Phys.*, 133:114505 – 1 – 9, 2010.

[PJ99] F. L. Plows and A. C. Jones. Laser-desorption supersonic jet spectroscopy of phthalocyanines. *J. Mol. Spectrosc.*, 194(2):163 – 170, 1999.

[PKSZ88] Lawrence W. Peng, Brian W. Keelan, David H. Semmes, and Ahmed H. Zewail. Dynamics of Intramolecular Vibrational Energy Redistribution in Deuteriated Anthracenes: Rotational Band Contour Analysis and Time-Resolved Measurements. *J. Phys. Chem.*, 92:5540 – 5549, 1988.

[PRD$^{+}$09] Dominik Pentlehner, Ricarda Riechers, Bernhard Dick, Alkwin Slenczka, Uzi Even, Nachum Lavie, Ravie Brown, and Kfir Luria. Rapidly pulsed helium droplet source. *Rev. Sci. Instrum.*, 80:043302 – 1 – 9, 2009.

[PRV$^{+}$11] D. Pentlehner, R. Riechers, A. Vdovin, G. M. Pötzl, and A. Slenczka. Electronic Spectroscopy of Molecules in Superfluid Helium Nanodroplets: An Excellent Sensor for Intramolecular Charge Redistribution. *J. Phys. Chem. A*, 115:7034 – 7043, 2011.

[PS12] Dominik Pentlehner and Alkwin Slenczka. Microsolvation of anthracene inside superfluid helium nanodroplets. *Mol. Phys.*, 110:1933 – 1940, 2012.

[PS13] D. Pentlehner and A. Slenczka. Electronic spectroscopy of 9,10-dichloroanthracene inside helium droplets. *J. Chem. Phys.*, 138:024313 – 1 – 11, 2013.

[PVH01] Nikolas Pörtner, Andrej F. Vilesov, and Martina Havenith. The formation of heterogeneous van der Waals complexes in helium droplets. *Chem. Phys. Lett.*, 343:281 – 288, 2001.

[PWP$^{+}$14] T. Premke, E.-M. Wirths, D. Pentlehner, R. Riechers, R. Lehnig, A. Vdovin, and A. Slenczka. Microsolvation of molecules in superfluid helium nanodroplets revealed by means of electronic spectroscopy. *Front. Chem.*, 2(51):1 – 12, 2014.

[Ram95] William Ramsay. Helium, a Gaseous Constituent of Certain Minerals. Part I. *Proc. R. Soc. London*, 58:80 – 89, 1895.

[Rie11] Ricarda Eva Friederike Elisabeth Riechers. *High-resolution spectroscopy in superfluid helium droplets. Investigation of vibrational fine structures in electronic spectra of phthalocyanine and porphyrin derivatives.* PhD thesis, Universität Regensburg, 2011.

[RKH$^+$04] Gael Rouillé, Serge Krasnokutski, Friedrich Huisken, Thomas Henning, Oleksandr Subkhorukov, and Angela Staicu. Ultraviolet spectroscopy of pyrene in a supersonic jet and in liquid helium droplets. *J. Chem. Phys.*, 120:6028 – 6034, 2004.

[RS85] A. A. Radzig and B. M. Smirnov. *Reference Data on Atoms, Molecules, and Ions, Springer, Heidelberg, 1985.* Springer, 1985.

[SAJ84] Mark Sonnenschein, Aviv Amirav, and Joshua Jortner. Absolute Fluorescence Quantum Yields of Large Molecules in Supersonic Jet Expansions. *J. Phys. Chem.*, 88:4214 – 4218, 1984.

[SBGI07] P. P. Semyannikov, T. V. Basova, V. M. Grankin, and I. K. Igumenov. Vapour pressure of some phthalocyanines. *J. Porphyrins and Phthalocyanines*, 4:271 – 277, 2007.

[SBHEJ91] Eli Shalev, Narda Ben-Horin, Uzi Even, and Joshua Jortner. Electronic spectral shifts of aromatic molecule-rare-gas heteroclusters. *J. Chem. Phys.*, 95:3147 – 3166, 1991.

[SBJ91] Eli Shalev, Narda BenHorin, and Joshua Jortner. Radiative lifetimes of van der Waals heteroclusters. *J. Chem. Phys.*, 94(12):7757 – 7768, 1991.

[ScD$^+$04] Roman Schmied, Çarcaçabal, Adriaan M. Dokter, Vincent P. A. Lonij, Kevin K. Lehmann, and Giacinto Scoles. UV spectra of benzene isotopomers and dimers in helium nanodroplets. *J. Chem. Phys.*, 121:2701 – 2710, 2004.

[SDHT01] Alkwin Slenczka, Bernhard Dick, Matthias Hartmann, and J. Peter Toennies. Inhomogeneous broadening of the zero phonon line of phthalocyanine in superfluid helium droplets. *J. Chem. Phys.*, 115:10199 – 10205, 2001.

[SKMV02] Mikhail N. Slipchenko, Susumu Kuma, Takamasa Momose, and Andrey F. Vilesov. Intense pulsed helium droplet beams. *Rev. Sci. Instrum.*, 73:3600 – 3605, 2002.

[SL06] Frank Stienkemeier and Kevin K. Lehmann. Spectroscopy and dynamics in helium nanodroplets. *J. Phys. B: At. Mol. Opt. Phys.*, 39:R127 – R166, 2006.

[SRS+04] A. Staicu, G. Rouillé, O. Sukhorukov, Th. Henning, and F. Huisken. Cavity ring-down laser absorption spectroscopy of jet-cooled anthracene. *Mol. Phys.*, 102:1777 – 1783, 2004.

[SS75] Friedrich Steinbach and Herbert H. Schmidt. Metal phthalocyanines used as catalysts in gas phase reactions. IV. Oxidation of 2-propanol catalyzed by monomeric $\beta$-copper-phthalocyanine in the presence of sulfur compounds. *J. Catal.*, 39:190 – 197, 1975.

[SSMS05] Wataru Sotoyama, Hiroyuki Sato, Azuma Matsuura, and Norio Sawatari. Ab initio configuration interaction singles (CIS) study on polycyclic aromatic molecules (II): Predicting fluorescence quantum yields by calculating the excitation energies. *Journal of Molecular Structure: THEOCHEM*, 756:35 – 38, 2005.

[ST87] S. Stringari and J. Treiner. Systematics of liquid helium clusters. *J. Chem. Phys.*, 87(8):5021 – 5027, 1987.

[ST08] A. Slenczka and J. P. Toennies. Chemical Dynamics Inside Superfluid Helium Nanodroplets at 0.37 K. In I. A. M. Smith, editor, *Low Temperatures and Cold Molecules*, page 345. World Scientific, Singapore, 2008.

[Ste85] G. D. Stein. Cluster Beam Sources: Predictions and Limitations of the Nucleation Theory. *Surf. Sci.*, 156:44 – 56, 1985.

[SV01] Frank Stienkemeier and Andrey F. Vilesov. Electronic spectroscopy in He droplets. *J. Chem. Phys.*, 115:10119 – 10137, 2001.

[Tis47] Laszlo Tisza. The Theory of Liquid Helium. *Phys. Rev.*, 72(9):838 – 854, 1947.

[TV98] J. Peter Toennies and Andrei F. Vilesov. Spectroscopy of Atoms and Moelcules in Liquid Helium. *Annu. Rev. Phys. Chem.*, 49:1 – 41, 1998.

[TV04] J. Peter Toennies and Andrey F. Vilesov. Superfluid Helium Droplets: A Uniquely Cold Nanomatrix for Molecules and Molecular Complexes. *Angew. Chem. Int. Ed.*, 43:2622 – 22648, 2004.

[UBD+98] D. Uridat, V. Brenner, I. Dimicoli, J. Le Calvé, P. Millié, M. Mons, and F. Piuzzi. Existence of two internal energy distributions in jet-formed van der Waals heteroclusters: example of the anthracene-argon$_n$ system. *Chem. Phys.*, 239:151 – 175, 1998.

[VVR71] P. S. Vincett, E. M. Voigt, and K. E. Rieckhoff. Phosphorescence and Fluorescence of Phthalocyanines. *J. Chem. Phys.*, 55:4131 – 4140, 1971.

[WDW09] Heather D. Whitley, Jonathan L. DuBois, and K. Brigitta Whaley. Spectral shifts and helium configurations in $^4$He$_N$-tetracene clusters. *J. Chem. Phys.*, 131:124514, 2009.

[Wed97] Gerd Wedler. *Lehrbuch der Physikalischen Chemie*. Wiley-VCH, 1997.

[WH94] Joachim Wolf and Georg Hohlneicher. High-resolution one- and two-photon spectra of matrix-isolated anthracene. *Chem. Phys.*, 181:185 – 208, 1994.

[WHKW05] Heather D. Whitley, Patrick Hunag, Yongkyong Kwon, and K. Brigitta Whaley. Multiple solvation configurations around phthalocyanine in helium droplets. *J. Chem. Phys.*, 123:054307, 2005.

[Wir10] Eva-Maria Wirths. Fluoreszenzanregungsspektroskopie in einem gepulsten Strahl aus superfluiden Heliumtropfen. Master's thesis, Universität Regensburg, 2010.

[YBE05] Shengfu Yang, Scott M. Brereton, and Andrew M. Ellis. Controlled growth of helium nanodroplets from a pulsed source. *Rev. Sci. Instrum.*, 76:104102 – 1 – 4, 2005.

[YBN$^+$07] Shengfu Yang, Scott M. Brereton, Satvinder Nandhra, Andrew M. Ellis, Bo Shang, Lan-Feng Yuan, and Jinlong Yang. Electron impact ionization of water-doped superfluid helium nanodroplets: Observation of $He(H_2O)_n^+$clusters. *J. Chem. Phys.*, 127:134303 – 1 – 6, 2007.

[YBWE06] Shengfu Yang, Scott M. Brereton, Martyn D. Wheeler, and Andrew M. Ellis. Electron Impact Ionization of Haloalkanes in Helium Nanodroplets. *J. Phys. Chem. A*, 110:1791 – 1797, 2006.

[YE08] Shengfu Yang and Andrew M. Ellis. Selecting the size of helium nanodroplets using time-resolving probing of a pulsed helium droplet beam. *Rev. Sci. Instrum.*, 79:016106 – 1 – 2, 2008.

[ZHS95] Shmuel Zilberg, Yehuda Haas, and Sason Shaik. Electronic Spectrum of Anthracene: An ab-Initio Molecular Orbital Calculation Combined with a Valence Bond Interpretation. *J. Phys. Chem.*, 99:16558 – 16565, 1995.

[ZSFH94] S. Zilberg, U. Samuni, R. Fraenkel, and Y. Haas. The vibrational structure of the $S_0 \rightarrow S_1$ transition of anthracene. *Chem. Phys.*, 186:303 – 316, 1994.

[ZSGL04] Marina v. Zhigalko, Oleg V. Shishkin, Leonid Gorb, and Jerzy Leszczynski. Out-of-plane defromability of aromatic systems in naphthalene, anthracene and phenanthrene. *Journal of Molecular Structure*, 693:153 – 159, 2004.

[ZZ88] Francesco Zerbetto and Marek Z. Zgierski. Theoretical Analysis of Franck–Condon and Vibronic Activity of the $a_g$ and $b_{3g}$ Modes in the $S_0 \leftrightarrow S_1$ Transitions in Anthracene. *Chem. Phys.*, 127:17 – 29, 1988.

# Acknowledgement

Thanks to ...

... particularly my supervisor Prof. Dr. Alkwin Slenczka for his encouragement, the great support, the many scientific and personal discussions and for granting the freedom to follow own ideas.

... Prof. Dr. Bernhard Dick for stimulating conversations and for giving me the opportunity to work on this project as a scientific assistant at his chair.

... all current and former members of the of the helium droplet group, Dr. Ricarda Riechers, Lars Christiansen and especially to Dr. Dominik Pentlehner and Tobias Premke, for the great atmosphere and support in the lab, the fruitful discussions and for their friendship.

... all further members of the chair, especially to Dr. Rafal Czerwienicz, Markus Leitl, Dr. Thomas Hofbeck, Alexander Schinabeck, Dr. Larisa Mataranga-Popa, Manuel Schneider, Nicole Berner, Uwe Faltermeier, Dr. Christian Greil, Fabian Brandl, Kathrin Magerl and Ivan Stambolic, for being fantastic colleagues, who are always willing to help whenever needed, to exchange ideas over a cup of tee and to have a great time inside and outside the university.

... Dr. Uwe Kensy and the staff of the mechanic and electronic workshops for their valuable work and their help with technical problems.

... Madlene von Sanden, Andrea Nömeier and Klaus Ziereis for their indispensable assistance in the everyday life of our research group.

... the Bischöfliche Studienförderung Cusanuswerk for the financial and personal support throughout my Bachelor, Master and PhD studies and for the wonderful graduate program and holiday academies.

... my flatmates and my friends, especially to Anne, for their encouragements and the great time spent together.

... in particular my family and Benedikt for their love and never-ending support all these years.